Novel Greening, Processing Route, and Bio-Inspired Hierarchical Structuring of Engineered Cementitious Composites for Sustainable Infrastructure

by

Daniel G. Soltan

A dissertation submitted in partial fulfillment
of the requirements for the degree of
Doctor of Philosophy
(Macromolecular Science and Engineering)
in the University of Michigan
2017

Doctoral Committee:

Professor Victor C. Li, Co-Chair
Professor Richard E. Robertson, Co-Chair
Professor Maria C. Lemos
Professor Holmer Savastano Jr., University of Sao Paulo

Daniel Soltan

dsoltan@umich.edu

ORCID iD: 0000-0002-2599-5660

To my parents,
for their immeasurable love and support that I will carry with me always,
and for which I am endlessly grateful.

Mom and Dad,
You are
my shipwrights,
making all my voyages possible,
my lighthouses,
beacons of aid in rocky waters,
and my stars,
guiding me from afar, always

ACKNOWLEDGMENTS

This dissertation reports the most significant findings from the three primary research projects on which I have worked in my time at the University of Michigan. This was not achieved alone, nor in a vacuum.

All three of these projects were collaborative to some degree, and I have a tremendous amount of gratitude to these collaborators, not only for their research contributions and guidance on these projects, but also for the inspiration and motivation they unknowingly provided to me. My favorite aspect of my dissertation research has been the research discussions I have had with these collaborators and my advisor, Professor Li. Discussions with these exceptional and visionary people always left me with renewed enthusiasm and inspiration for whatever project we happened to be discussing. I treasure the endless and infectious optimism of scientific researchers and innovators, and I will strive to exemplify this quality throughout my own career.

I would like to first thank each of the research collaborators who have had significant impacts on my dissertation research. Thanks to Professor Holmer Savastano Jr. for close collaboration on the curauá composites project, many meaningful research discussions, and for his kind encouragement. Thanks also to Professor Savastano's research group, including Bruna Barra and Patricia das Neves, for their characterization of various natural fibers and their work regarding various methods of natural fiber treatment. Thanks also to the colleagues of Professor Savastano: Dr. Sérgio Francisco dos Santos, at Sao Paulo State University (Guaratinguetá Campus, Brazil), for helpful discussions, and the group led by Prof. Alcides Leao, at Sao Paulo State University (FCA Botucatu Campus, Brazil) for kindly furnishing leaf samples and information about curauá cultivation.

Professor Richard Robertson has been an extremely important part of my graduate studies at Michigan. As my co-advisor, he has been a trusted source of mentorship and has allowed me to pursue an unconventional research path within the Macro program. I greatly appreciate his wealth of composites knowledge, but I am especially grateful for his constant support and kind nature.

Thanks to Jeff Plott, Prof. Evgueni Filipov, Prof. Albert Shih, and Prof. Greg Keolian, all from the University of Michigan, for discussions and support on the 3D printing project. Thanks to Alan Olvera for the thermal characterization testing carried out for the curauá composite project. And thanks to Professor Nima Rahbar (Worcester Polytechnical Institute) for discussions regarding the slip-hardening mechanisms and numerical modeling of natural nacre, as well as about life as an academic researcher in general.

Thanks, as well, to Prof. Maria Lemos for her commitment to serve on my dissertation committee as a cognate member, and for enhancing my understanding of environmental sustainability considerations and context through several discussions and introductions. These sustainability considerations serve as motivation for all three of my materials design projects.

Thanks to Prof. Ravi Ranade, Devki Desai, Dr. Emily Herbert, Dr. Qian "Maple" Zhang, and soon-to-be Dr. Motohiro Ohno for being excellent research role models throughout my time in the Advanced Civil Engineering Materials Research Lab. Special thanks to Ravi, who has continued to be a resource for answers to all kinds of research related inquiries, and whose research findings have played an integral role in my own.

I'd like to also thank University of Michigan Macro program alumnus, Prof. Raymond Pearson, who mentored me in polymers science research at Lehigh University. I am sure that without his kind help and hospitality in his lab many years ago, I would not be graduating from the University of Michigan.

I also owe a huge thank you to the University of Michigan Civil and Environmental Engineering technicians, Bob Spence and Jan Pantolin for countless problem solving discussions, help with experimental logistics, instrument maintenance, troubleshooting, and training, and always being accessible and willing to help. Thanks also to Bob Fischer for machining and guidance in the fabrication of grips for the large dogbone specimen tensile testing apparatus.

I'd like to personally thank the University of Michigan Macromolecular Science and Engineering program coordinators, Nonna Hamilton and her successor Adam Mael, for their exceptional and genuine support. Both have gone above and beyond for both myself and others in the program, and always with a smile. The Macro program, and all Macro students, are incredibly lucky to have had Nonna and/or Adam as resources. Both Adam and Nonna have done so much behind the scenes to give each and every student the best chance at succeeding in the program. Thanks also to Macro Director, Prof. Mark Banaszak Holl for his consistent support and encouragement.

Thanks, as well, to the always-friendly, always-helpful University of Michigan Civil and

Environmental Engineering department staff.

My dissertation research has been supported by a number of funding sources, namely the University of Michigan MCubed program and The Macromolecular Science and Engineering program itself. The MCubed Program is a visionary research funding model pioneered by the University of Michigan to encourage truly innovative, collaborative, and cross-disciplinary research. The nacre-inspired composite design project and the 3D-printable ECC project both received seed funding from the MCubed program. The Macro program is also to be commended for its significant financial support offered to its students, including me, ensuring every student has the chance to succeed. Thanks to Adam Mael, Prof. Mark Banaszak Holl, and Prof. Rick Laine for continual and dogged support of this Macro family tradition. The curauá fiber work was financially supported by: FAPESP projects #2012/51467-3 and #2013/50107-6, the UM-FAPESP program, and the University of Michigan Graham Sustainability Institute.

Several material vendors also provided material donations to support this dissertation research. Thanks to Elkem for providing microsilica, to Headwaters Resources (Monroe, MI, USA) for donating fly ash materials (as made possible by the generosity and logistical support of Michael Hyland and Sarah Keller of Headwaters), and to Lafarge for donation of Class H “oil well” cement for the nacre-inspired composites project.

Thanks to Tessa Perez for being an exceptional proofreader and my best friend, and to her and her family for their continued love and emotional support on this journey.

And last, but certainly not least, I want to express my gratitude to my research advisor, Professor Victor Li. Professor Li has given me the opportunity to work on exactly the types of materials development projects I sought when I arrived at the University of Michigan. He has allowed me to design these research projects myself and around my own strengths as a researcher. Just as he promised me on my first day as a member of his research group, he has been a coach, not a boss. He has given me the resources, opportunities, and guidance to become a better writer, presenter, and scientist, and he has been extremely supportive of my personal and professional ambitions. It has been an honor and a privilege to work so closely with Professor Li, and with the technologies he has pioneered.

TABLE OF CONTENTS

LIST OF TABLES

LIST OF FIGURES

LIST OF APPENDICES

LIST OF ABBREVIATIONS

%CM: “Percentage of total cementitious material by weight”, a metric used herein to describe ingredient ratios (including non-cementitious ingredients) in matrix compositions; all types of cement, fly ash, and microsilica (in some cases) are considered in “total cementitious material”

ECCs: “Engineered cementitious composites”, a family of short, polymer fiber reinforced, cement matrix-based composites, characterized by a low volume fraction of dispersed, discontinuous fibers, tensile strain-hardening behavior, and a distributed microcracking pattern when subjected to tensile stresses above the elastic limit; also referred to as SHCCs, and colloquially as “bendable concrete”

HSHDC: “high strength high ductility concrete”, an ultra high strength version of ECC, used in this research as an SHCC model and primary component in nacre-inspired hierarchical composites

MPa: Megapascal, a metric pressure (stress) unit and equal to 1,000,000 newton (force) per square meter, or $1x10^6$ pascals

PP: polypropylene

PU: Polyurethane

SHCCs: cement matrix based composites exhibiting tensile strain-hardening behavior; includes short polymer fiber reinforced ECCs

VCP: vinyl coated polyester

ABSTRACT

Strain-hardening cementitious composites (SHCCs) are a family of cementitious materials that preserve the advantages of concrete as a construction material, while eliminating many of concrete's shortcomings. While concrete is weak and brittle in tension, SHCCs exhibit a degree of tensile ductility under extreme loading and material toughness hundreds of times that of concrete, providing enhanced durability and resilience for cementitious infrastructure. This research covers three materials design projects aimed at expanding the capabilities of the SHCC family, offering their durability and resilience benefits to new infrastructure use cases and enhancing those qualities in others.

First, the use of natural plant fibers, rather than synthetic polymer fibers, as the sole reinforcement in SHCC materials is explored as a route for material greening. Strategies to overcome the design challenges associated with the use of natural fibers are reported and a curauá fiber reinforced strain-hardening cementitious composite is introduced.

Second, the concept and micromechanical design considerations of strain-hardening cementitious composites are applied to cementitious materials designed for building-scale 3D printing. Automated additive manufacturing techniques, such as 3D printing, are poised to revolutionize the construction industry, offering benefits in time and cost efficiency and human safety. However, the full potential of building-scale 3D printing has been hampered by the required insertion of ancillary reinforcement, antithetical to the bottom-up, freeform 3D printing paradigm. By using SHCC materials as the primary printing material, these limitations could be removed, improving design freedoms, efficiency, and the inherent durability and resiliency of the printed structure. Compositional and processing strategies to achieve printability in SHCC

materials (and cementitious materials in general) are investigated and reported. Proof-of-concept printable SHCC materials are demonstrated, and their mechanical performance is characterized.

Third, enhanced mechanical property profiles of SHCC materials are pursued, as inspired by the structure and deformation mechanisms of a natural composite material found in seashells. Despite being composed 95% of a brittle chalk-like material, nacre exhibits remarkable tensile strength, tensile ductility, and toughness. Strategies of adapting nacre's hierarchical structural organization and associated deformation mechanisms to a large size scale and with materials relevant to infrastructural applications are explored and evaluated. SHCCs serve as an efficient means to achieve this structure and these mechanisms due to their characteristic tensile behaviors. These nacre-inspired composite design strategies are pursued as means to improve the holistic mechanical property profiles of SHCCs. Applied to the highest strength versions of SHCCs, these bio-inspired design strategies offer benefits to seismic, blast, and impact resistant infrastructure applications.

This research seeks broad impact by addressing the sustainability of infrastructure through material greening and improved durability and resilience of the fundamental building block of most modern infrastructure: cementitious materials. Parametric studies are used to design novel versions of SHCCs with new and useful characteristics, all while deliberately engineering the fiber, matrix, and interfacial properties to generate strain-hardening behavior. In addition to addressing specific compositional or performance targets, resulting in three novel types of functional SHCCs, each design project produces results and implications related to the others.

CHAPTER I

Introduction

1.1 BACKGROUND AND MOTIVATION

Concrete, by both weight and volume, is currently the most widely used engineering material in the world. It can be processed in large quantities, is relatively cheap, and performs efficiently in compression. Concrete, therefore, serves as the ubiquitous basis of our built environment.

However, concrete is not without severe limitations. Weak and brittle in tension, concrete fails under many typical loading modes and environmental conditions. A single crack can lead to rapid deterioration or cause total loss of load carrying capacity. The use of steel reinforcement to compensate for concrete's shortcomings in tension often compounds and accelerates degradation processes due to the additional tensile forces introduced by corrosion products [1-3]. As such a proliferate component of civil infrastructure, concrete's shortcomings are evident in everyday life, from poor road conditions and visibly deteriorating bridges, to the frequent and disruptive repairs of this infrastructure. The failures due to concrete's lack of durability and resiliency are not just an inconvenience to the public and drain on governmental budgets, but also threats to human safety and the well-being of our modern societies.

These shortcomings make concrete infrastructure, as constructed presently, unsustainable. Concrete's lack of durability and resiliency demand repeated repair events that consume valuable resources, including time, energy, and money. In the US, the deterioration caused by these issues is occurring at a rate greater than at which it can be repaired, evidenced by the "D+" grade of the nation's infrastructure condition as assigned by the American Society of Civil Engineers in their latest annual report card [4]. Additionally, the repair events that can be completed are

responsible for the majority of the carbon emissions (a measure of environmental impact) of concrete infrastructure, mainly due to traffic disruption [5]. Truly sustainable infrastructure would instead have long service life, dramatically reduced environmental impact, and the capacity to endure loading conditions, both of the present and of the future.

Beyond durability under normal service conditions, concrete infrastructure needs to withstand extreme loading events to ensure human safety in events like naturally occurring disasters, and even malicious attacks, of seemingly unlikely scale. Resiliency, defined as the ability to minimize the probability of failure, minimize the consequences of failure, and minimize the time between failure and a return to service, is also a shortcoming of typical concrete [6]. An improvement of the durability and resiliency of the concrete material used in critical infrastructure components would effectively address each of the requirements for sustainable infrastructure, significantly improving the sustainability of our built environment and the functioning of our modern societies.

With the advent of so-called "Ultra High Performance" concretes (UHPCs), the compressive strengths achievable in concrete infrastructural materials has risen to over 200 MPa in practice and nearly four times that in more controlled laboratory settings [7,8]. The design approach of UHPC is to eliminate flaws by promoting particle packing and extreme densification. This is a damage prevention approach. These UHPC materials are, however, even more brittle than normal concrete [9]. The use of steel fibers within these matrices has served to mitigate the catastrophic failure that can occur in tension, however these "fiber reinforced concretes" (FRCs) exhibit tension-softening behavior with still limited tensile ductility [9,10].

Taking a different approach to improved performance in concrete materials, strain-hardening cementitious composites have been invented and pioneered by Li [11]. Engineered Cementitious Composites (ECCs), also known more generally as strain-hardening cementitious composites (SHCCs) and colloquially as "bendable concrete", exhibit a characteristic distributed microcracking pattern and strain-hardening behavior when subjected to tensile loading above the elastic limit. The micromechanics of ECCs have been described previously in detail [11], and differ from those of other fiber reinforced concretes. In short, when the brittle cementitious

matrix first fractures in tension, the dispersed discontinuous fibers are able to bridge the crack, holding the crack to several tens of microns in width, while carrying the tensile load such that further opening of the microcrack (via fiber pullout) requires more energy than originating a microcrack elsewhere in the matrix. This cycle can be repeated many times, such that the composite is able to distribute deformation throughout and suppress brittle fracture failure. Rather than damage prevention, this is a damage management approach and it results in cementitious materials with toughness hundreds of times that of traditional concretes and even UHPCs.

As SHCC materials accumulate damage (in the form of microcracks) under tensile strain, they can support an *increasing* load, exhibiting the strain-hardening behavior typical of metal alloys. This behavior promotes a bend-before-break failure mode, prevents spalling, eliminates the need for steel reinforcement in many applications, and even creates new applications for large-scale cementitious materials [11, 12]. Additionally, self-healing behavior has been observed in these materials with exposure to moisture and air, such that stiffness can be regained and strength retained [13]. In these ways, SHCCs can contribute to durability and resiliency when used in place of traditional concrete materials.

The characteristic behavior of SHCCs can be leveraged in direct tension and bending, and even offers performance benefits in compression. Compatible with typical concrete processing methods, SHCCs preserve the advantages of concrete, while offering significant improvements in regard to concrete's shortcomings.

The characteristic distributed microcracking behavior of ECCs is generated in part by a low volume fraction of short polymer fibers, evenly dispersed throughout the cementitious matrix. The micromechanical interactions that allow the composite-scale strain-hardening behavior of SHCC materials depends on a balance of properties and parameters of three components: the fiber, the brittle matrix, and the interface between the two. The default behavior of short fiber reinforced cementitious composites is strain-softening behavior like that seen in many steel fiber reinforced concretes (FRCs); strain-hardening behavior is generated in a "sweet spot" of properties and parameters associated with the fiber, matrix, and interface. Compositional and

performance manipulation is guided by a micromechanics design basis very different from the simple dense packing approach of UHPC. Changing the strength of matrix, for example, must be compensated for with changes in the fiber, the interface, or likely both, if strain-hardening behavior is to be preserved.

1.2 RESEARCH THEMES AND OBJECTIVES

This research seeks broad impact by addressing the sustainability of infrastructure through material greening and improved durability and resilience of the fundamental building block of most modern infrastructure: cementitious materials. The materials design projects comprising this dissertation share the approach of improving the sustainability of infrastructure by expanding the utility of strain-hardening cementitious composites, thus introducing or enhancing the sustainability-related benefits SHCCs can offer to various segments of the civil engineering and construction industry.

The research presented herein is focused on the systematic composite design and development of three different groups of SHCC materials, each defined by specific performance or compositional targets, in a manner ensuring practical and impactful application to improve the durability and resilience of cementitious civil infrastructure. This research builds upon over two decades of pioneering SHCC-related work, and aims to make this class of materials applicable to new use cases and enhance performance in others. Each of the three materials design projects included in this research introduce and investigate novel approaches in the design of SHCCs to improve the diversity of property profiles SHCCs can offer. Additionally, the three projects are linked by the implications the research findings and conclusions of each have on the others.

The first design challenge is to use natural plant fibers instead of synthetic polymer fibers as the sole fiber reinforcement in a SHCC material. Renewable natural fiber in the place of synthetic polymer fiber is one route to greening SHCCs as this substitution reduces the embodied energy (total energy required consumed by the production processes required for a material or product) of the composite. A natural fiber reinforced SHCC would provide a greener alternative for

specific construction applications in which the higher strength synthetic fibers may not be necessary.

The discrepancies in physical characteristics, mechanical properties, and chemical properties between natural fibers and the synthetic fibers typically used for SHCCs create significant composite design challenges in generating strain-hardening behavior. Compositional and processing strategies to overcome these challenges and subsequently manipulate the mechanical properties of the resulting SHCCs are investigated.

The second design challenge is to design a SHCC compatible with the building-scale three-dimensional printing (3D Printing) additive manufacturing process. Additive manufacturing methods offer the potential of automation, efficiency, human safety, and architectural freedoms to the construction industry. The building-scale 3D printing industry is currently in its infancy, but experiencing recent growth and increased public awareness. Current state-of-the-art building-scale 3D printing processes are limited by the weak, brittle concrete materials used for printing. A printable strain-hardening cementitious material offers solutions to several of the major issues currently faced in building-scale 3D printing, including the weak "printable concrete", and requirement of insertion of additional reinforcement and high strength fill material.

This design project focuses on the manipulation of fresh state properties of ECCs to make ECCs compatible with existing 3D printing processes. The effect of the printing process on the mechanical performance of ECCs is also explored. The goal is to develop strategies and performance indicators to systematically guide printable ECC material design, rather than develop a singular printable SHCC material. In addition to creating 3D printing-compatible ECCs to provide solutions to the building-scale 3D printing industry, several proof-of-concept printable ECC materials are used to explore the potential benefits the 3D printing process can offer to general application of SHCCs.

Like the other two design challenges, the third project seeks to leverage the characteristic behaviors of SHCCs in novel hierarchical composite materials offering value proposition for critical structural and infrastructural applications. Unlike the other two design challenges, the

third project does not focus on how the primary components of ECCs (cementitious matrix, fiber, and the interface between the two) can be manipulated to impart new functionality and/or value, but rather explores a higher, metalevel of SHCC composite design: can SHCC materials be applied as a primary component in hierarchical composite materials for infrastructure to further enhance the mechanical benefits SHCCs offer? Again, this design project does not seek to produce a singular material, but a broadly applicable design approach and associated strategies. The envisioned outcome is "a rising tide [that] lifts all boats" in that the hierarchical design approach can improve the mechanical property profile of any SHCC material to which it is applied.

In fact, the inspiration for the third project literally comes from the seashore. Inspiration is derived from nacre, a natural material seen on the interior of seashells. Design features and associated deformation mechanisms proven to be responsible for nacre's impressive mechanical property profile are emulated on a much larger scale, adapted to materials useful for civil engineering applications for the first time. The characteristic tensile behaviors of SHCCs enable an efficient route to generate nacre-like structure and deformation mechanisms on a large-scale—overcoming a major bottleneck in the development of synthetic, nacre-inspired materials, particularly at large size-scales. Application of these nacre-inspired composite design schemes to those SHCCs on the upper end of the mechanical performance spectrum are of particular interest to push SHCC performance into property profile white spaces; however, the other end of the spectrum is also of interest to improve the performance of those SHCCs subject to the most limiting constraints.

While each of these projects are, for efficiency, undertaken and reported in a self-contained manner, their research findings and conclusions have implications related to each of the other design projects. For example, due to the micromechanical mechanisms that govern ECC performance, the relatively low average tensile strength of the natural fibers yields relatively low tensile strength natural fiber reinforced ECCs; the nacre-inspired composite design schemes may offer routes to expand the range of natural fiber reinforced SHCC applications via mechanical property profile enhancement. The building-scale 3D concrete printing process allows a high level of control over the geometry of (and fiber alignment within) cementitious members, and

produces a naturally layered structure; it can perhaps be employed to produce future large-scale, SHCC-enabled adaptions of nacre's complex hierarchically organized composite structure. Conversely, the lessons learned regarding various nacre-inspired design features may be able to inform and improve, if only indirectly, the design and manufacture of printed members and structures.

1.3 DISSERTATION ORGANIZATION

This document is organized into five chapters, corresponding to the three materials design projects comprising this dissertation research, plus this introductory chapter covering the common motivation, background information, and scope of this research, and a closing chapter with concluding remarks regarding this research. The next three chapters each report the specific motivations, research objectives, experimental approach and details, results, and conclusions of one of the materials design and development projects.

These three parts, in order, cover the design and development of a curaua fiber reinforced strain-hardening cementitious composite, design and development of self-reinforced cementitious materials for building-scale 3D printing, and SHCC-enabled, nacre-inspired approaches for durability and resilience in infrastructural materials.

REFERENCES
(CHAPTER I)

[1] Z.P. Bazant, Physical model for steel corrosion in concrete sea structures – application, J Eng Mech, ASCE, 105 (6), pp. 1155-1166, 1979.

[2] M. Ohtsu and S. Yosimura, Analysis of crack propagation and crack initiation due to corrosion of reinforcement, Constr Build Mater, 11 (7-8), pp. 437-442, 1997.

[3] B.H. Oh, K.H. Kim, S.Y. Jang, Y.R. Jiang, B.S. Jang, Cracking behavior of reinforced concrete structures due to reinforcing steel corrosion, J Korea Concr Inst, 14 (6), pp. 851-863, 2002.

[4] American Society of Civil Engineers. 2017 Report Card for America's Infrastructure, http://www.infrastructurereportcard.org/, July 31, 2017.

[5] Chandler, R.F. "Life-Cycle Cost Model for Evaluating the Sustainability of Bridge Decks: A Comparison of Conventional Concrete Joints and Engineered Cementitious Composite Link Slabs." A report of the Center of Sustainable Systems, University of Michigan, 2004.

[6] Bruneau, M., Chang, S., Eguchi, R., Lee, G., O'Rourke, T., Reinhorn, A., Shinozuka, M., Tierney, K., Wallace, W., von Winterfelt, D., A Framework to Quantitatively Assess and Enhance the Seismic Resilience of Communities, EERI Spectra Journal, Vol.19, No.4, pp.733-752, 2003.

[7] Shutt, C.A. "UHPC Joint Provides New Solution." Aspire, pp.28-31, Fall 2009.

[8] Richard, P. and M. Cheyrezy. Reactive Powder Concretes with High Ductility and 200-800 MPa Compressive Strength, P.K. Mehta. (Ed.) ACI SP-144 (V.4), Detroit, MI, pp. 507-518, 1994.

[9] Gettu, R., Bazant, Z. P. & Karr, M. E, Fracture Properties and Brittleness of High-Strength Concrete, ACI Materials Journal, 87(6), 608-18, 1990.

[10] Ultra High Performance Concrete (UHPC): Proceedings of the International Symposium on Ultra High Performance Concrete, Kassel, Germany, Ed. M. Schmidt and E. Fehling, 2012.

[11] V.C. Li, On Engineered Cementitious Composites (ECC): A Review of the Material and Its Applications, J. of Adv. Concr. Technol., Vol. 1, No. 3, 215-230 November 2003.

[12] M.D Lepech, and V.C. Li, Design and field demonstration of ECC link slabs for jointless bridge decks. Conf Proc ConMat'05, Vancouver, Canada, 2005.

[13] Herbert, E.N. and V.C. Li, "Self-healing of engineered cementitious composites in the natural environment", High Performance Fiber Reinforced Cement Composites 6, G.J. Parra-Montesinos, H.W. Reinhardt and A.E. Naaman (eds.), Springer, pp.155-162, 2012.

CHAPTER II

Curauá fiber reinforced strain-hardening cementitious composites

2.1 INTRODUCTION

With increasing urbanization and climate change concerns, the need for infrastructure that is more durable, more resilient to extreme loading, and more environmentally sustainable has been self-evident. While concrete is the most heavily used material in the world, and a key component of civil infrastructure, the brittle failures of concrete and repeated maintenance required of concrete infrastructure are well documented, prompting research and development of new concrete materials that possess tensile ductility: strain-hardening cementitious composites. These materials can offer durability and resilience, even in extreme loading conditions, and contribute to infrastructure sustainability via reduced repair events and extended service life [1-4]. The objectives of the present study are (1) to further the sustainability of ductile, strain-hardening cementitious composite materials through a focus on material "greening" using natural plant fibers, and (2) to highlight and expand the range of functional uses of natural fibers in construction applications.

2.1.1 Strain Hardening Cementitious Composites

In recent years, ductile concrete has been successfully designed [1,5,6]. Often referred to as Strain-Hardening Cementitious Composites (SHCCs) or Engineered Cementitious Composites (ECCs), this class of concrete materials possesses tensile strain capacity of 2-5%, two to five hundred times that of normal concrete. SHCCs have compressive strength ranging from 20 MPa to over 160 MPa. Their mechanical behavior, atypical for cementitious mortar-based composites, has earned them the colloquial nickname of "bendable concrete". They have been applied in full-

scale construction [1,7], including buildings and infrastructure for transportation, water, and energy.

A variety of polymer fibers, including poly(vinyl alcohol) (PVA), high-tenacity polypropylene (HTPP), and polyethylene (PE) have been successfully adopted as reinforcements in SHCCs [8-10]. Table 2.1 shows some characteristics of these synthetic fibers. The combination of fiber strength and diameter has made it feasible to design SHCCs with fiber volume content limited to 2% or less, following micromechanical principles [1,11].

Table 2.1: Properties of various synthetic fiber types used in ECC materials

Fiber Type	**Specific Gravity (g/cm^3)**	**Tensile Strength (MPa)**	**Young's Modulus (GPa)**	**Effective Diameter (μm)**
Polyethylene	0.98	2700	120	38
Poly Vinyl Alcohol	1.3	1600	42	39
High Tenacity Polypropylene	0.91	850	6	12

The defining and eponymous characteristic of SHCC materials is a strain-hardening tensile deformation behavior, providing damage tolerance and a high degree of durability in a variety of environments. Representative tensile stress-strain curves of this family of composites are shown in Figure 2.1. Strain-hardening behavior is reflected physically in these cementitious materials by the generation of a plurality of microcracks, each corresponding to a stress drop in the stress-strain curve for a particular specimen. In this way, SHCCs can distribute deformation, making them flaw and damage tolerant, and suppressing failure such that a much greater amount of energy is required to force failure than in other concrete materials.

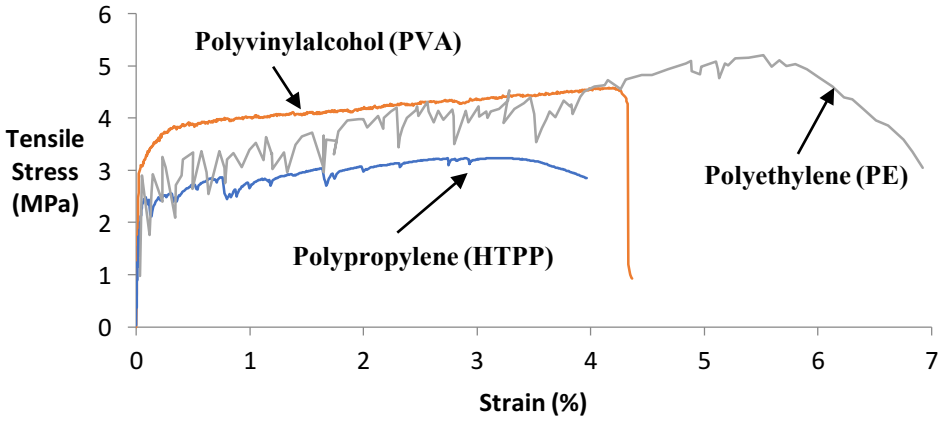

Figure 2.1: The influence of fiber type (PE, PVA and High Tenacity PP fibers) on ECC composite tensile strength and ductility

The micromechanics responsible for the ductile behavior exhibited at the composite level have been extensively documented [5,6,8,11]. The physical and mechanical parameters and properties of each fiber-matrix system must be considered and tailored to achieve the multiple microcracking and strain-hardening behaviors characteristic of SHCCs.

2.1.2 Toward More Sustainable Strain-hardening Cementitious Composites

While synthetic polymer fibers have many advantages as reinforcement for SHCC materials, they also have the disadvantage of being fibers with high embodied energy, being derived from crude oil. In the search for a less energy-intensive, renewable material with properties suitable to serve as the reinforcing fibers in SHCCs, this work investigates curauá plant fiber as an alternative to synthetic fiber. This chapter reports the findings of this investigation.

Previously reported studies of curauá-reinforced composites [12-15] have almost exclusively focused on the use of curauá fiber within polymer matrices, and for non-structural applications. This previous work has shown curauá to be an attractive natural fiber reinforcement, outperforming natural fibers more traditionally used in engineering applications like sisal and jute, but is by no means an exhaustive demonstration of curauá fiber's potential. By using curauá as the fiber reinforcement in an SHCC material, we aim to broaden its range of applications, while also improving the sustainability of SHCCs.

Although cellulosic components have been used in cement-based composites for many years, such composites are generally limited to thin sheet applications, manufactured by the Hatschek process with high fiber volume fraction, making them not particularly useful for general construction purposes. In contrast, SHCCs are designed for cast processing in precast plants or for on-site construction applications, allowing more versatility. The limited and randomly distributed short-fiber content in SHCCs is important for good workability for cast processing as well as for cost control. Demonstrating utility of curauá fiber as an SHCC reinforcement would greatly expand the range of applications for plant-fiber reinforced cementitious materials and would represent a significant step toward the popular use of renewable plant fiber in materials for construction applications.

2.1.3 Curauá Fiber

The curauá plant (Fig. 2.2) is native to the northern region of Brazil. The previously limited commercial cultivation of curauá has seen a significant uptick over the last fifteen years, as it has started to generate attention for its fibers' mechanical properties and use in non-structural composites in the automotive industry [16]. Still, scientific literature focused on curauá composite fabrication and properties is still relatively sparse compared to that of other natural fibers such as sisal and jute.

Curauá (*Ananas comusus* var. *erectifolius* (L.B.Smith)) is a monocotyledonous herbaceous species, belonging to the family Bromeliaceae [12]. Though there is only one species of curauá, there are five varieties. The most common varieties are "white", with light green leaves, and "purple", with reddish-purple leaves, each pictured in Figure 2.2. Curauá plants are only heavily commercially cultivated in the Santarém region, in the state of Pará, Brazil. Fibers of the purple variety have shown superior mechanical performance compared to the white variety [17], however the white variety is much more widely cultivated for agronomic reasons.

Figure 2.2: The white curauá variety (left), and the purple curauá variety, pictured with the plant fruit (right)

Details regarding the cultivation, harvest, and processing of the curauá plant and curauá fibers can be seen in Appendix II.1.

Curauá fibers have been recognized for their outstanding mechanical properties in comparison to other plant fibers [18-20]. Mechanical, chemical, and physical properties of the curauá fiber used in this study have been independently evaluated and are reported herein, including comparison to those values determined by other researchers and to those of other plant fibers traditionally used in engineering applications. These comparisons are made in Section 2.4.1.

The use of curauá fibers as reinforcement for ECC introduces challenges for composite design. Literature suggests significant water uptake by the porous and hydrophilic natural fibers and subsequent water release during curing, resulting in a large, porous, and weak interfacial transition zone (ITZ) between each fiber and the matrix [21-23]. Additionally, the large effective fiber cross-sectional area, presence of non-fibrous vegetal matter, and potentially contaminated surfaces characteristic of the as-supplied curauá fiber are likely to contribute to poor fiber-matrix interfacial bonding.

The goal of the present work is to report curauá composite compositions and processing shown to overcome these challenges and promote SHCC-type mechanical behavior, thus demonstrating the utility of curauá fiber in construction applications. A method of manipulating the mechanical property profile of the curauá-reinforced ECC is then explored, and thermal property characterization of the curauá composite, as related to potential cladding and façade applications, is reported.

2.2 EXPERIMENTAL APPROACH

The mechanical and physical properties of curauá fibers as supplied by the Pematec Triangel company are first independently characterized by a collaborating research group in Brazil under the direction of Prof. Holmer Savastano Jr., and are compared to previously reported values for curauá and other natural fibers. Various curauá-reinforced, short fiber cementitious composites, as inspired by the ECC micromechanical model for SHCCs, are then fabricated and tested.

Composite design is undertaken systematically with focus on the principal elements governing SHCC performance: matrix properties, fiber properties, and the properties at the interface between matrix and fiber, including the Interfacial Transition Zone (ITZ). Composite performance was initially evaluated via uniaxial tensile testing, with the goal of achieving multiple-cracking, strain-hardening behavior. Follow-up characterization includes testing in compression, bulk density measurement, and thermal property testing.

2.2.1 Experimental Variables

Experimental variables for the composite design can be classified as raw materials, formulation, or processing. As depicted graphically in Figure 2.3, this creates four categories of variables that guide strain hardening cementitious composite design: Matrix Composition, Curing Protocol, Fiber Parameters, and Fiber Treatments. Each of these categories explicitly tailors the performance of either the matrix or the fiber, and every category can influence the properties of the ITZ. Factors from each of these categories were considered and tested in combination to develop curauá-reinforced composite designs that exhibit strain-hardening behavior.

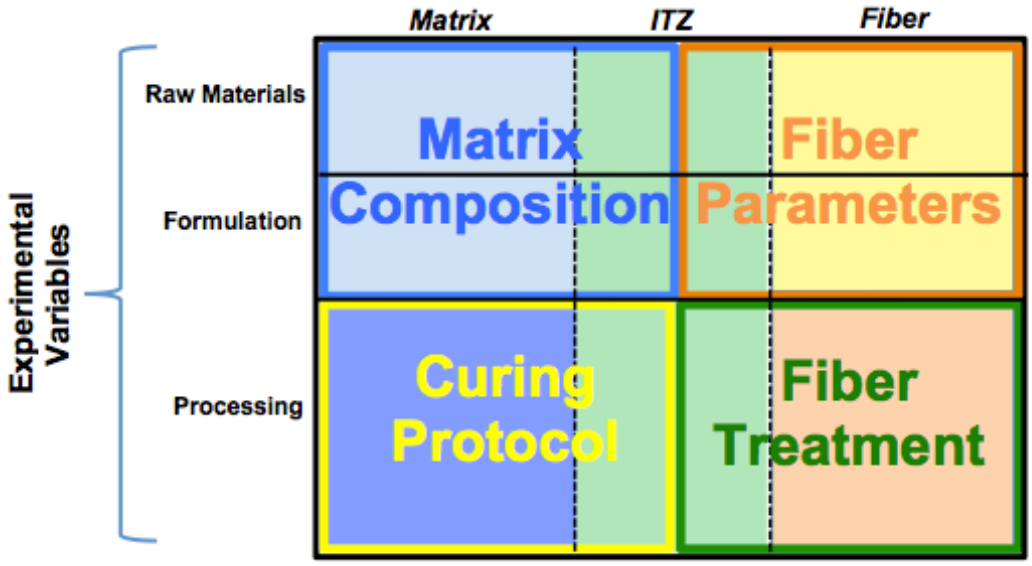

Figure 2.3: Categories of variables that guide design of curauá-reinforced SHCCs

Composite design insights and rationale relating to these four categories of variables, gleaned from preliminary testing and previous ECC design investigations, are broken down by category below.

Matrix Composition

The design of ECC involves a tailoring of the matrix to the particular fibers used as reinforcement, as dictated by micromechanical considerations. This requires matrix composition to be developed in an iterative fashion, following improvements in fiber and ITZ performance yielded by fiber treatments and changes to fiber parameters.

Due to the lower fiber strength of curauá fiber compared to synthetic polymer fibers previously used in SHCC design, low strength cementitious matrices are explored. Matrix properties depend upon the choice of raw materials and the formulation with which the raw materials are combined.

A high volume of fly ash is chosen to serve the dual roles of reducing cement content (contributing to material greening), and tailoring matrix strength to the strength of the fibers.

In addition to the choice of fly ash, several other variables are investigated for their influence on matrix properties as it related to composite performance. Microsilica, ground silica flour, and varied water contents are investigated to determine efficient means of matching matrix properties to the crack bridging capacity of the fibers. Additional methods of matrix property manipulation, including the use of recycled tire fines, varied ratios of fly ash and cement, and varied superplasticizer content were investigated in preliminary testing, but were not selected for inclusion in this study. Matrix design must be investigated in parallel with the other categories of variables to reach the delicate balance between matrix properties, fiber properties, and those of the ITZ, which allows strain-hardening behavior in the cementitious composite.

The specific matrix compositions that yielded successful strain-hardening ECC behavior, given the fiber treatments and parameters experimentally determined to be most effective, are listed in Section 2.3.1 and discussed in Sections 2.4.2 and 2.4.3.

Fiber Parameters

While most of the fiber properties in the as-supplied curauá fiber like strength and stiffness generally cannot be changed, some physical parameters of the fiber remain as free variables for composite design. In the context of "raw materials", given the selection of curauá fiber, these variables are the length to which the fiber is chopped and the effective fiber cross-sectional area. Due to fiber bundling, the effective fiber cross-sectional area is not necessarily a fixed, inherent property of the curauá fiber, and can be manipulated prior to mixing. In the context of the composite formulation, the primary variable is the number of fibers available for crack bridging at any given point within the composite. All three of these factors—fiber length, effective cross-sectional area, and number—are factors in the fiber volume fraction of the composite.

Of course, composite design must also be guided by processing considerations. Both fiber volume fraction and fiber length have a significant effect on the dispersion of fiber in the matrix and castability of the fresh paste, in addition to the tensile strain-hardening performance of the composite. The fibers become clumped and tangled during mixing if fiber volume fraction and/or length are too large. Longer fiber length and increased fiber volume fraction, however, provide higher fiber bridging capacity, promoting the desired distributed multiple microcracking

behavior of ECC. Fiber volume fraction and fiber length are therefore compromises between processibility and composite performance.

Curing Protocol

Curing protocol, the environmental conditions of the composites in the hour and days after casting, generally affects the strength of the brittle matrix, though it can also have implications for the ITZ. In this study, only composites subject to air curing protocols (ambient, low humidity curing environment) are reported. Saturated curing (sealed, high humidity environment) was explored in preliminary testing, and was seen to provide a boost in the strength of the brittle matrix, as indicated by increased first cracking strength of the discontinuous fiber reinforced composite specimens. In the design of SHCC, this first cracking strength must be consistently less than the crack bridging capacity of the fibers in the composite for strain-hardening and distributed micro-cracking to occur. Additionally, it is generally fiber bridging capacity, not matrix strength, that governs ultimate tensile strength of the strain-hardening composite. Therefore, in most curauá-reinforced cementitious composites, with given set of fiber treatments, air curing yielded the better strain-hardening performance, due to the reduced matrix strength.

Curing in a carbon-rich atmosphere is hypothesized to provide a future route to strengthen the interfacial bonding between fiber and matrix, by reducing the size and porosity of the ITZ.

Fiber Treatment

Fiber treatment was explored because of the poor fiber-matrix interfacial bonding initially observed. Literature suggests significant water uptake by the porous and hydrophilic natural fibers and subsequent water release during curing, resulting in large, porous, and weak interfacial transition zones (ITZ) between the fiber and matrix [21-23]. Additionally, the large effective fiber cross-sectional area, presence of non-fibrous vegetal matter, and potentially contaminated surfaces characteristic of the as-supplied curauá fiber likely contribute to poor fiber-matrix interfacial bonding. Plasma treatment, silane coupling agent, cleaning processes, and several “debundling” procedures are investigated.

Methane cold-plasma treatment was investigated in preliminary testing as a means of making the curauá fiber surface more hydrophobic, based on work by Barra et al. (2012) with sisal fiber [21]. An increase in hydrophobicity of the fiber surface was hypothesized to decrease water absorption, leading to decreased porosity and size of the ITZ, and therefore an improved fiber-matrix bond. While shown to improve composite performance over the untreated fiber case, plasma treatment produced inconsistent and inferior composite performance compared to that of composites prepared instead with a liquid fiber-matrix coupling agent. Use of the bonding agent was therefore elected instead of plasma treatment for the curauá reinforced strain-hardening composites reported in this study.

Vinyltriethoxysilane (VS) was investigated because of the reported efficacy of silane coupling agents in bonding polymeric fibers (natural and synthetic) to various types of matrices. This particular vinyl-silane coupling agent was chosen for fiber-matrix bonding in the siliceous, cementitious matrix based on work reported by Ranade (2014) [24]. The proposed mechanism for enhanced fiber-matrix bonding is "a durable bond between the siliceous inorganic material [of the matrix] and the organic material of the fiber[s]", made possible by the two functional groups of the silane [24]. A possible secondary mechanism is a reduction in water/cement ratio, due to the VS withdrawing water from the fresh paste via hydrolysis [24]. The reduction in matrix porosity around the fibers due to this hydrolysis and the chemical bonding due the functional groups of the VS may each contribute to a higher resistance to fiber pullout in the curauá fiber composite.

A debundling fiber treatment was investigated as a means of reducing the effective cross-sectional area of the curauá fiber. This debundling was done via manual combing of the continuous fiber with a straight-tooth, metallic comb. Beyond minimizing fiber bundling, this combing process also serves to remove non-fibrous vegetal material and weak, damaged, or tangled fiber. All three of these effects theoretically contribute to enhanced crack-bridging capacity for a given fiber volume fraction. This process was used in all strain-hardening curauá composites reported in this study, and is therefore not explicitly a variable. It is described in more detail in Section 2.3.2.

An alternative debundling process, which involved manual grinding of chopped fibers between rough surfaces, was also investigated in preliminary work. This process was abandoned in favor of the combing process due to concerns of damaging the structure (and thus the mechanical strength) of the curauá fiber, though it did yield improved composite performance compared to that of composites with no debundling treatment.

A cleaning treatment, referred to hereafter as "soaking", was also conducted on fibers to ensure no adverse affects on fiber-matrix bonding due to contaminants on fiber surfaces. The soaking and drying cycle may also serve to collapse the hollow lumen of the curauá fiber, which may reduce water absorption during composite processing. Again, this treatment was applied to all successfully strain-hardening composites reported herein and is thus discussed in more detail in the "composite processing methods" section (Section 2.3.2), rather than as a variable, here.

2.3 MATERIALS AND METHODS

2.3.1 Materials

Due to its commodity status, the white variety of curauá fiber was chosen over the other varieties to be investigated in the present study. Fiber used in this study was purchased from Pematec Triangel, a company based in Brazil. Pematec harvests from private farms in the state of Pará and only cultivates the white variety of curauá. The commercial price of this fiber in the Brazilian market is approximately US$1.3/kg, according to Pematec as of February 2015. Fibers were supplied in the uncut form (0.5 m filaments and longer).

Table 2.2: Experimental compositions of curauá-ECC cementitious matrices highlighted in this study, reported as a percentage of total cementitious material by weight, with the exception of the fiber content (percent by volume).

Mix	Microsilica	Ground Silica	Type I cement	Fly Ash	Water	Vinyl Silane	ADVA 190	Fiber (%vol)
V0	0.0	0.0	26.3	73.7	28.9	1.0	0.3	4.4
V1	20.0	0.0	26.3	73.7	33.5	1.0	0.3	4.4
V2	20.0	0.0	26.3	73.7	33.5	2.0	0.3	4.4
V3	15.0	5.0	26.3	73.7	33.5	2.0	0.3	4.4

The four cementitious composite compositions highlighted and evaluated in this study are listed in Table 2.2.

Using the industrial byproduct fly ash (Class F) as a pozzolan, the content of energy-intensive cement can be reduced. The combined use of renewable plant fiber and industrial waste-stream fly ash contributes to the overall goal of producing a "greener", lower embodied energy ECC material.

In addition to Type I Portland cement, and Class F waste-stream fly ash, Elkem 955 microsilica (silica fume), US Silica Sil-Co-Sil 75 ground silica, W.R. Grace ADVA 190 high-range water reducing admixture (HRWRA), and vinyltrimethoxysilane (VS) coupling agent were used in this study. Additional information regarding the chemical composition of the ingredients can be found in Appendix II.2.

Vinyltriethoxysilane (VS) was investigated because of the reported efficacy of silane coupling agents in bonding polymeric fibers (natural and synthetic) to various types of matrices. This particular vinyl-silane coupling agent was chosen for fiber-matrix bonding in the siliceous, cementitious matrix based on work reported by Ranade (2014) [24].

Matrix composition was treated as a variable in this investigation to properly tune composite behavior. With the exception of fiber content, compositions are reported herein as a percentage of the total cementitious material (cement plus fly ash), by weight, and this metric is abbreviated as % CM. Fiber content is reported as percentage by volume.

2.3.2 Composite Processing Methods

The first step in composite processing is preparation and treatment of the natural curauá fibers. Continuous (0.5-1.0 m) curauá fibers were first subjected to a debundling treatment. This debundling was done via manual combing of the continuous fiber with a straight-tooth, metallic comb (pictured in Figure 2.4 with a pencil for scale). The 2.5mm and 1.5mm spaced sets of teeth on the comb were used sequentially, in that order, in the combing process. The direct effect of this combing process on the fiber appearance is depicted in Figure 2.5. Beyond minimizing fiber

bundling and reducing effective fiber diameter, this combing process also serves to remove non-fibrous vegetal material and remove weak, damaged, or tangled fiber. All three of these effects theoretically contribute to enhanced crack-bridging capacity for a given fiber volume fraction.

Figure 2.4: A straight-tooth, metallic comb used for a debundling treatment of continuous curauá fiber prior to chopping (shown with pencil for scale)

Figure 2.5: The appearance of the continuous curauá fibers prior to combing (left) and after combing (right), illustrating the effect of the treatment

After being gently combed to "open up" the fiber bundles, the as-received continuous curauá fiber was then soaked in water at elevated temperature (80 C) for at least 18 hours. Water was replaced several times during this period to most effectively eliminate contaminates that may have been removed from the fiber surfaces. The continuous fibers were then dried at 90 C for at least 12 hours and then vigorously re-combed to eliminate bundling that occurred as a result of the drying process. It was observed that this soaking process caused a slight color change of the fiber, with the treated fiber being a paler shade of its original yellowish color.

Fibers are chopped after the second combing. Throughout this study, curauá fibers were manually chopped to length using a guillotine-style paper cutter. A significant distribution of fiber lengths was seen even when a specific length was targeted, therefore fiber lengths are reported as a 10 mm range. Fibers 10-20mm in length were used for all composites reported.

The dry, pozzolanic materials were mixed for 3 min. in a small (4.7L bowl volume) planetary mixer at approximately 120 rpm prior to the addition of water and superplasticizer. Batch size was approximately 1.0 L. Cut fibers were introduced to the thoroughly mixed paste in small amounts to aid dispersion. Once all fibers were added, mixing continued for an additional 2 min. with the last minute at a higher rate (~255 rpm) of mixing, as demonstrated by Felokoglu et al. (2014) to improve dispersion of fibers in HTPP-ECC.

The fresh paste, with dispersed fibers, was cast into continuously vibrated, open molds for dogbone-shaped specimens (33cm long, 1.27cm thick, with an 8 x 3 cm gage section) as recommended by the Japanese Society of Civil Engineers (JSCE), and cube (50 mm) specimens. Specimens were demolded after 2 days. Composite specimens were tested 28 days after casting after undergoing ambient air curing.

2.3.3 Fiber Characterization

Mechanical characterization of the curauá fiber was conducted by a collaborating research group at USP-Pirrasununga (Brazil). Direct tensile testing was carried out in a Universal Testing Machine MTS Servo hydraulic Test Systems, using a set-up composed of mechanical grips, 100 N load cell and crosshead speed of 0.2 mm/min. Approximately 40 samples, 40mm in length, were tested utilizing a procedure previously used by Barra (2014) and tensile strength and modulus of elasticity were determined [26]. For the calculation of the cross section of the fiber, an elliptical shape was assumed for the filaments. Using a correction factor based on the direct measurement of 40 specimens, cross-sectional area of each test specimen fiber was calculated from an average thickness measurement. An optical microscope was used for the measurements of the average thicknesses of the fibers.

The specific density of the fibers was obtained using a Quantachrome Instruments helium gas multipycnometer. The chemical composition of the fibers, regarding the lignin and holocellulose, was determined using the procedure by Morais et al. (2010). The lignin content was assessed using the procedures indicated in the TAPPI "T 203 cm-99" standard. The hemicellulose content is determined by the difference between holocellulose content and alpha cellulose content. The micrographs were taken using a SEM operating with backscattered electrons (BSE) and voltage of 15 kV.

2.3.4 Composite Testing

For uniaxial tensile testing of the curauá fiber composites, the dogbone specimens were gripped along their slanted edges via a wedge grip. Adequate degrees of freedom were provided by the grip apparatus to ensure near uniaxial direct tension along the longitudinal axis of the specimen. Displacement controlled tensile tests were performed at a rate of 0.005 mm/s. Strain was calculated from the average of the extension of two LVDTs mounted with the specimen normalized by the gage length. The tensile stress was calculated from the loading force recorded by the Instron load cell and the cross-sectional area of the dogbone specimens' gage section (~381 mm^2). Ultimate tensile strength is reported herein as the stress at 95% of the maximum load sustained by each composite. Strain capacity is reported as the strain at maximum stress carried by the composite prior to terminal stress decay.

Uniaxial compression testing was conducted with 50 mm cube specimens cast and cured with the same procedure as the dogbone specimens. A loading rate of ~50 psi/s was used, based on recommendations of the ASTM C109 international standard. Compressive strength is reported as the stress at the maximum load sustained by the composite.

Composite bulk density, ρ_{bulk}, was calculated using Eqn. 1, where dry mass, M_d, is measured after specimens are dried at 80°C for at least 12 hours, saturated mass, M_s, is measured after soaking in water for over 12 hours, and immersed mass, M_i is measured while specimens are suspended in water after soaking for over 12 hours.

$$\rho_{bulk} = (M_d) / (M_s - M_i) \qquad (1)$$

Bulk density accounts for interconnected voids and the inherent porosity of the natural fiber that contribute to the composite's thermal properties, and is therefore relevant for comparison between curauá-ECC compositions. However, in the calculation of thermal diffusivity, specific density is used.

Specific density was measured with a Quantachrome MICRO-ULTRAPYC 1200*e* using ultrahigh purity helium as the measurement gas. An average density was calculated using 5 consecutive measurements with a deviation less than 0.600%. Specific density characterization reported in this study was conducted by collaborating author Alan Olvera.

Thermal conductivity, thermal diffusivity, and specific heat capacity measurements were also conducted by collaborating author Alan Olvera. This thermal characterization was conducted via the laser flash method using a commercial apparatus (LFA 1000, LINSEIS). Measurements were completed under dynamic vacuum (~10^{-2} Torr) through the approximate temperature range 25 °C to 100 °C. The instrument precision on the thermal diffusivity data is ±6%. A NIST certified standard (Pyroceram 9606) was measured simultaneously with all samples for calculation of the specific heat capacity by a comparative method. Thermal conductivity was calculated using the equation 2, where D is thermal diffusivity, C_p is the specific heat capacity, and ρ_s is the specific density of the sample.

$$\kappa = DC_p\rho_s \qquad (2)$$

2.4 RESULTS AND DISCUSSION

2.4.1 Curauá fiber characteristics

The mechanical and physical properties of the curauá fiber used in this study are reported in Table 2.3. Also measured, for comparison, are those values for piassava, coir, and sisal fibers. This characterization was conducted by collaborating researchers based in Brazil [25].

Table 2.3: Mechanical, chemical and physical properties for vegetable fibers

Properties/Fibers	**Curauá**	**Piassava**	**Coir (*)**	**Sisal (*)**
Mechanical:				
Tensile strength (MPa)	620 ± 132	61 ± 18	83 ± 22	344 ± 94
Young's modulus (GPa)	41.7 ± 9.9	1.82 ± 0.46	1.4 ± 0.5	7.9 ± 2.8
Chemical composition:				
α-Cellulose (%)	69.0 ± 0.39	43.23 ± 0.18	45.46 ± 0.11	61.77 ± 0.20
Hemi cellulose (%)	10.0 ± 0.12	8.34 ± 0.27	12.66 ± 0.33	20.72 ± 0.35
Lignin (%)	13.0 ± 0.18	50.05 ± 0.51	35.36 ± 0.18	12.42 ± 0.24
Specific density (g/cm^3)	1.42 ± 0.047	1.57 ± 0.05	1.20 ± 0.012	1.42 ± 0.001
Average x-sect. area (mm^2)	0.012 ± 0.011	0.307 ± 0.188	0.097 ± 0.029	0.034 ± 0.013

(*) from Barra (2014) [26]

Table 2.4: Average properties for Brazilian fibers as reported by Satyanarayana et al. (2007)[18] and Tomczak et al.(2007)[19]

Property/Fiber	**Curauá**	**Piassava**	**Coir**	**Sisal**
Tensile strength (MPa)	125-300	134.58-142.9 / 108.5-147.3	95-174	324-329 / 577
Modulus of elasticity (GPa)	30-80	1.07-4.59	2.5-4.5	19.00
Elongation at break (%)	4.5-6	6.4-21.9	13.7-41	2-2.5
Microfibrilar angle	18.8	na	51	20
Diameter (μm)	97	na	40-400	18/100-300
Density	0.92	na	1.39-1.52	1.26-1.33
α-Cellulose (%)	70.7-73.6	31.6	43.4-53	74-75.2
Hemicellulose (%)	21.1	na	14.7	10-13.9
Lignin (%)	7.5-11.1	48.4	38.3-40.77	7.6-7.98
Crystallinity (%)	75.6	na	43-44	72.2

na = not available

The values reported here can be compared to values (seen in Table 2.4) previously reported [18,19]. The significantly higher tensile strength of curauá reported in Table 2.3 can likely be attributed, in part, to the calculation of the stress values using a noncircular, bean-shaped cross-section, rather than a circular estimation. We believe that the bean-shaped cross-section is a more accurate representation of the true cross-section, and therefore giving a smaller cross-sectional area and more accurate strength values.

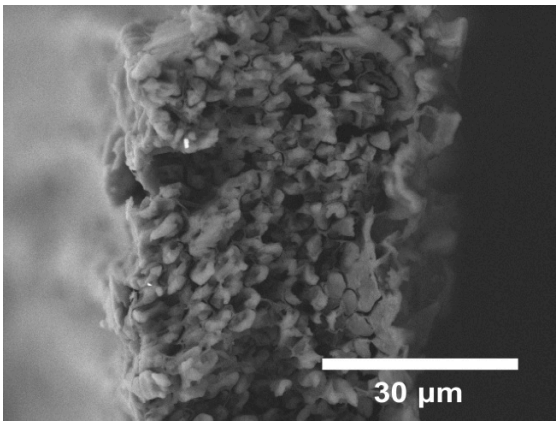

Figure 2.6: SEM micrograph of the bean-shaped cross section of curauá fiber obtained by cryofracture

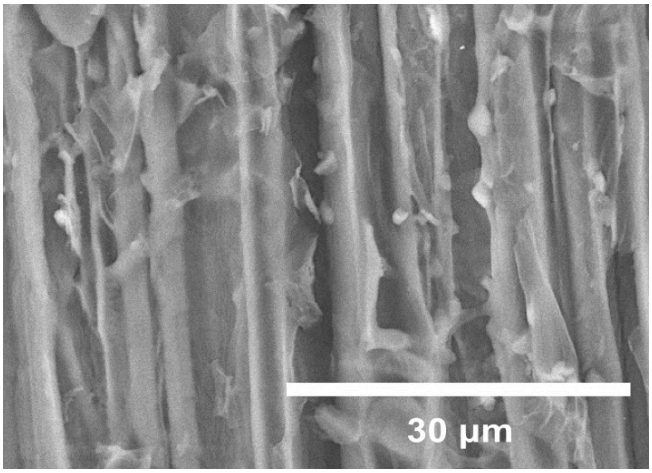

Figure 2.7: Lateral external surface of a curauá fiber taken by SEM

The SEM micrograph in Figure 2.6 depicts the irregular shape of the cross section of the curauá fiber, showing that it should not be approximated as an oval or circular shape. Using cryofracture, it is also possible to see the arrangement of unitary cells in the cross section, as well as the open spaces of the internal lumen of each cell, which represent a significant number of internal voids. Figure 2.7 depicts the lateral surface of the macro-fiber evidencing the open structure and the existing spaces between unitary cells. Such open morphology can facilitate the penetration of moisture and degradation agents into the unprotected fiber surface—challenges for composite design.

Further analysis of the mechanical, physical, and chemical properties of these natural fibers can be found in Soltan et al. (2017) [25].

It is important to note that plant fibers in general are subject to significant variation in mechanical, physical, and chemical properties due to the plant conditions (age of the plant, from where on the plant fibers are extracted, etc.), soil constituents, and climate variables. In addition, the procedures of extraction can influence the mechanical performance of the fibers. The shape and morphology of the cross-section of the plant fibers, and thus mechanical properties, are also variable along their length, generally correlated to the distance from the main stem. Specific experimental procedures, such as measurement of tensile strength and modulus, depend on determination of an individual fiber's cross-sectional area in order to calculate accurate values. This introduces ranges of properties when cross-sectional shape varies between fibers and along the length of an individual fiber. Mechanical properties of natural plant fibers, such as the curauá characterized and used for composite reinforcement in this investigation, should be understood to be a distribution rather than the more discrete values of synthetic fibers.

The distribution of curauá's mechanical properties represents a marked difference between curauá-reinforced cementitious composites and synthetic polymer fiber-reinforced ECC materials, presenting an additional challenge to composite design.

2.4.2. Curauá-ECC mechanical properties: Parametric studies

Fiber volume fraction

Early tests proved the need for fiber volume fraction greater than the 2.0% amount typically used for polymer fiber reinforced ECCs, due to the much larger curauá fiber cross-sectional area (fewer fibers available for crack bridging at a given volume fraction) and weak fiber-matrix bonding. Figure 2.8 shows the tensile strain softening behavior observed for the composite reinforced with 2.0% by volume of 10–20 mm curauá. Fiber bridging capacity with 2% by volume of fibers was not sufficient to generate any multiple cracking behavior. Instead, these specimens failed by the slow opening of the first crack in the matrix.

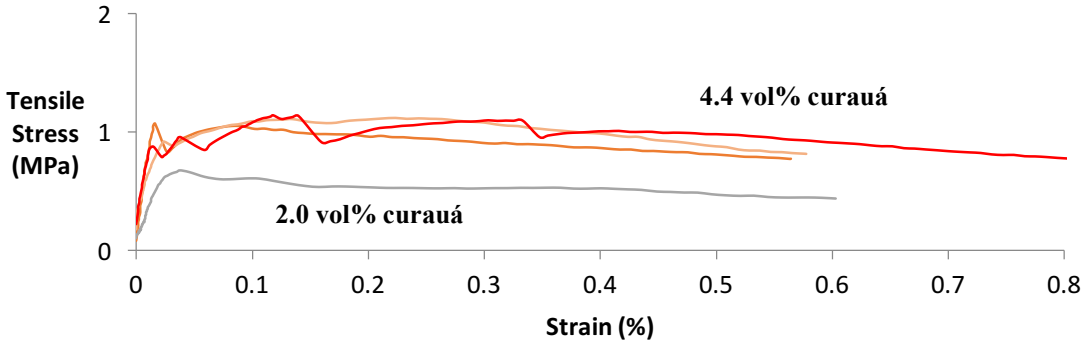

Figure 2.8: Comparison of the typical tensile behavior of 2.0% by volume curauá fiber (10–20 mm) reinforced composite and the range of tensile behavior observed for the 4.4% case

Mixing trials showed that at fiber volume fractions above 2.0%, curauá fibers longer than 20 mm caused tangling and poor dispersion. When fibers were cut to lengths less than 20 mm, fiber volume could be increased at least four fold without entangling during mixing, provided a higher water content is used. However, high fiber volume fractions, and their associated large water contents, resulted in extremely porous and weak composites. It was seen that fibers are the primary source of porosity in the composite.

Fibers 10–20 mm in length were able to be mixed, and dispersed well, up to a 4.4% volume fraction, with a reasonable water content of ~29% of the total cementitious material, by weight (% C.M.). As seen in Fig. 2.8, these parameters result in promising composite behavior, although lacking further parametric manipulation, multiple cracking and strain-hardening are still limited. As a compromise between the observed processing limitations caused by fiber entanglement, composite porosity, and the requirement of fiber bridging capacity, a 4.4% volume fraction of 10–20 mm fibers are the chosen fiber parameters for the discontinuous fiber reinforced composite specimens throughout the current study.

Vinyl-silane coupling agent

Vinyltriethoxysilane (VS), in liquid form, was added and thoroughly mixed into the fresh paste just prior to casting. The performance of curauá-reinforced composites with three varying doses of VS (0.0, 0.5, and 1.0% C.M.), are compared in Table 2.5. The performance of these VS-enhanced composites was aided by the “combing” fiber debundling process and the “soaking”

fiber cleaning process, each described in Section 2.3.2. It is seen that continuing to increase VS content, with otherwise identical composition, weakens the composite, perhaps as a result of contributing to the excess liquid in the fresh paste state.

Table 2.5: Mechanical performance of curauá-reinforced composites with varying doses of vinyltrimethoxysilane (VS). All three composites include 4.4% by volume of curauá fiber.

VS Content (%C.M.)	1st Crack Strength (MPa)	Ultimate Tensile Strength (MPa)	Strain Capacity (%)	Crack Distribution
0.0	1.2 ± 0.1	1.2 ± 0.10	0.1 ± 0.0	1-2 localized, cracks
0.5	1.8 ± 0.0	2.4 ± 0.01	0.6 ± 0.2	19-25 tight cracks
1.0	1.6 ± 0.2	2.2 ± 0.16	0.8 ± 0.1	23-35 tight, well-distributed cracks

Figure 2.9: Distributed, multiple cracking pattern of the V0 curauá-ECC specimens under direct, uniaxial tensile loading (applied in lateral direction). The surface has been painted white prior to testing to enhance crack contrast.

The 1.0% C.M. VS-enhanced composite, referred to hereafter as the V0 composite (see Table 2.2 for complete composition), successfully demonstrates the characteristic ECC tensile behavior. As illustrated in Fig. 2.9, the V0 composite exhibits the tight, well-distributed microcracks associated with the tensile strain-hardening mechanism of ECC. When microcracks are well-distributed and crack widths remain tight, deformation is spread throughout the material, without localizing, enhancing tensile ductility and suppressing failure. Measured after unloading, the vast majority of the 30+ cracks that appear in the gage section of this specimen, which has been tested beyond its strain capacity (i.e. beyond "failure"), remain under 20 μm in width. Even the largest crack, the crack that eventually caused failure of the specimen, is measured at only 50 μm in

width. This is desirable because tight crack widths have proven to be an important factor in the inherent and autogenous self-healing behavior of ECC materials [2].

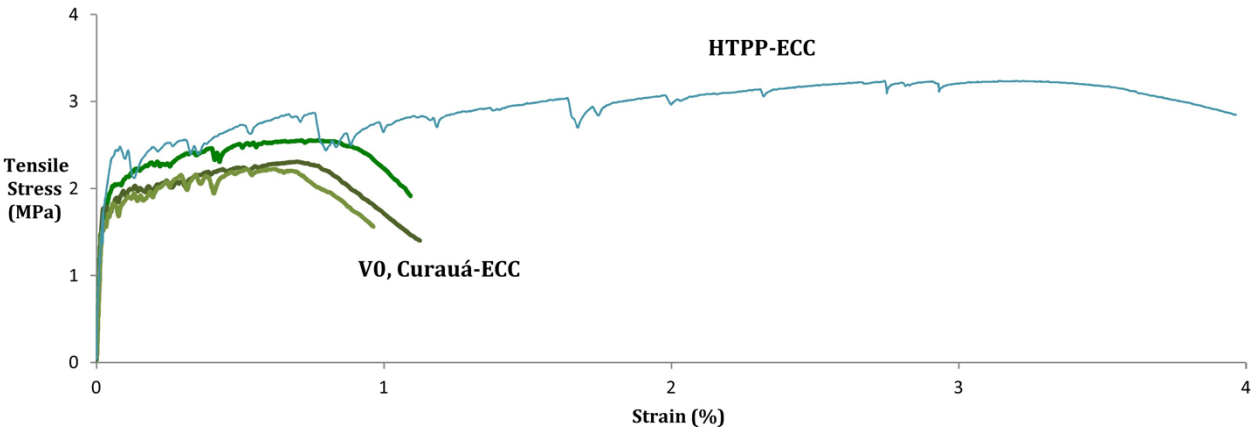

Figure 2.10: The range of typical tensile performance of the V0 curauá fiber ECC, illustrated by three representative curves (green), compared to a typical performance of High Tenacity Polypropylene-ECC (blue).

The V0 composite exhibits an average ultimate tensile strength of (2.2 ± 0.2) MPa, an average tensile strain capacity of (0.8 ± 0.1)%, and average compressive strength of (12.3 ± 0.4) MPa. A representative range of stress-strain curves for the V0 composition is given in Fig. 2.10 and compared to ECC reinforced with synthetic, high tenacity polypropylene fibers.

The strain capacity of the curauá-ECC cannot match the HTPP-ECC, likely because of the limited number of fibers available for contribution to crack bridging. The average cross-sectional area of curauá is over 100 times larger than that of the HTPP fibers, meaning that for a given volume fraction, there are fewer fibers dispersed throughout the composite and far less fiber-matrix interfacial surface area. Even at over double the fiber volume fraction of HTPP-ECC, there are not as many individual fibers at any given crack site to share the load that has been transferred to the fibers from the brittle matrix. Each fiber can only offer a nominal resistance to crack opening via friction generated by the fiber pullout necessary for the composite strain-hardening mechanism; too strong of a fiber-matrix bond would cause fiber rupture, which would be deleterious to strain-hardening behavior. Additionally, the curauá fibers are much more prone to fiber bundling that increases the effective cross-sectional area even further, compared to the synthetic polymer fibers. This issue of the curauá fiber's large effective cross-sectional area leads

to crack bridging capacity being exhausted at lower strains than in HTPP-ECC, despite impressive microcracking saturation throughout the gage sections of the dumbbell-shaped curauá-ECC test specimens.

The cementitious mortar matrix of the V0 composite (listed in Table 2.2) was derived using water content and the fly ash:cement (FA:C) ratio to properly tune matrix strength according to the crack-bridging capacity of the fiber. When higher water contents were used, higher porosity reduced compressive strength to unacceptable values. When lower FA:C ratios were used, the matrix strength was higher than the crack-bridging capacity of the fiber, generating only localized cracking and strain-softening behavior. Other means of manipulating matrix strength and porosity, such as the use of recycled tire rubber and varied HRWRA (ADVA 190) content, did not yield improved composite behavior and unnecessarily increased the bill of materials. The balance of water content and FA:C ratio described in Table 2.2 for the V0 composition allows fresh cement properties sufficient for effective mixing and fiber dispersion, as well as desirable tensile properties of the cured composite.

While the V0 composition exhibits impressive tensile properties, meeting the goal of producing ECC-type behavior with natural curauá fibers, its compressive strength (~12.3 MPa) limits the composite to a set of non-structural construction applications. Microsilica, however, was able to boost composite strength while preserving the multiple-cracking, strain-hardening behavior.

Microsilica

Microsilica (MS) was introduced as a means of boosting composite strength via increased bulk density. The compositions V1, V2, and V3, detailed in Table 2.2, represent the MS-enhanced compositions that most consistently exhibited the requisite tensile strain-hardening behavior of ECC materials. Their tensile performances are graphically illustrated in Figure 2.11 and their compressive strengths are compared in Figure 2.12.

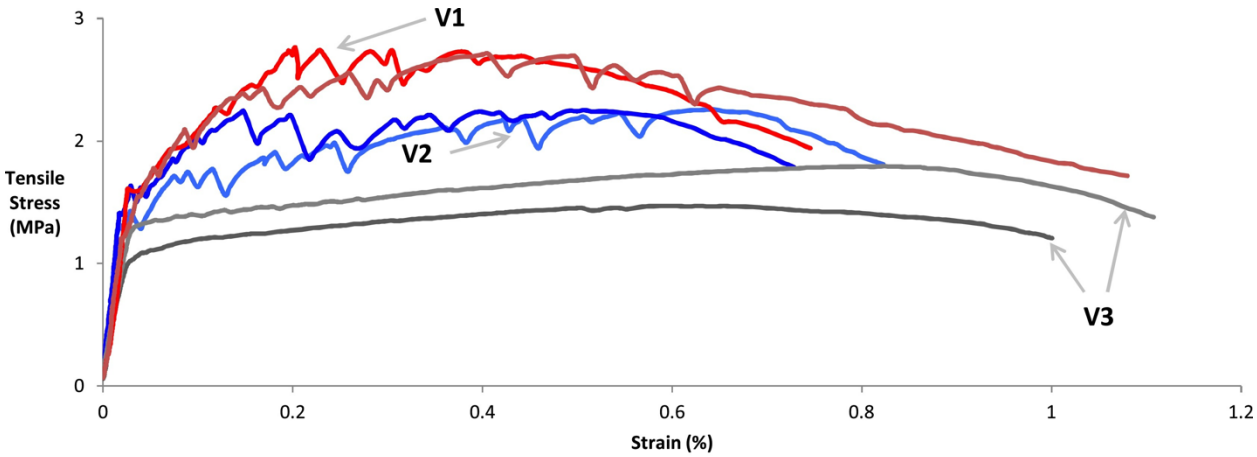

Figure 2.11: The V2 specimens (blue) show a balance between the tensile strength of the V1 composition (red) and the strain capacity of the V3 composition (gray)

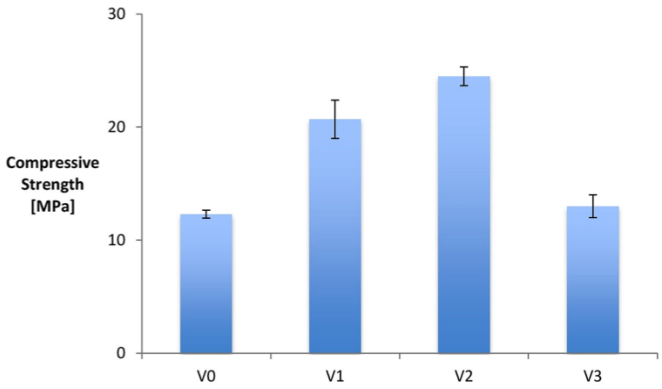

Figure 2.12: The addition of 20% C.M. microsilica boosts compressive strength of the curauá-reinforced ECC, however, a small substitution of ground silica appears to negate this effect. The increase in V-S has a modest effect on compressive strength of the MS-modified composition.

A 20% C.M. (in relation to cementitious mass) addition of MS is seen to successfully boost the compressive strength of curauá-reinforced ECC to values over 20 MPa, qualifying it for structural applications, while maintaining strain-hardening behavior. The MS (0.1–1.0 μm particle size) contributes to strength-promoting densification, as evidenced by the (1.62 ± 0.03) g/cm^3 bulk density of the V1 composite compared to (1.51 ± 0.05) g/cm^3 for the V0 composite.

2.4.3 Trade-off between tensile and compressive properties of SHCCs

The tensile and compression performance of the V1-V3 composites, as presented in Figures 2.11 and 2.12, illustrate a general principal of SHCC/ECC composite design. There exists a trade-off between strength and tensile strain capacity for a given fiber-matrix system. Compressive strength of the composite is largely based on the strength of the brittle cementitious matrix, which is indicated in tension by the stress at which the first crack occurs (i.e. where elastic behavior of the matrix is exhausted). When the first crack strength of the composite is reduced (via increased water or fly ash content, for example), tensile strain capacity can be improved, however, compressive strength will suffer. In the natural fiber reinforced SHCCs reported here, for a given coupling agent content and set of fiber treatments, higher strength and larger tensile strain capacities *can* each be attained, but generally at the sacrifice of the other.

The V0 and V2 composites represent a compromise between compressive strength and tensile strain capacity, allowing robust strain hardening. However, due to the higher strength of the V2 matrix, the V2 composite cannot match the strain capacity of the V0 composite, as seen in Fig. 2.13. The V0 composite also exhibits a more well-distributed cracking pattern with a greater number and tighter width of cracks. These composites demonstrate the ability of SHCCs to have property profiles tailored to specific loading demands.

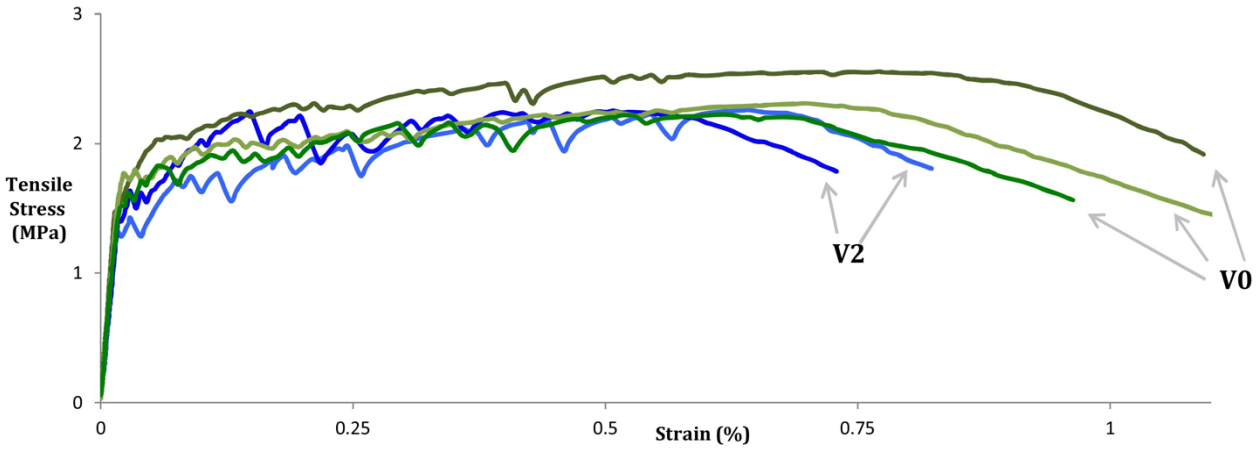

Figure 2.13: The V2 composition (blue) shows similar low strain performance to the V0 composition (green), but cannot match V0's strain capacity or distributed microcracking behavior

Observation of the curauá-SHCC failure surfaces suggests that the tensile strength of the curauá fiber may not be fully utilized in these composites, showing potential for further property profile enhancement. The fiber ends exposed when a V0 specimen was loaded beyond its strain capacity and to separation, seen in Figure 2.14, have appearance consistent with fibers that have been pulled out as opposed to ruptured; ruptured fiber ends would appear frayed and have shorter exposed lengths on a fracture surface.

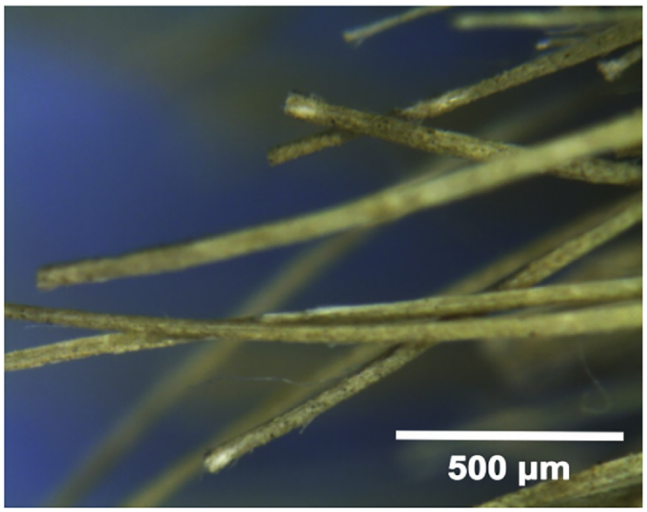

Figure 2.14: Exposed fiber ends on the fracture surface of a V0 composite specimen. The clean-cut ends and long exposed lengths indicate fiber pull-out as the mechanism of composite failure, rather than fiber rupture.

With fiber pullout being the dominating mechanism of composite failure, there appears to be potential for the fiber-matrix chemical and/or frictional bonding to $_{be}$ strengthened, while still achieving composite strain-hardening behavior. Figure 12.15 plots the current relationship between compressive strength and tensile strain capacity in curauá-SHCCs, as well as the potential performance vector that may be allowed by further enhancement of the strength of the interfacial bonding between the curauá fiber and the cementitious matrix.

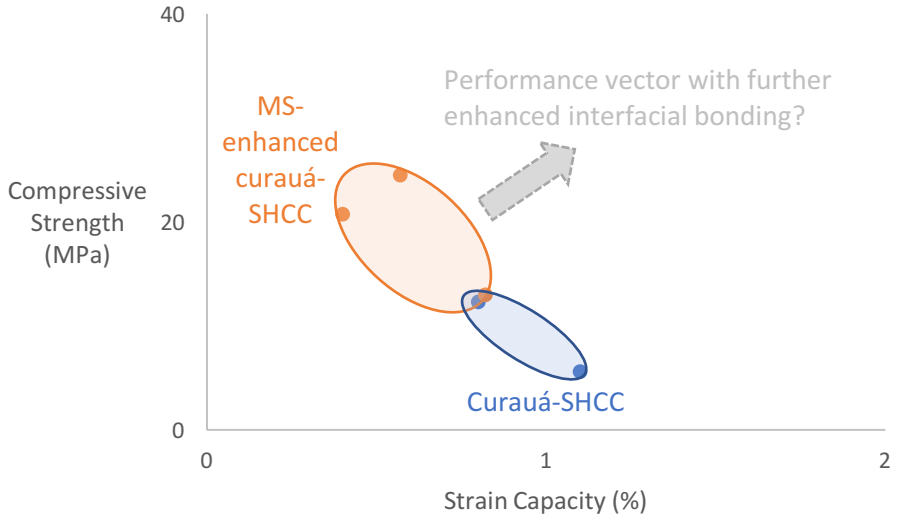

Figure 2.15: The relationship between compressive strength and tensile strain capacity of the curauá-SHCCs reported here and the potential performance vector that might accompany a further enhancement of the interfacial bond between the fiber and matrix

2.4.4 Curauá-SHCC thermal properties

To demonstrate the potential of curauá-SHCC for building cladding and façade application, the thermal conductivity, specific heat capacity, and thermal diffusivity of the V0 curauá-SHCC composition were measured. For comparison, those values of a typical ECC composition using synthetic polymer (PVA) fibers and fiber-less cement/fly ash mortar were also measured. This thermal testing was performed by collaborating student Alan Olvera and these results are illustrated graphically in Figure 2.16.

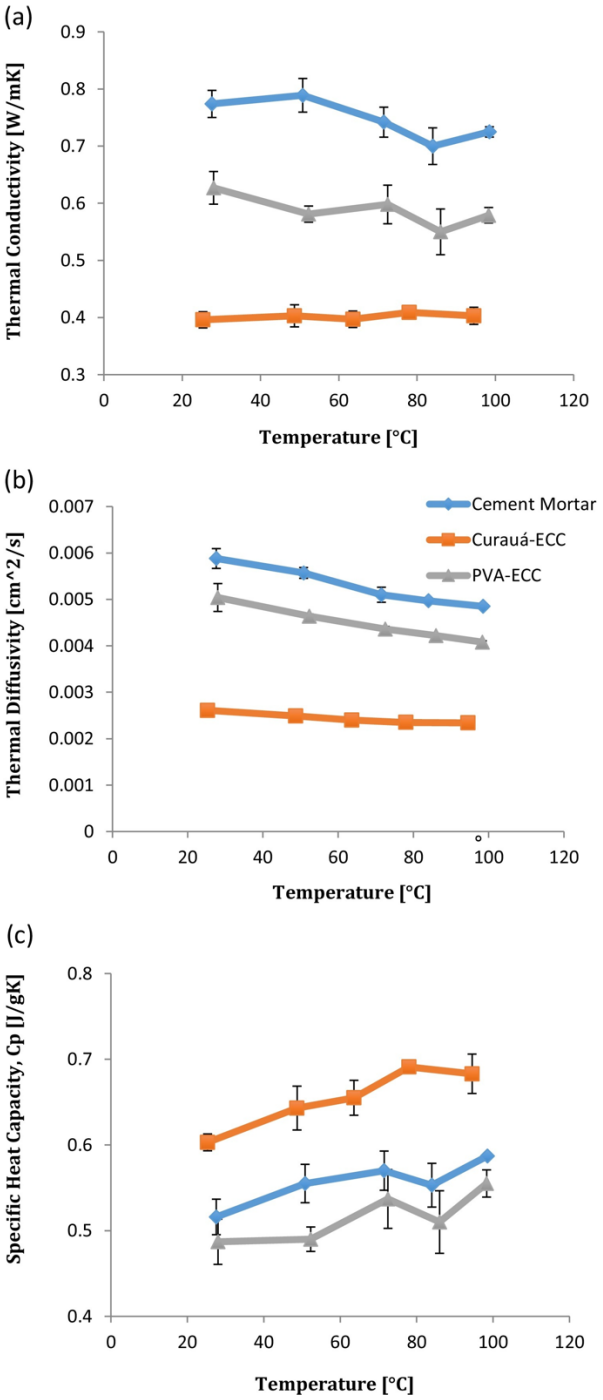

Figure 2.16: Characterization of (a) thermal conductivity, (b) thermal diffusivity, and (c) specific heat capacity for Curauá-ECC (labeled Curauá-ECC), compared to those values of cement/fly ash mortar and synthetic, PVA-fiber ECC. Curauá-SHCC exhibits lower thermal conductivity and higher thermal storage than PVA-ECC and fiber-less cement/fly ash mortar.

Table 2.6: Specific density values, as measured by helium pycnometry, for thermal diffusivity calculations

Material	Specific Density (g/cm^3)
Cement/Fly Ash Mortar	2.55
PVA-ECC	2.56
Curauá-SHCC	2.52

Specific density of each of these materials (required for the calculation of thermal diffusivity) is reported in Table 2.6.

It is seen that curauá-ECC offers both a lower thermal conductivity and lower thermal diffusivity, over the 20–100 °C temperature range, than fiber-less cement/fly ash mortar and typical, PVA-reinforced ECC. Further, the curauá-SHCC exhibits a higher specific heat capacity than either of the other materials. These rankings mean that, not only can curauá-SHCC effectively discourage the transfer of energy through itself better than these other materials, it can also store more energy—a thermal property profile well-suited for building cladding and facades.

2.4.5 Future development of curauá-SHCC

With fiber pullout being shown to be the dominating mode of composite failure in tension (Section 2.4.3), continuing to enhance the fiber-matrix bond appears to be the route to continued mechanical property improvement in curauá-SHCC. While continuing to increase the amount of the vinyl-silane coupling agent beyond 2.0% C.M. did not improve composite performance, additional fiber treatments or processing changes may be able to further enhance fiber-matrix bonding. One proposed route to improved fiber-matrix bonding is curing in a carbon dioxide-rich environment, a process sometimes referred to as “carbonation”. This procedure has been observed to reduce porosity in the ITZ of extruded natural fiber-reinforced cementitious composites [27]. It is suggested that this process be explored, as a means of improving composite mechanical performance, in the continued development of curauá-SHCC.

The thermal properties reported here are for curauá-SHCCs that were not optimized, or even explicitly designed, for thermal performance. The potential to improve upon the thermal properties for specific applications remains.

The research finding presented in Chapter IV of this dissertation may also provide hierarchical composite design routes to improve the mechanical property profile of natural fiber reinforced SHCCs such as those presented in this chapter. Rather than use a synthetic polymer fiber mesh material as investigated in Chapter IV, natural fiber mesh materials could be used to generate similar deformation mechanisms that function to boost mechanical properties of the composite.

Future work on the development of curauá-ECC should also explore the durability of such composites, in a variety of environments, over time.

2.5 CONCLUSIONS

An independent evaluation of the mechanical and physical properties of Brazilian curauá fiber has been conducted and the efficacy of chopped curauá fibers in castable, strain-hardening cementitious composites has been demonstrated. By reporting specific compositions and processing that promote distributed microcracking and strain-hardening behavior in curauá-ECC, the originally stated objectives of developing a "greener" version of ECC with the use of natural fibers, and establishing the basis of expanded utility of natural fibers for construction applications, have been accomplished. The effective use of curauá in ECC materials proves the feasibility of natural fibers in construction applications in general. Natural fibers can contribute to construction material greening and provide a route to low cost, but versatile construction materials, particularly for regions with local fiber availability. With the compressive strength of curauá-ECC reaching just over 20 MPa and tensile properties unable to match those of synthetic fiber ECCs, natural fiber cementitious composites in their current form are not structural building materials for universal use, but rather a low environmental and economic cost option for specific construction roles. The following conclusions can also be drawn from the results reported herein:

(1) Using a representative, bean-shaped cross section for curauá fiber strength calculations, the average strength of the white curauá fiber used in this study is measured as (620 ± 132) MPa.

(2) Physical characteristics of natural fibers (porosity, water absorption, fiber bundling, and a distribution of mechanical properties, etc.) present additional challenges in the design and processing of natural fiber composites, compared to composites using synthetic fibers.

(3) The use of vinyl-silane coupling agent provides sufficient fiber-matrix bonding in a cementitious matrix to allow robust composite strain-hardening performance.

(4) Distributed micro-cracking, strain-hardening cementitious composites can be made with discontinuous, natural curauá fibers as reinforcement, constituting a significant step toward versatile natural fiber composites for structural application, and representing a greening option for ECC materials.

(5) Microsilica can improve the compressive and tensile strength of curauá-reinforced ECC, while maintaining strain-hardening behavior, however, with a given set of fiber treatments and fiber-matrix coupling parameters, increasing composite strength will come at the sacrifice of tensile strain capacity.

(6) Based on evidence of fiber pullout being the dominating mode of tensile failure, methods of further enhancing fiber-matrix bonding may improve the mechanical performance of curauá-reinforced ECCs.

(7) The curauá-reinforced ECCs reported herein show potential for use as construction materials for cladding and façade applications given their lightweightedness and low thermal conductivity.

REFERENCES
(Chapter II)

[1] Li, V.C., "On Engineered Cementitious Composites (ECC) – A Review of the Material and its Applications," J. Advanced Concrete Technology, 1 (3) 215-230, 2003.

[2] Herbert, E.N. and V.C. Li, "Self-healing of engineered cementitious composites in the natural environment", High Performance Fiber Reinforced Cement Composites 6, G.J. Parra-Montesinos, H.W. Reinhardt and A.E. Naaman (eds.), Springer, pp.155-162, 2012.

[3] Ranade, R. , V.C. Li, M.D. Stults, W.F. Heard, and T.S. Rushing, Composite Properties of High-Strength, High-Ductility Concrete, ACI Mater. J., Vol. 110, Issue 4, pp. 413-422, 2013.

[4] Chandler, R.F. "Life-Cycle Cost Model for Evaluating the Sustainability of Bridge Decks: A Comparison of Conventional Concrete Joints and Engineered Cementitious Composite Link Slabs." A report of the Center of Sustainable Systems, University of Michigan, 2004.

[5] Li, V.C., "From Micromechanics to Structural Engineering – the Design of Cementitious Composites for Civil Engineering Applications," JSCE J. of Struc. Mechanics and Earthquake Engineering, 10 (2) 37-48, 1993.

[6] Kanda, T. and V.C. Li, "Practical Design Guidelines for Pseudo Strain Hardening Cementitious Composites Reinforced with Short Random Fibers – Part I Micromechanics theory for predicting first crack strength," AIJ J. Struct. Constr. Eng., 539, 13-21, 2001.

[7] Rokugo, K., T. Kanda, H. Yokota, N. Sakata, "Applications and recommendations of high performance fiber reinforced cement composites with multiple fine cracking (HPFRCC) in Japan," Materials and Structures 42:1197–1208, 2009.

[8] Li, V.C., S. Wang, and C. Wu, “Tensile Strain-Hardening Behavior of PVA-ECC,” ACI Materials J., 98 (6) 483-492, 2001.

[9] Maalej, M., and V.C. Li, "Introduction of Strain Hardening Engineered Cementitious Composites in the Design of Reinforced Concrete Flexural Members for Improved Durability," ACI Structural J., 92 (2) 167-176, 1995.

[10] Felekoğlu, B., K. Tosun-Felekoğlu, R. Ranade, Q. Zhang, and V.C. Li, “Influence of Matrix Flowability, Fiber Mixing Procedure, and Curing Conditions on the Mechanical Performance of HTPP-ECC,” J. Composites, Part B: Engineering, 60, 359-370, 2014.

[11] Yang, E.H. and V.C. Li, “Strain-hardening Fiber Cement Optimization and Component Tailoring by means of a Micromechanical Model,” J. Construction and Building Materials, 24, 130-139, 2010.

[12] Castro, D.O., Ruvolo-Filho, A., Frollini, E., Materials prepared from biopolyethylene and curauá fibers: Composites from biomass, Polymer Testing, Vol. 31, Iss. 7, pp. 880-888, October, 2012.

[13] Horlle de Oliveira, F., Luiza Helfer, A., Campos Amico, S., Mechanical behavior of unidirectional curauá fiber and glass fiber composites, Macromolecular Symposia, 319, pp. 83-92, 2012.

[14] Gomes, A., Matsuo, T., Goda, K., Ohgi, J., Development and effect of alkali treatment on tensile properties of curauá fiber green composites, Composites Part A: Applied Science and Manufacturing, Vol. 38, Iss. 8, pp. 1811-1820, 2007.

[15] Mano, B., Araujo, J.R., Spinace, M.A.S., De Paoli, M.-A., Polyolefin composites with curauá fibres: Effect of the processing conditions on mechanical properties, morphology and fibres dimensions, Composites Science and Technology, Vol. 70, Iss. 1, pp. 29-35, January 2010.

[16] Zah, R., Hischier, R., Leao, A.L., Braun, I., Curauá fibers in the automotive industry—a sustainability assessment, Journal of Cleaner Production, 15, pp. 1032-1040, 2007.

[17] Silva, R.V. and Aquino, E.M.F., Curauá Fiber: A new alternative to polymer composites, Journal of Reinforced Plastics and Composites, Vol. 27, no. 1, pp. 103-112, 2008.

[18] Satyanarayana, K.G., J.L. Guimarães, F. Wypych. Studies on lignocellulosic fibers of Brazil. Part I: Source, production, morphology, properties and applications. Composites: Part A 38 (2007) 1694–1709.

[19] Tomczak, F., K.G. Satyanarayana, T.H. Demetrio Sydenstricker. Studies on lignocellulosic fibers of Brazil. Part III: Morphology and properties of Brazilian curauá fibers. Composites: Part A 38 (2007) 2227–2236.

[20] Leão, A.L., R. Rowell, N. Tavares, Applications of natural fibers in automotive industry in Brazil, P.N. Prasad, J.E. Mark, S.H. Kandil, Z.H. Kaifi (Eds.), Science and technology of polymer and advanced materials, Plenum Press, New York, pp. 755–761, 1998.

[21] Barra, B.N. B. Paulo, C. Alves Jr., H. Savastano Jr., and K. Ghavami, "Effects of Methane Cold Plasma in Sisal Fibers", Key Engineering Materials Vol. 517 pp. 458-468, 2012.

[22] Dixit, S. and P. Verma, "The effect of surface modification on the water absorption behavior of coir fibers", Advances in Applied Science Research, 3 (3), pp. 1463-1465, 2012.

[23] Dai, D. and M. Fan, "Wood fibres as reinforcements in natural fibre composites: structure, properties, processing and applications," Natural Fibre Composites: Materials, Processes, and Applications, pp. 3-65, Woodhead publishing, 2014.

[24] Ranade, R., Doctorate Dissertation, University of Michigan, 2014.

[25] Soltan, D.G., P. das Neves, A. Olvera, H. Savastano Jr., and V.C. Li, Introducing a curauá fiber reinforced cement-based composite with strain-hardening behavior, Journal of Industrial Crops and Products, Vol. 103, Pages 1-12, September 2017.

[26] Barra, B.N., Doctorate Thesis, University Sao Paulo, 2014. (In Portuguese)

[27] Santos, S.F., R. Schmidt, A.E.F.S. Almeida, G.H.D. Tonoli, H. Savastano Jr., Supercritical carbonation treatment on extruded fibre-cement reinforced with vegetable fibers, Cement and Concrete Composites, 56, pp. 84-94, 2015.

[28] Cordeiro et al., Sustainable cultivation and production of curauá (Ananas comosus var. erectifolius (L.B.Sm) Coppens & F.Leal, Bromeliaceae) in the northeast of Para, Brazil. Proceedings: Non-wood Forest Products – Meeting on Non-wood Forest Products and Environmental Services. Esquel, Chubut province, Argentina, 2010. (in Portuguese)

CHAPTER III

Design and development of self-reinforced cementitious materials for building-scale 3D printing

3.1 INTRODUCTION

The modern construction industry has recently seen a push toward increased automation, led by recent advances in building-scale additive manufacturing processes [1-6]. The potential benefits of automated additive manufacturing processes for the construction industry have been previously enumerated and include improved efficiency and safety [5,7-10].

Three-dimensional printing ("3D printing" or "3DP") of concrete has generated significant publicity and is the most widely recognized and applied method of additive manufacturing for construction applications. Many of the recent innovations in the area, in both academic and commercial research and development, have focused primarily on the equipment with which 3D concrete printing is conducted to improve the capabilities of the process.

Much less attention has been paid to the materials used for building-scale 3D printing, though this has also been studied [11-13]. While many engineering challenges related to the "printability" of the concrete materials used for building-scale 3DP have been overcome, much of this work ignores the inherent weaknesses of traditional concrete and the implications of these weaknesses for 3D printed structures.

Traditional concrete is brittle and weak in tension, prone to failure in many common loading situations such as those that introduce bending moments or shear forces. For this reason, steel reinforcement is typically used to carry tension within concrete, and printed concrete is no exception. Steel reinforcement is susceptible to corrosion, which introduces additional tensile

forces on the concrete cover and often leads to rapid deterioration of concrete structures. Additionally, the placement of steel reinforcement into a 3D printed structure is antithetical to the speed, ease, and design freedom promised by the freeform, bottom-up 3DP paradigm. The need for placement of additional reinforcement in large 3D printed structures has limited the benefits, short of its potential, that the process has been able offer the industry.

In this study, a self-reinforced printable cementitious composite, designed to reduce or eliminate the need for steel reinforcement in printed structures and based on the micromechanical design considerations of SHCCs, is introduced. A general design philosophy for printable cementitious materials, leveraging thixotropy, is described. Compositional ingredients and material processing parameters are investigated for their contribution to material behaviors that promote printability in cementitious materials.

3.1.1 Printability

The material behaviors that define printability, the capacity for a material to be successfully processed via the 3DP process, have been previously described for cementitious materials [1,10,11]. Lim et al. (2012) stated, "the wet properties of the [cementitious] material are critical to the success of manufacture", and go on to identify the key attributes of printability [1]. These attributes are (1) extrudability, the capacity of the cementitious material in the fresh (uncured) state to pass or be pumped through small pipes/nozzles and ultimately be deposited in an even, continuous filament, (2) buildability, the ability of a printed filament to hold its shape, particularly under the weight of subsequently printed layers, and (3) interlayer bonding, the ability of adjacent filaments to form a cohesive bond, producing a unified, structurally sound printed part. Each of these parameters is dependent on "workability", a descriptor of the rheological properties of a freshly mixed cementitious material. Workability can be equated to "flowability", an often-used metric to indirectly, but quantitatively, evaluate the rheology of freshly mixed cementitious materials. "Open time" is defined as the period of time in which the workability is consistent within certain tolerance acceptable for 3DP.

Extrudability and buildability are competing factors in that high workability promotes extrudability, while low workability promotes buildability. Additionally, low workability can

negatively affect interlayer bonding. These three key attributes—extrudability, buildability, and interlayer bonding—must be properly balanced to allow printability.

3.1.2 Thixotropy and minimal workability loss for printability

The ideal behavior of a "printable" cementitious material as described above is summarized in terms of flowability over time, or "flowability evolution", in Figure 3.1. Flowability, a standard metric used in concrete materials design and evaluation, is an efficient indicator of workability. Between the time the material is thoroughly and completely mixed, t=0, and the time the material is printed, $t=T_p$, the material should be "extrudable" which corresponds to a large range of flowability values above a certain critical value. At the time the material is deposited by the printer head, the material needs to be both extrudable and immediately buildable, corresponding to another range of flowability values below that certain critical value. The material needs to first hold its shape when extruded in a predictable way, and by the time subsequent layers are deposited upon it, be able to support those respective weights without excessive deformation. The loss of flowability prior to deposition could theoretically take place at any rate, represented by the various dotted lines in Fig. 3.1, as long as deposition occurs when the material is both extrudable and buildable. Summarized simply, the ideal material should be flowable prior to deposition, be both extrudable and buildable at the time of deposition, and rapidly harden after deposition.

Because the time from mixing to being deposited (due to the batch processing typically used for cementitious material) would not realistically be constant for a large-scale print, the time at which the material rapidly hardens needs to be decoupled from the time the material is mixed, or more precisely, the time from which the material is hydrated. A graphical representation of this theoretical "printable" behavior, subject to the constraints of construction and cementitious material processing, is presented in Figure 3.2.

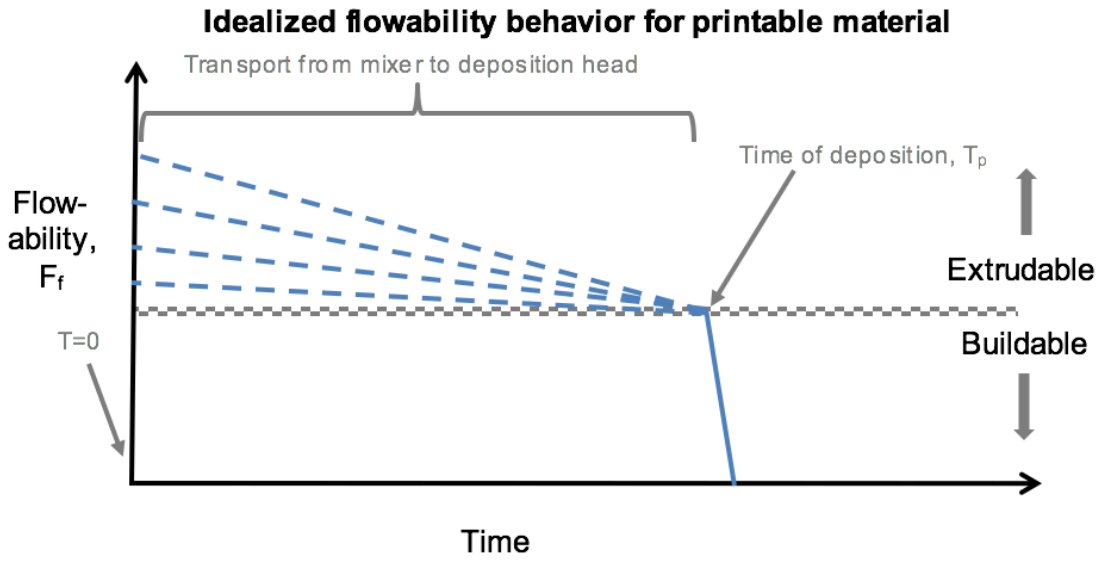

Figure 3.1: The idealized flowability behavior for a cementitious printable material is graphically represented in terms of flowability evolution, wherein the material is extrudable prior to deposition, extrudable and buildable at the time of deposition, and rapidly hardening after deposition so as to become increasingly buildable

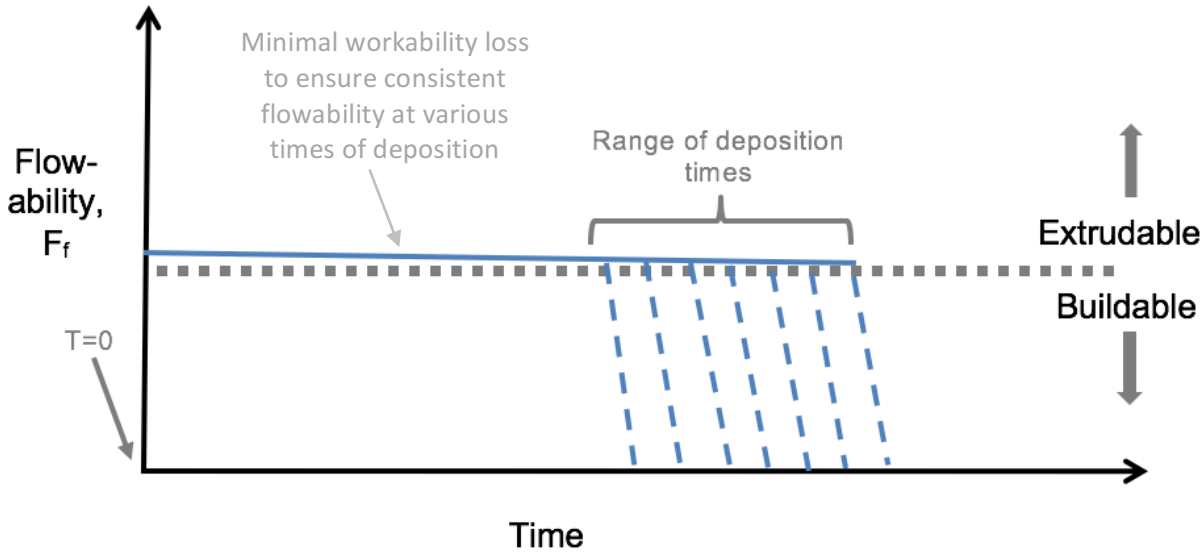

Figure 3.2: The theoretical flowability evolution required for consistent 3D printing, given common practical constraints of construction and cementitious material processing. The low negative slope of the flowability evolution curve prior to the various times of deposition represents a minimal amount of workability loss between mixing and deposition that would give a predictable, consistent deposition flow rate and filament stability.

As Figure 3.2 indicates, there should be minimal workability loss (corresponding to change in flowability, ΔF_f) between the start of deposition to end of deposition, to ensure consistent deposition. In practice, minimal workability loss during deposition can be extrapolated to also require a low decrease in flowability between the end of mixing to the end of deposition. This "harden on command" flowability evolution is atypical and challenging for typical cementitious materials.

Thixotropic rheological behavior can theoretically be exploited to generate this flowability evolution behavior in which hardening is decoupled, at least temporarily, from time after mixing [14]. Thixotropic materials can be described as having a reduced viscosity (i.e. increased flowability) when a shear stress, such as mixing/stirring, is applied, compared to the unperturbed state. Viscosity is regained in a thixotropic material when the applied shear stress is removed, in a process called rebuilding. In a 3D concrete printing system, shear stresses are applied in the pumping process. Additional agitation can be performed as needed in the material feeding system. A cementitious material that is thixotropic with rapid rebuilding, as illustrated graphically in Figure 3.3, could therefore be highly printable.

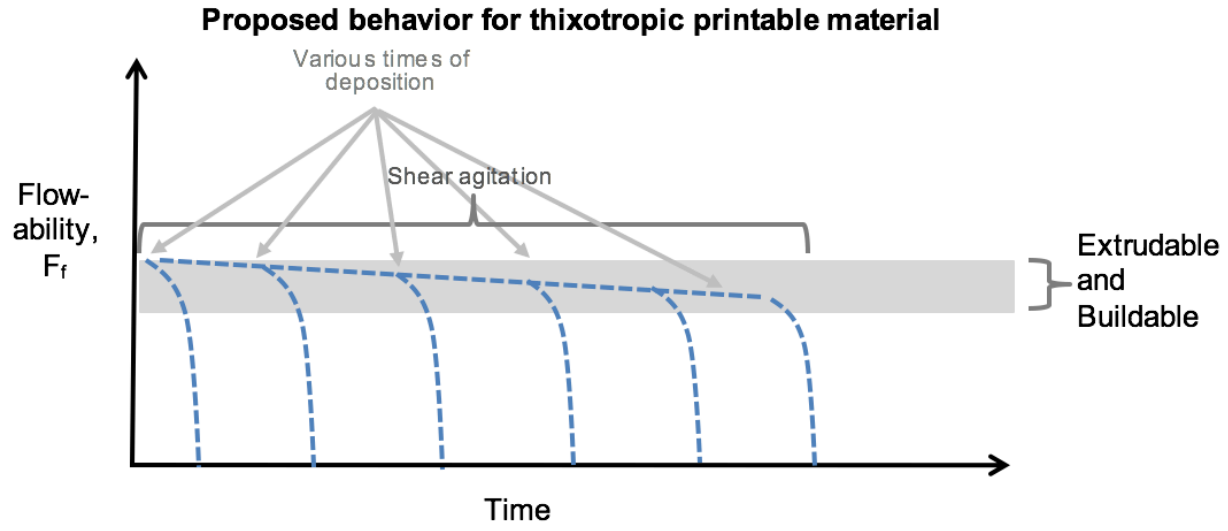

Figure 3.3: Proposed flowability evolution for a realistically printable cementitious material derived via thixotropy and rapid rebuilding

A range of flowability values in which the material is both extrudable and buildable, as indicated in Figure 3.3, would also be advantageous. Thixotropy would allow a range of flowabilities in which the material is simultaneously extrudable when a shear stress is applied, and buildable when that shear stress is removed.

To guide the design of printable cementitious materials, this study investigates the effect of several compositional ingredients reported to promote thixotropic behavior in mixtures, in addition to relevant processing parameters, on the attributes associated with printability of cementitious composites. Thixotropic behavior with minimal workability loss and rapid rebuilding is targeted, in combination with mechanical behaviors that promote durability in cementitious materials.

3.1.3 ECCs as durable materials for building-scale 3D printing

Engineered cementitious composites (ECCs), a family of cementitious materials compatible with typical concrete processing methods and exhibiting strain-hardening behavior by way of a low volume fraction amount of dispersed polymer fibers, have been developed for the purpose of improving the durability and resiliency of critical structural and infrastructural components. The micromechanics of ECCs, also called strain-hardening cementitious composites (SHCCs), have been previously described, and differ from those of other fiber reinforced concretes [15]. In short, when the brittle cementitious matrix fractures in tension, the dispersed fibers are able to bridge the crack, holding the crack to several tens of microns in width, while carrying the tensile load such that further opening of the microcrack requires more energy than originating a microcrack elsewhere in the matrix. This cycle can be repeated many times, such that the composite is able to distribute deformation throughout and suppress brittle fracture failure. ECCs are more damage and flaw tolerant than other fiber-reinforced materials because strain-hardening behavior, rather than strain-softening behavior, is generated. In fact, ECCs exhibit tensile ductility (as measured by strain capacity prior to failure, where failure is defined as the inability to carry and increasing load) and toughness (energy required to cause failure) hundreds of times those values of traditional concretes, providing the potential to eliminate or diminish the amount of steel reinforcement necessary to accommodate tensile loading.

Engineered cementitious composite materials have been previously developed for the casting application method typical of concretes [16], as well as the spraying method typical of "shotcretes" [17,18]. In this study, a material exhibiting the characteristic strain-hardening behavior of ECCs is designed to have the distinct rheological properties required for functional compatibility with building-scale 3D printing processes (i.e. printability).

While fiber reinforcement in printable cementitious materials has been studied in the past [11-13], the fibers in those cases are generally included to mitigate the effects of drying shrinkage and do not promote robust tensile strain hardening behavior, which is responsible for the load-carrying capacity and durability of ECCs, in the printable material.

3.2 MATERIALS AND METHODS

3.2.1 Evaluation of fresh state properties

Fresh state workability has been identified as being crucial to the printability of cementitious materials. In this study, the fresh state is defined as the condition of the complete composite composition (including dispersed fibers) in the short time period after complete mixing has been concluded, and in which printing would theoretically take place. In this work, workability is quantitatively assessed using the flowability factor, measured via the drop table test (ASTM C1437 and ASTM C230), as used previously for investigations of thixotropic [19] and printable [10] cementitious materials. In the present study, the flowability factor of cementitious pastes (completely mixed compositions, including fibers) is measured over time (after mixing is stopped) to generate a "flowability evolution" curve, providing a convenient method of describing the change in workability (stiffening) over time intervals relevant to 3D printing. The simplicity of this method of assessing workability over time allows it to be used (1) to accelerate the design process of new printable mixes and (2) as a realistic, on-site quality control technique.

3.2.2 Compositional ingredients

The material compositions investigated in this study are inspired by previously reported engineered cementitious composites. Several compositional ingredients, listed in Table 3.1, are

included due to their reported effects on the fresh state and early stage properties, hypothesized to promote target behaviors for printable cementitious materials.

Table 3.1: Ingredients investigated for utility in printable cementitious compositions

Ingredient	Reported Effects in Cementitious Pastes
Calcium Aluminate Cement (CA)	*Early flowability followed by rapid hardening, high early strength [10][17]*
Hydroxypropyl Methylcellulose (HPMC)	*Increased viscosity, segregation prevention during pumping, and thixotropy [17][21]*
Microsilica (MS) and ground silica flour	*Early strength and thixotropy [22][23]*
Attapulgite Nanoclay (ANC)	*Thixotropy and enhanced cohesion [19][24][25]*

Composition is used as variable throughout the study and compositional variations in the reported results are labeled accordingly. Several important mix compositions reported herein are described and labeled in Table 3.2. All compositional components are reported in percentage, by weight, of the total cementitious material. In this study, "total cementitious material" is defined as (Type I cement + Fly Ash + calcium aluminate cement) by weight. All mixes contain 2% by volume polyvinylalcohol (PVA) fiber cut to 12 mm, the typical fiber volume fraction for ECC materials. Fiber is included in all the mixes for all tests due to its significant effect on properties in both the fresh and cured states.

Table 3.2: Several key mix compositions are described. All compositions are reported in percentage of total cementitious material (%C.M.), apart from fiber content which is reported in volume fraction.

	Type I Portland Cement	Class F Fly Ash	Calcium Aluminate Cement	F-75 Silica Sand	MS	GS	Water	ANC	HPMC	HRWRA	PVA Fiber (% by vol.)
Mix 0	45.5	54.5	0.0	36.3	0.0	0.0	26.4	0.0	0.0	0.3	2.0
Mix 1	76.9	23.1	0.0	61.5	0.0	0.0	35.4	0.0	0.4	0.6	2.0
Mix 2	76.9	23.1	0.0	61.5	0.0	0.0	38.0	0.0	0.4	0.8	2.0
Mix 3	69.6	22.4	8.0	60.0	0.0	0.0	37.2	0.0	0.4	0.8	2.0
Mix 4	69.6	22.4	8.0	45.0	10.0	5.0	43.0	0.0	0.4	0.8	2.0
Mix 5	72.0	23.0	5.0	45.0	10.0	5.0	43.0	0.5	0.4	0.8	2.0

MS: microsilica **GS:** ground silica
ANC: attapulgite nanoclay **HPMC:** hydroxypropylmethylcellulose
HRWRA: high range water reducing agent **PVA:** polyvinylalcohol fiber (12mm)

Additional information about each of the compositional ingredients can be found in Appendix III.1.

3.2.3 Mix processing

Mixing of the cementitious compositions is conducted in KitchenAid (6 qt.) or Hobart (12 gal.) planetary-style mixers. Because the mixing process, including the order of ingredient addition and time of addition, affect the fresh properties of the cementitious paste, this procedure was conducted according to an explicit schedule. Dry ingredients (excluding ANC, HPMC, and MS) are mixed first for at least five minutes. A portion of the water content is added at time zero, followed by the high range water reducing agent (HRWRA) at t = 30 seconds, and the MS content between t= 1:00 min and t=2:00 min.

Remaining portion of the water content is mixed with the ANC and used for the ANC exfoliation process, similar to that described in Kawashima (2013), in a standard 40 oz./700 W blender [24,25]. The portion of the water content separated out for this process is ~0.7-1.0 L., depending on the batch size, sufficient to cover the blender blades and for rinsing of the blender jar to ensure nearly all of the exfoliated ANC content is added to the mix. The ANC is exfoliated in water (blended) for at least 3 min. before being added to the mix. The ANC content, and associated water content, is added to the mix at t = 6 min. For mixes not including ANC, the entirety of the water content is added at time zero.

Half the HPMC content is added at t = 8 min, followed by the addition of fibers in small handfuls between t = 9 min and t = 12 min, after which the remainder of the HPMC content is added. Mixing continues until t = 28 to ensure even dispersion and activation of the viscosity modifying ingredients.

In addition to compositional ingredients, several processing parameters were investigated for their effect on fresh state properties. Water temperature and batch size, two controllable processing parameters, were used as variables. The water content for each mix reported herein, unless otherwise stated, can be assumed to be 20-25°C at time of addition. Three typical batch

sizes are used in this study: 1.2 L, 3.1 L, and 6.2 L, which will hereafter be referred to as small, medium, and large batches.

3.2.4 Workability loss evaluation method

For the investigation of workability loss, half of the mix volume is removed from the mixer at t = 28 min, and drop table flowability testing is performed at regular time intervals. The other half of the mix volume remains in the mixer and continues to be mixed for an additional 15 min and is removed at t = 43 min, at which time flowability testing is performed. Comparison of the flowability evolution between these two volumes of the same mix determines the workability loss with continued agitation. Minimal workability loss is targeted for robust printability.

While thixotropy is not directly measured via hysteresis in this study, workability loss is used as an indicator of "single cycle" thixotropy over the short time scale in which a cementitious material would be printed.

3.2.5 Printability evaluation methods

A manual extrusion technique was used as a preliminary, small-scale approximation of the final step of typical 3D printing processes designed for concrete. This printing approximation technique used a mechanically actuated caulk gun, pictured in Figure 3.4, with circular nozzle diameters 8mm – 13 mm. In lieu of a progressive cavity pump, a peristaltic pump with a 3 cm tube diameter and 4 cm x 1.5 cm flat tip nozzle was used for a large scale approximation. Manual agitation of the material in the hopper of the peristaltic pump was performed to maintain adequate workability over the period of printing.

Figure 3.4: A mechanically actuated, manually operated caulk-gun apparatus, shown with a pencil for scale, was used as a means of extrusion for a small-scale approximation of the final step of the 3D printing process. Nozzle diameters 8-13mm were used.

3.2.6 Mechanical performance evaluation methods

Uniaxial tensile and compression testing was used to evaluate mechanical performance of the materials. Tensile specimens were prepared via casting using dogbone [26] and coupon conformations, as well as via the manual printing approximation technique in the coupon shape. Both casting and the manual printing approximation technique were used to produce cubic specimens for compression testing. All test specimens were cured in air at room temperature as would be realistic for printed forms in practice. Mechanical testing on the composites was performed 28 days after being mixed and formed.

Tensile testing was performed with a universal tensile testing machine (Instron), with constant displacement loading at a rate of 0.005 mm/s, based on the recommendations of the JSCE [26]. Ultimate tensile strength is reported herein as the stress at the maximum load sustained by each composite. Strain capacity is reported as the strain at maximum stress carried by the composite prior to terminal stress decay.

Compression testing was performed with a Forney compression machine. A stress controlled loading rate of ~50 psi/s (~344.7 kPa/s or 890 N/s) was used, based on recommendations of the ASTM C109 International standard. Compressive strength is reported as the stress at the maximum load sustained by the composite.

3.3 RESULTS AND DISCUSSION

The flowability evolution of typical ECCs (represented by Mix 0), designed for casting, is not appropriate for 3DP due to high initial flowability and the long time required for the material to harden, as illustrated in Figure 3.5. For comparison, Mix 1 is also plotted in Figure 3.5. In Mix 1, HPMC was used as a thickening agent to create a mix that exhibited flowability values that allowed extrudability and the ability of the extruded filament to hold its shape. Preliminary testing, using the manual extrusion approximation technique, showed that flowability factor values between 1.2 and 1.4 were an appropriate target for extrudability and shape stability under self-weight, however rapid hardening is also required for buildability. Mix 1 shows that manipulation of viscosity via HPMC and cement/fly ash ratio is successful in modifying the flowablity factor to fall within this range. However, a practical printable cementitious material is not achieved due its slow rate of hardening. Rapid hardening (after extrusion) is desired to

accommodate the weight of many subsequently deposited layers and to facilitate time-efficient construction.

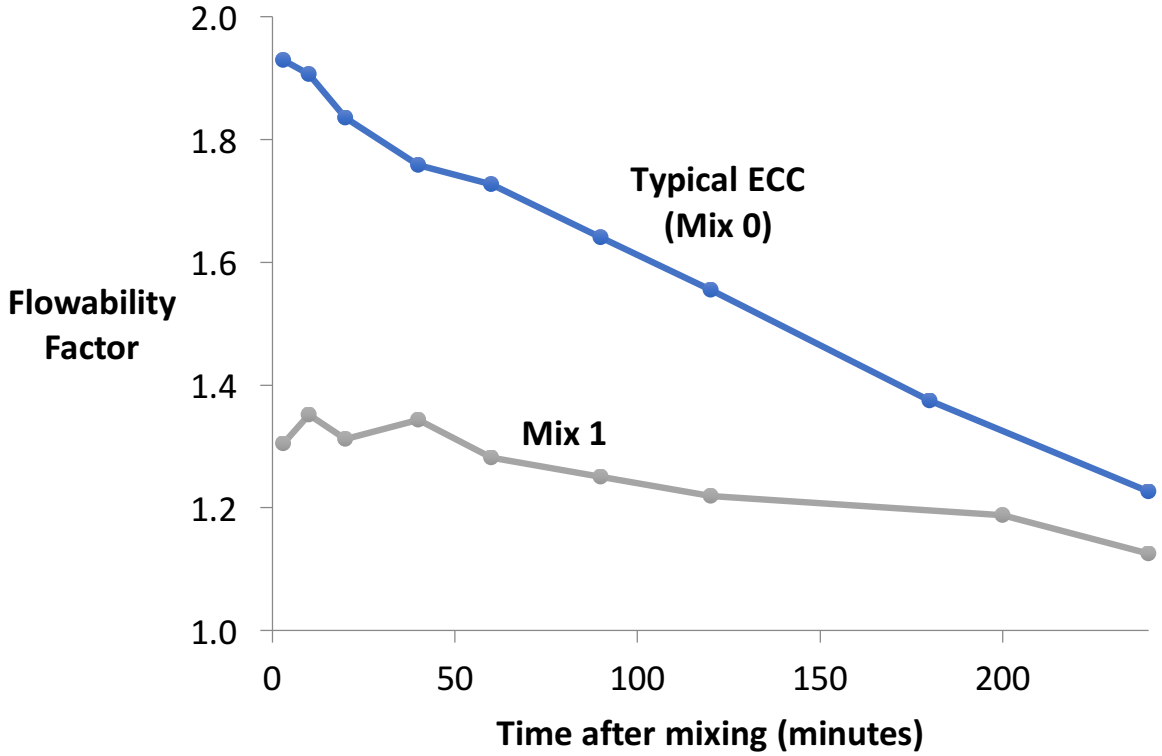

Figure 3.5: The flowability evolutions for a typical castable ECC (Mix 0) and a viscosity-modified version (Mix 1) incorporating HPMC. Neither flowability evolution is appropriate for 3D printing due to the long hardening times.

3.3.1 Compositional Effects on Workability Evolution

Calcium aluminate cement, microsilica, ground silica, and attapulgite nanoclay are all investigated for their effect on workability, as indicated by flowability evolution. The flowability evolution generated by various dosages of each of these compositional ingredients are measured and reported here to guide composite design in a systematic and broadly applicable manner. The trends in flowability evolution behavior are more important to note than absolute flowability values because these ingredients produce additive effects on initial flowability, rate of hardening, and time to hardening, and not all permutations of ingredient dosage combinations are measured/reported here. Two of the most promising compositions, based on flowability

evolution and incorporating a combination of these ingredients, are described and labeled in Table 3.2 as Mix 4 and Mix 5.

Calcium Aluminate Cement

Calcium aluminate cement (CA) was seen to be effective primarily in manipulating the rate of hardening. Mix 2 was used a baseline to illustrate the effect of CA dosage on the rate of hardening. Water content was adjusted slightly to allow sufficient mixing and fiber dispersion for several dosages. The effect on flowability evolution of various dosages of CA, in the small batch size, is illustrated in Figure 3.6. The rapid hardening seen in CA/Portland cement mixes has been previously attributed to "the rapid formation of Ettringite and secondarily due to the hydration of CAC" [20].

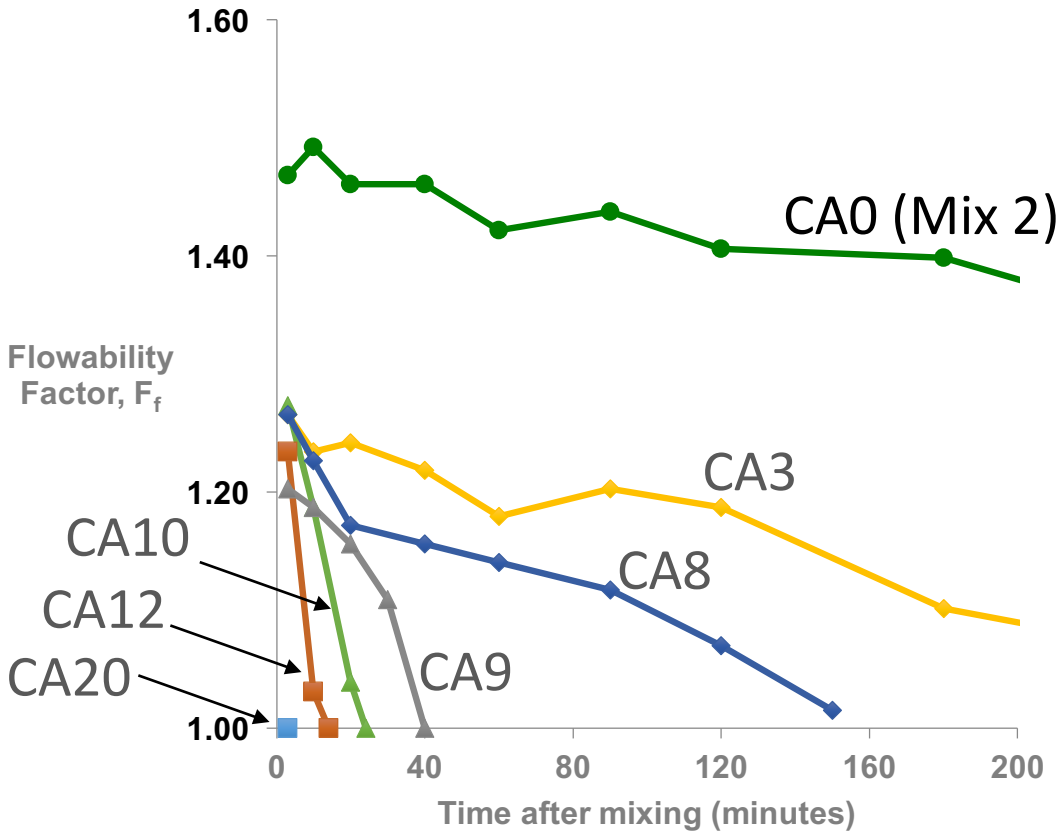

Figure 3.6: Effect of calcium aluminate dosage on the flowability evolution of the cementitious composite in the small batch size, where CA0, CA3, and CA8 et cetera, represent calcium aluminate cement content of 0, 3, and 8 et cetera percent by weight of total cementitious material, respectively.

The relatively rapid hardening rates exhibited by the CA9 and CA10 compositions here are desirable for printability, however rapid hardening is not the only requirement for printability; initial flowability adequate for extrudability and minimal workability loss under continued shear agitation are also targeted behaviors for printability. Additional compositional ingredients and processing parameters that address initial flowability and workability loss, will also affect the rate of hardening, meaning that calcium aluminate dosages lower than 9% CM can also generate appropriately rapid hardening behavior in some SHCC compositions. In larger batch sizes, the rapid hardening rates seen in Figure 3.6 for CA9 and CA10 were achieved with lower CA dosages (5% CM Calcium Aluminate), with the addition of ANC and increased water temperature (Section 3.3.5). Compositional considerations regarding the mitigation of workability loss under continued agitation are addressed in Section 3.3.6.

Microsilica and Silica Flour

Microsilica, substituted for silica sand by weight, was seen to increase the rate of hardening (Figure 3.7), however significant increase in water content was required to produce proper dispersion of fiber, and effects of the increase in water dominated at the higher water contents. Though the higher water contents produced acceptable early flowability, they also produced longer time to hardening.

As seen in Fig. 3.7, introducing ground silica (GS), also called silica flour, in addition to MS was seen to allow both the early flowability and a rapid rate of hardening. This is likely due to a more even particle size distribution caused by the substitution of MS and GS for silica sand—the GS has an average particle size between those values of F-75 silica sand and MS. This promising composition incorporating both MS and GS is labeled Mix 4, attractive due to its rapid hardening and early flowability factor values corresponding to the 1.2-1.4 target for a combination of extrudability and buildability.

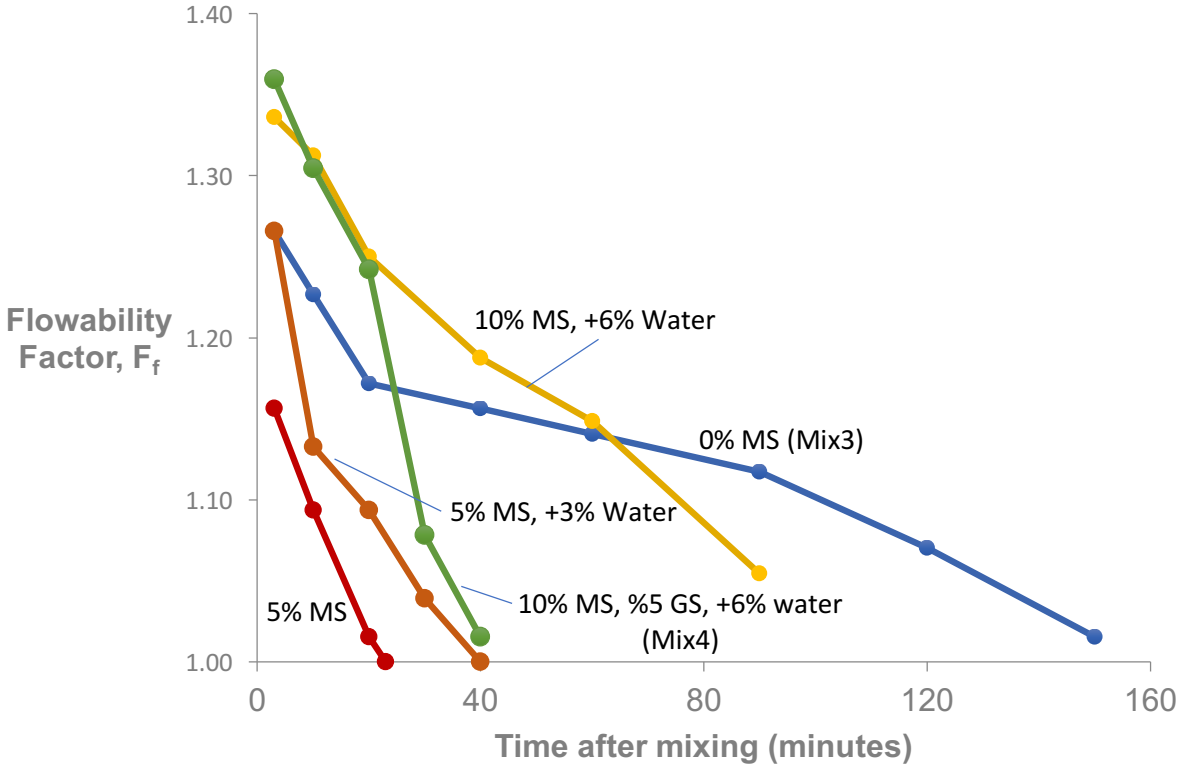

Figure 3.7: The effect of microsilica (MS) dosage on flowability evolution in the small batch size. These mix compositions are based on Mix 3 and inspired Mix 4.

Attapulgite Nanoclay

The effect on workability, as depicted by flowability evolution, of ANC dosages is illustrated in Figure 3.8. A thickening effect, reducing the flowability and time to hardening, is seen when mixed into large batch sizes. Rate of hardening ($\frac{\Delta F_f}{t}$) is only slightly increased.

An effect on the mitigation of workability loss, the primary motivation for its inclusion, was also observed at the 0.5% C.M. and 0.8% C.M. dosages of ANC, as discussed in Section 3.3.6.

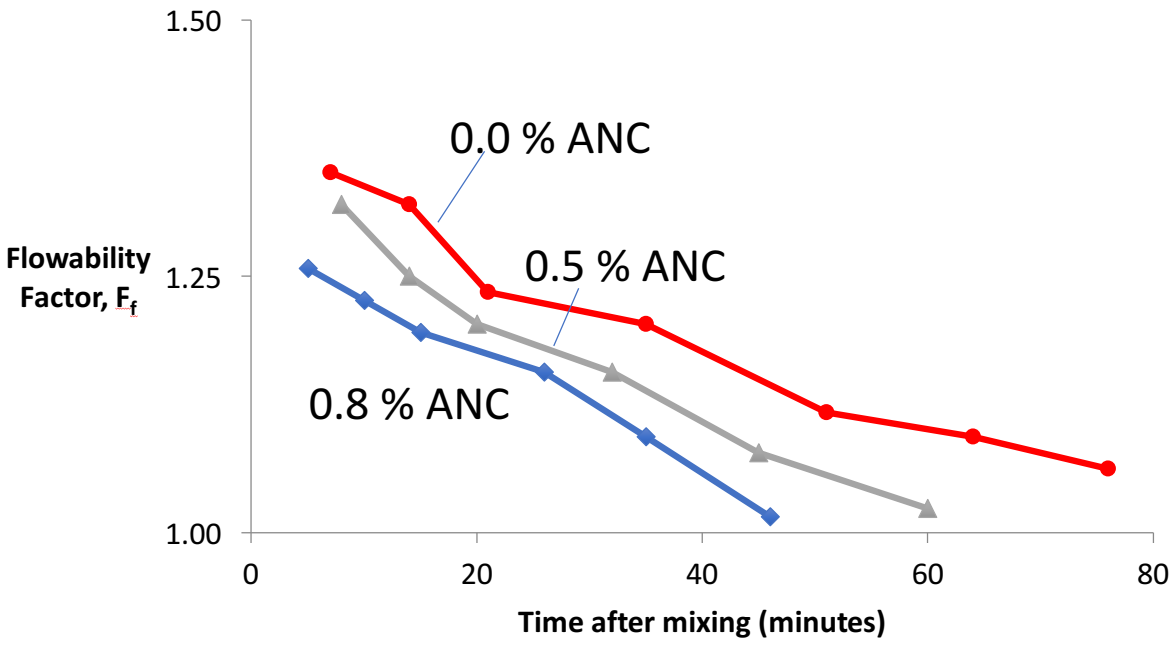

Figure 3.8: ANC is seen to reduce flowability and reduce the time to hardening

3.3.2 Water Temperature Effect on Workability Evolution

The Mix 4 composition was used to illustrate the effect of water temperature on workability in the fresh state, as seen in Figure 3.9. The flowability evolution curves for the three clustered, intermediate temperatures illustrate the degree of variability to be expected between different batches of the same composition. Most current concrete printing technology hardware should be able to handle a degree of material variation for practical application, but it is recommended that water temperature be carefully monitored and controlled for mixing of printable cementitious composites. Water temperature can also be used to intentionally manipulate the fresh state properties of a particular mix composition. Water temperature affects fresh state rheological properties due to the accelerated activation of pozzolonic reactions of the cementitious materials.

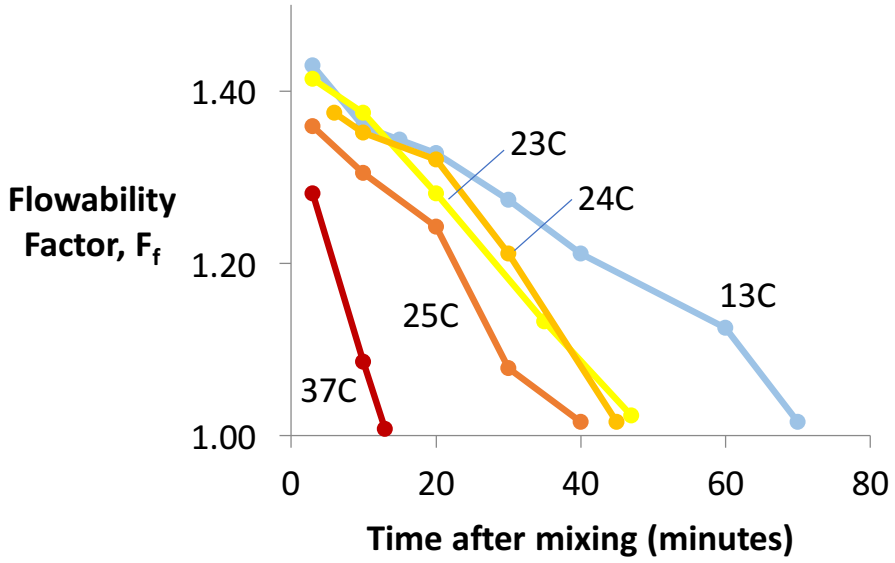

Figure 3.9: Effect of water temperature on flowability evolution in Mix 4 (small batch)

3.3.3 Mechanical Performance Characterization

Performance in Tension

Tensile performance of each composition was evaluated to confirm robust tensile strain hardening behavior. Mix 4 performed similarly to castable ECC compositions when each was tested in the cast form (Figure 3.10). Specimens were tested in the cast dogbone form to determine the inherent tensile properties of the material itself. This specimen type generally measures the material's ideal tensile performance due to the shape of the specimen which encourages fiber alignment and mitigation of stress concentrations and flaws.

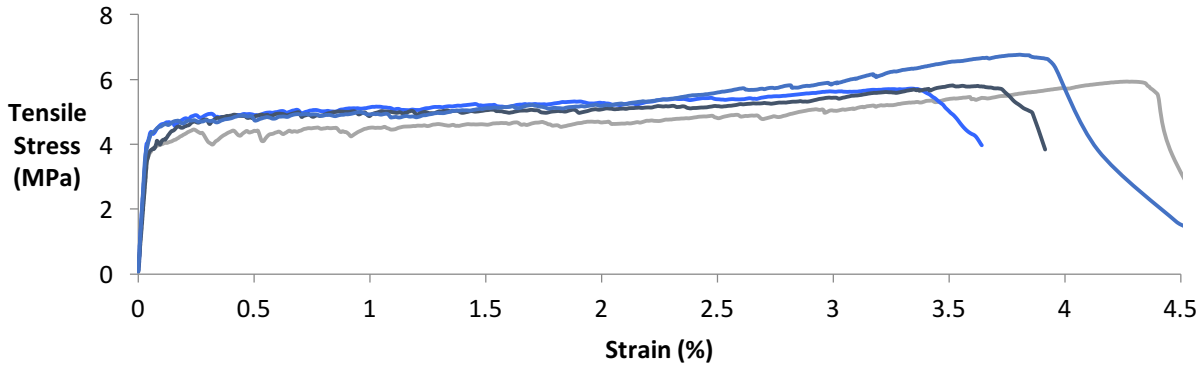

Figure 3.10: Stress-strain curves (blue) of specimens cast with Mix 4, tested under direct tension, are compared with a representative curve (gray) for a typical ECC material (Mix 1), using dogbone shaped specimens

To assess the tensile performance in the printed or "structured" state, specimens were prepared with Mix 4, using the manual extrusion approximation technique described in Section 3.2.5. This technique allowed specimens to be produced with aligned filaments in multiple layers (see Fig. 3.11), mimicking the structure of a printed form. This form includes imperfections, such as rough, ribbed surfaces, and the joints (and sometimes small gaps) between adjacent filaments. These specimens were "printed" in the rectangular shape of the coupon specimens often used to test cast cementitious materials in tension.

As seen in Figure 3.12, these "printed" coupon-shaped specimens were compared under direct tension with "cast" specimens (coupon form) of the same composition (Mix 4), to illustrate the effect on mechanical performance of the structuring that would result from the 3D printing process. The average ultimate tensile strength and strain capacity of the printed and cast specimens are compared in Figure 3.13. The superior performance in the printed form can be attributed to a much higher degree of fiber alignment in the tensile direction and the squeezing action produced upon extrusion, which may serve to eliminate air trapped in the material and densify the material as the filament form is produced.

The degree of fiber alignment is likely to be reduced as the filament size is increased for process scaling, but alignment is still expected to be generated based on the material flow/extrusion process. Deliberate nozzle design may be used to enhance fiber alignment even as the process is scaled. This control over fiber alignment (parallel to the 3DP toolpath) will provide for opportunities to (1) reinforce critical areas of structures vulnerable to failures in tension, (2) impart mesoscale material structuring for functional grading or deformation mode manipulation, and (3) optimize mechanical properties for a given structure or part.

Multiple curves for each type of specimen are included in Fig. 3.12 to illustrate the range in performance observed for each type of specimen. The variable performance of the printed specimens can likely be attributed to the inhomogeneity of flaw size produced by the printing process and/or pattern. Regarding the difference in mechanical behavior when compared to the tensile performance of the dogbone specimens: the coupon specimen form generally

approximates material performance in the bulk state, with minimal fiber alignment, such as how the material would be structured in a large-scale cast form.

Figure 3.11: “Printed” coupon specimens

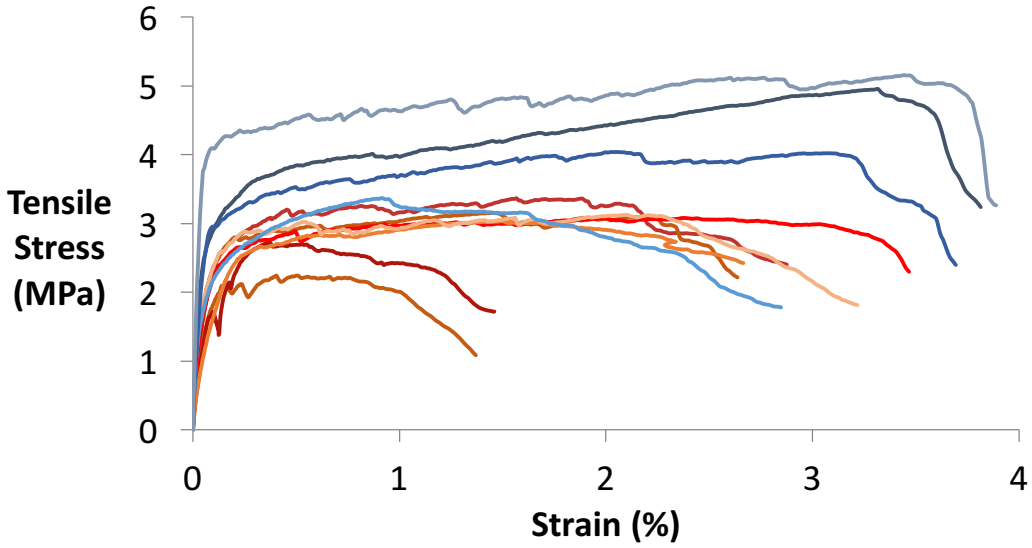

Figure 3.12: The printed specimens (blue curves), with highly aligned fiber orientation, outperform the cast specimens (red curves) composed of the same material, when compared using the coupon specimen shape

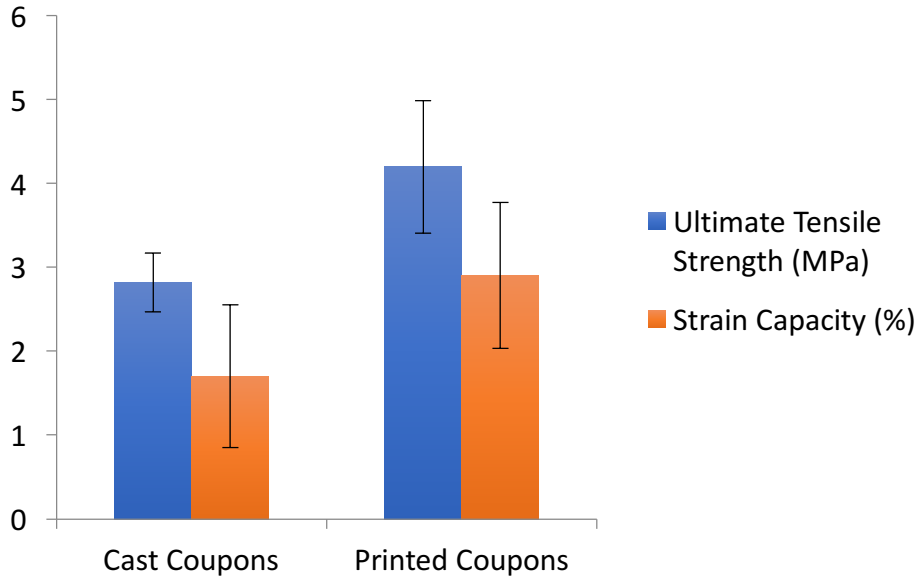

Figure 3.13: The effect on tensile strength and strain capacity of the printed structuring is illustrated with the Mix 4 composition

Performance in Compression

The effect on compressive strength of the printing process structure was also tested. Specimens printed in a cubic shape (with minimal intentional internal voids) were compared to specimens cast into the cubic shape. The results are compared in Figure 3.14. No significant difference in compressive strength was observed.

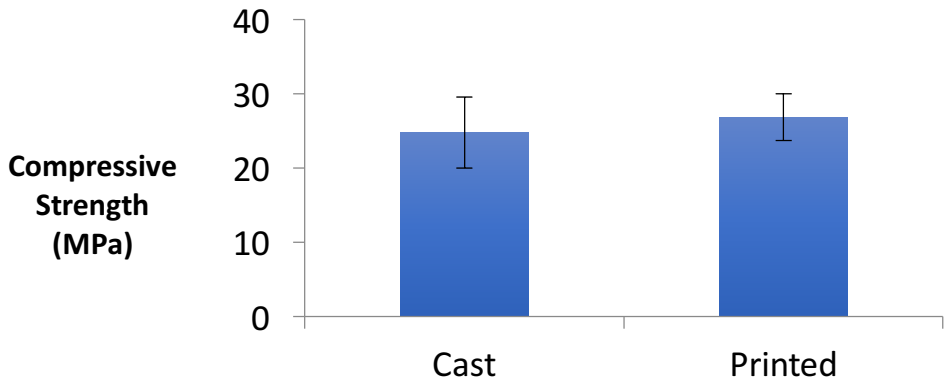

Figure 3.14: No significant difference was seen in compressive strength between structures produced by the casting and printing processes, using the Mix 4 composition

Early strength of a printable composition is important due to the significant amount of weight it is expected to support in the hours after being deposited, as the otherwise unsupported member or structure is constructed. The early strength of the Mix 5 composition, containing ANC, was measured using compressive testing of cast cube specimens to ascertain material properties of the composition (Fig. 3.15). This Mix 5 composition is shown to meet all other requirements of a printable cementitious composite (extrudability, buildability, rapid hardening, and robust tensile properties). These compressive strength values are not necessarily representative of any particular printed member formed with this composition due to flaws that could arise from the printing process, but rather an accurate representation of the inherent material properties of the composition. These values are similar to those reported for printable concrete by Rushing et al. (30-38 MPa at seven days after mixing) [10]. It could be realistic to expect, due to the geometry of the printed filaments (high surface area), that strength may be gained even more quickly in a printed form.

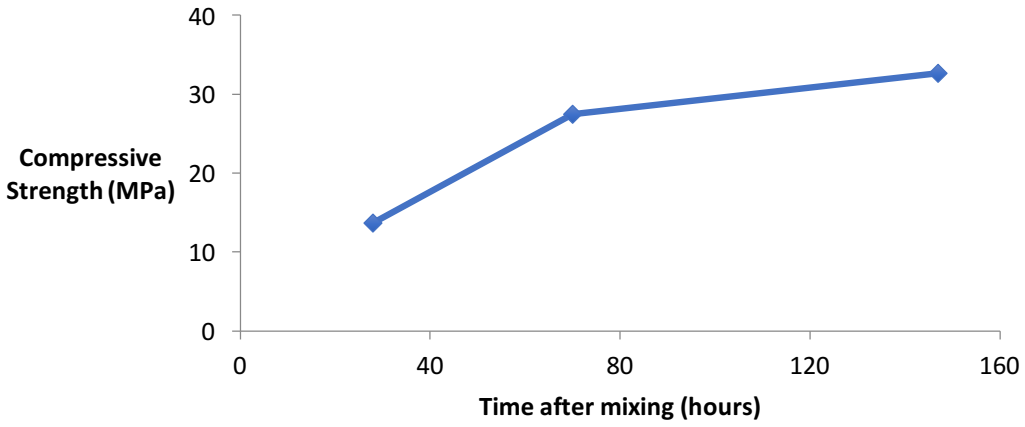

Figure 3.15: Early strength of the Mix 5 printable ECC composition is measured over time

3.3.4 Interlayer Bonding Characterization

The interlayer bond strength is another important aspect of the printed form of cementitious composites. To characterize the strength between adjacent printed filaments coupon tensile specimens were sectioned from the printed pattern pictured in Figure 3.16. Specimens were printed and cured in the partially supported 45-degree angle arrangement pictured. Filaments were aligned normal to the axis of loading.

Figure 3.16: Preparation of the print pattern to be used in interlayer bonding testing of Mix 4 via the approximated 3D printing technique. Coupon shaped specimens were sectioned from the print pattern and tested in tension with the loading axis normal to the bond lines between filaments.

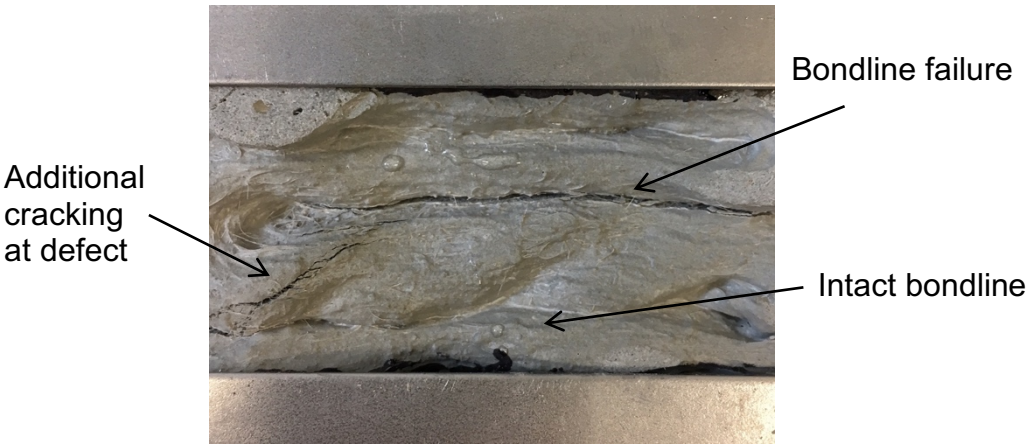

Figure 3.17: An example of a tested interlayer bonding specimen

Four specimens of the Mix 4 composition were tested. The average interlayer bond strength was measured to be 0.9 MPa with a standard deviation of 0.5 MPa. This is a conservative characterization of the average interlayer bond strength as it represents the weakest of the three

bond lines in each tensile specimen. An example of a tested specimen is seen in Figure 3.17. All specimens ultimately failed along one of the bond lines within the gage section, though all specimens showed a plurality of cracks, demonstrating a degree of failure suppression.

Improvement in interlayer bonding is necessary for implementation on the full-scale and will significantly improve the durability and resilience of the full-scale printed structures. Potential strategies to improve this bonding include compositional adjustment, surface texturing/grooves created in deposited filaments to mechanically anchor subsequent layers, and the automated inclusion of interlayer fibers to "stitch" layers together.

3.3.5 Batch Recalibration for Printable Compositions

It was seen that batch size has an effect on the fresh state properties of the cementitious compositions reported here. Larger batch sizes generally showed higher flowability and slower rates of hardening than the same composition proportions mixed in the small batch size (1.2L), as illustrated for Mix 4 in Figure 3.18.

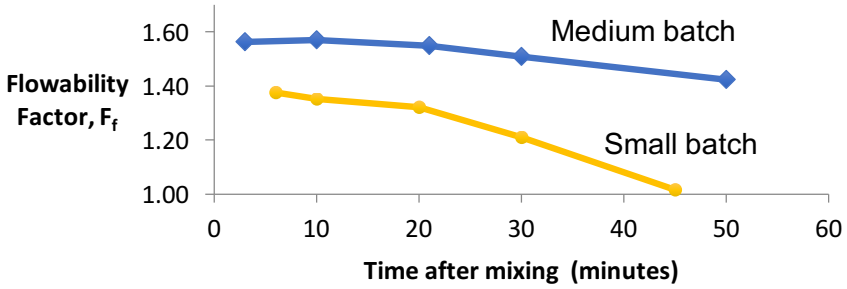

Figure 3.18: Comparison of flowability evolution for Mix 4 mixed in small (1.2 L) and medium (3.1 L) batches. The flowability evolution associated with the small batch here is considered more appropriate for use with the 3D printing process.

A mix composition that mimicked the flowability evolution seen in the small batch version of Mix 4 in the medium batch size was derived by reducing the CA content, adding attapulgite nanoclay, and using a water content with an elevated temperature. The flowability evolution of this recalibrated composition (Mix 5) is compared to that of Mix 4, mixed in a small batch, in Figure 3.19. CA content was reduced based on the results reported in Section 3.3.6, ANC was

added based on results of Section 3.3.1 and 3.3.6, and the use of elevated water temp. was based on results reported in Section 3.3.2.

Batch size is a processing parameter that should be accounted for in scaling processing of printable cementitious materials. The results reported in Sections 3.3.1 and 3.3.2 can be used to guide material design.

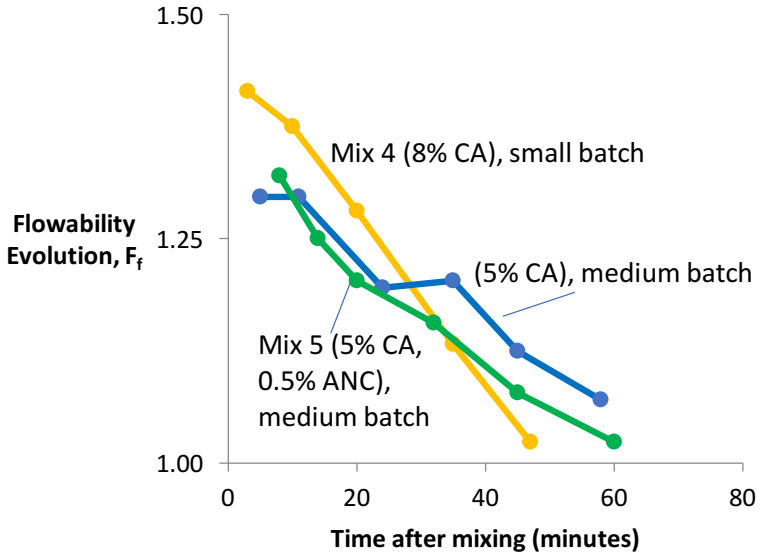

Figure 3.19: The flowability of the Mix 4 composition can be approximated in a larger batch size when the calcium aluminate cement composition is reduced to 5.0% C.M and with the addition of 0.5% Attapulgite nanoclay. Both medium batches included here use 37° C water, while the small batch uses room temperature water.

3.3.6 Workability Loss Evaluation

Under the workability loss test scheme described in Section 3.2.4, Mix 4 exhibited significant workability loss. As seen in Figure 3.20, with an additional 15 minutes of applied shear agitation (mixing), the fresh state material showed reduced flowability factor values at every time interval. Even if this (+15 min mixing) flowability curve is shifted 15 minutes on the x-axis (as represented by the dotted curve in Fig. 3.20) to account for the additional time spent in the mixer, the flowability factors are still less than those values at the same time intervals for the portion of the mix not subjected to additional mixing. This indicates that for this composition, continued shear agitation *accelerates* hardening and loss of workability, which is not desirable for consistent, controllable printing performance.

Attapulgite nanoclay and reduced CA content were seen to reduce workability loss to near zero, a target behavior for printability. Figure 3.21 shows the flowability evolution for compositions with an ANC contents of 0.5% C.M. and 0.8% C.M (each with a calcium aluminate cement content of 5.0% C.M. and 37°C water), when mixed for 28 and 43 minutes after the addition of water. The composition with ANC content of 0.5% C.M. is Mix 5, and is detailed in Table 3.2. For both the 0.5% and 0.8% ANC compositions, the portion of the paste (including fibers) that was mixed for an additional 15 minutes shows matching flowability evolution to those portions only mixed for 28 minutes, indicating near zero workability loss under continued shear agitation.

Near zero workability loss allows the material to exhibit the "harden on command" type behavior described in Figure 3.3 as being a target for printability.

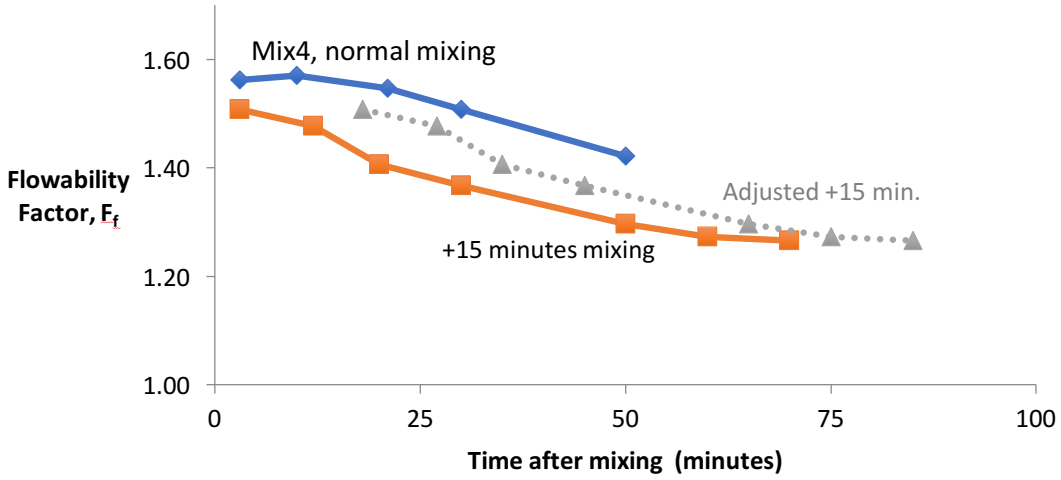

Figure 3.20: Mix 4 showed significant workability loss, indicated by the lower flowability factor values at similar time intervals, under an additional 15 minutes of shear agitation. The discrepancy between the top curve and the dotted curve illustrates the contribution of additional mixing, as opposed to simply time, to workability loss for this particular composition.

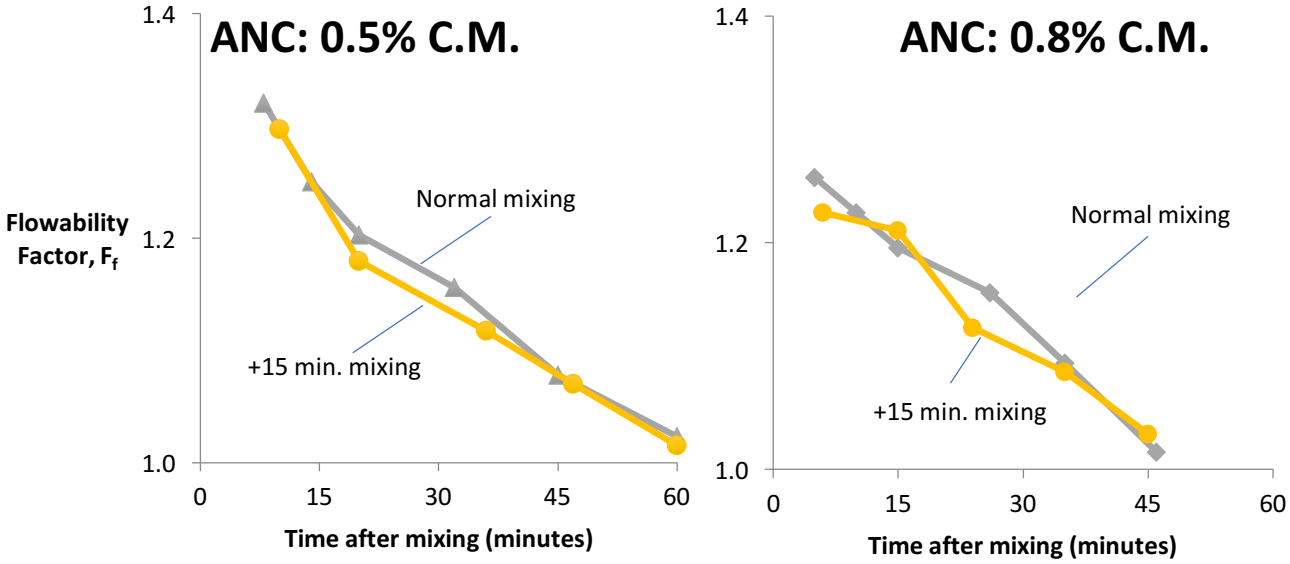

Figure 3.21: Compositions with calcium aluminate cement content of 5.0% C., 37°C water, and ANC content of (a) 0.5% C.M. and (b) 0.8% C.M., show minimal workability loss under an additional 15 minutes of shear agitation (mixing); minimal workability loss under these conditions indicate a highly consistent printable material.

3.3.7 Scaled Printing Approximation

Due to the minimal workability loss, appropriate flowability evolution, and robust strain-hardening behavior (Fig. 3.22) exhibited by the Mix 5 composition, it was used for a large-scale printing approximation (Fig. 3.23).

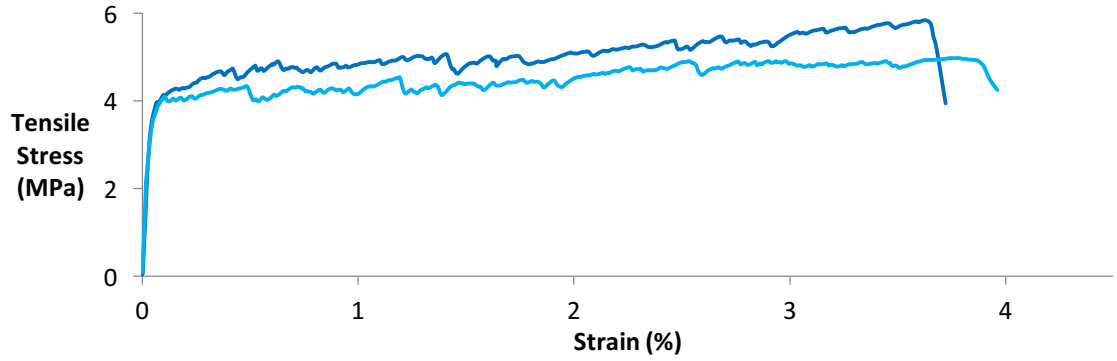

Figure 3.22: Representative stress-strain curves illustrating the tensile performance of the Mix 5 composition, showing robust strain-hardening behavior

The Mix 5 composition exhibited great extrudability and immediate buildability as well as sustained printability over a period of time. The material showed clay-like workability with shear thinning behavior and rapid rebuilding that allowed both extrusion and buildability with minimal deformation of layers under the weight of subsequent layers. Several stacks of 6-9 layers, and 30 cm in length, were produced. The filament produced was approximately 1cm thick (height) and 4 cm wide. The rate of deposition was intentionally slowed to simulate the longer time between deposition passes that would be characteristic of larger print sizes.

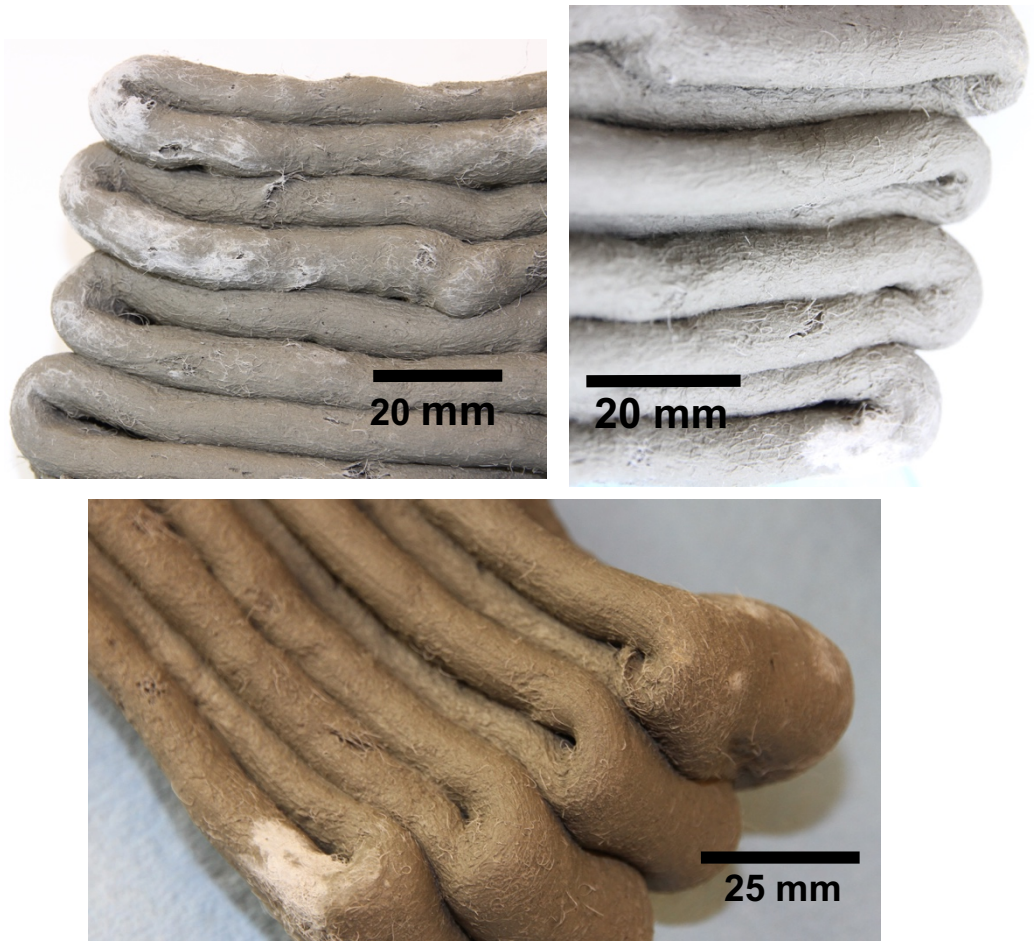

Figure 3.23: Large-scale printing approximations produced with the Mix 5 composition, showing a combination of extrudability, buildability and appropriate hardening/early strength behavior

3.3.8 Cost considerations

Regarding the cost of such printable SHCCs, the bill of materials (including the PVA polymer fibers) includes only ingredients already used in full-scale, presumably economically feasible, construction applications of concrete. With the inclusion of polymer fibers and specialty

materials like purified Attapulgite nanoclay, the cost per unit volume is unavoidably higher than the simplest printable concretes, however, the advantages provided over those low strength printable concretes, both in expanded utility and mechanical performance, offer a significant value proposition. Similarly, the 3D printing process can offer significant advantages over traditional casting methods for many applications, especially when it is considered that the molding framework, and labor associated with it, constitutes 35-60 percent of the cost of a traditional concrete structure, and produces a significant amount of waste [27]. Requiring no temporary framework, 3D printing processes eliminate that cost and waste.

Comparative costing with printable concretes currently used for commercial large-scale printing projects is difficult due to the proprietary nature of such materials. Reports of the use of geopolymer materials (by the company Cazza, for example) hint that the costs of these non-fiber-reinforced materials are similar to that of the printable SHCCs reported here.

The price point of the printable SHCCs, like those reported here, can be a design variable for various applications and performance targets. The use of polypropylene (rather than PVA) fibers would be an effective strategy to lower the cost per volume, while more expensive ultra-high molecular weight polyethylene fibers and specialty cements could be used to boost compressive and tensile strengths, while maintaining a 3-5% strain capacity.

3.4 CONCLUSIONS

The influences of several compositional ingredients on fresh state flowability evolution were reported. Calcium aluminate cement, HPMC, microsilica, ground silica, purified and exfoliated attapulgite nanoclay, and water content were used to manipulate fresh state rheological behavior. HPMC can be used to manipulate initial flowability, but is not effective in manipulating rate of hardening. Dosage of CA is seen to have a large effect on rate of hardening, as well as on initial flowability. Substituting MS and GS for a fractional portion of silica sand content also increases rate of hardening, while maintaining initial flowability. Small amounts of ANC reduced time to hardening via reduced workability, but showed only a slight effect on rate of hardening. For compositional additions or substitutions, water content may need to be adjusted to allow proper mixing and fiber dispersion, which can both affect mechanical performance.

A printable cementitious material design paradigm, based on minimizing workability loss under continued shear agitation, was proposed and used to guide printable cementitious composite development. Purified and exfoliated attapulgite nanoclay was seen to minimize workability loss under relevant processing conditions. The workability loss mitigation provided by ANC was negated when increased rate of hardening caused by excessive CA content dominated. A limited CA content in combination with ANC is recommended to maintain low workability loss for robust printability.

Batch size and temperature of the water content added during processing were seen to be two processing parameters that have a significant effect on fresh state rheological properties. Water temperature can also be used to intentionally manipulate fresh state properties. It is recommended that both batch size and water temperature be monitored and controlled for consistent, predictable printing performance.

Compositions exhibiting both extrudability and buildability in the fresh state and interlayer bonding and robust strain-hardening in the cured state were systematically designed and demonstrated on a variety of scales. The mesoscale material structuring produced by the printing process was seen to improve mechanical performance in direct tension due to fiber alignment, without negatively affecting compressive strength.

The early stage properties of the Mix 5 composition indicate a promising printable composition. Robust tensile strain-hardening behavior of this composition has been confirmed, which will contribute to durability and resilience of the material and structural members produced with it. This printable ECC material exhibited tensile strain capacity of ~4.0%, and tensile strength approaching 6 MPa. Compressive strength for this composition is gained quickly, conservatively measured to reach 30 MPa within 6 days. Extrudability and immediate buildability was observed during a demonstration of an approximated printing process.

The effects of compositional ingredients and processing parameters demonstrated in this paper can be used to manipulate the early stage behaviors as needed for specific applications, processing equipment, and project scale.

REFERENCES
(Chapter III)

[1] S. Lim, R.A. Buswell, T.T. Le, S.A. Austin, A.G.F. Gibb, T. Thorpe, Developments in construction-scale additive manufacturing processes, Autom. in Constr., Volume 21, Pages 262-268, January 2012.

[2] N. Labonnote, A. Rønnquist, B. Manum, P. Rüther, Additive construction: State-of-the-art, challenges and opportunities, Autom. in Constr., 72, pp. 347-366, 2016.

[3] P. Wu, J. Wang, X. Wang, A critical review of the use of 3-D printing in the construction industry, Autom. in Constr., 68, pp. 21-31, 2016.

[4] F. Bos, R. Wolfs, Z. Ahmed & T. Salet, Additive manufacturing of concrete in construction: potentials and challenges of 3D concrete printing, Virtual And Phys. Prototyp., Vol. 11 , Iss. 3, 2016.

[5] Y.W. D. Tay, B. Panda, S.C. Paul, N.A.N. Mohamed, M.J. Tan, and K.F. Leong, 3D printing trends in building and construction industry: a review,
Virtual and Phys. Prototyp., 2017.

[6] Keating, S.J., J.C. Leland, L. Cai, N. Oxman, Toward site-specific and self-sufficient robotic fabrication on architectural scales, Sci. Robot., 2, 26 April 2017.

[7] A. Warszawski and R. Navon, "Implementation of Robotics is Building: Current Status and Future Prospects", J. of Constr. Eng. and Manag., Vol. 124, Issue 1, pp. 31-41, 1998.

[8] D. Hwang and B. Khoshnevis, An Innovative Construction Process-Contour Crafting (CC), Proceedings of the 22nd International Symposium on Automation and Robotics in Construction ISARC 2005, Ferrara, Italy, September, 2005.

[9] R. A. Buswell R. C. Soar , A. G. F. Gibb, and A. Thorpe, Freeform Construction: Mega-Scale Rapid Manufacturing for Construction, Autom. in Constr., 16 (2), pp. 224-231, 2007.

[10] T.S. Rushing , G. Al-Chaar , B.A Eick , J. Burroughs , J. Shannon , L. Barna , and M. Case, Investigation of concrete mixtures for additive construction, Rapid Prototyp. J., Vol. 23 Issue: 1, pp.74-80, 2017.

[11] T.T. Le, S.A. Austin, S. Lim, R.A. Buswell, A.G.F. Gibb, T. Thorpe, Mix design and fresh properties for high-performance printing concrete, Mater. and Struct., Vol. 45, Issue 8 pp. 1221, 2012.

[12] A. Kazemian, X. Yuan, E. Cochran, and B. Khoshnevis, Cementitious materials for construction-scale 3D printing: Laboratory testing of fresh printing mixture, Constr. and Build. Mater., Volume 145, Pages 639–647, 1 August 2017.

[13] M. Hambach and D. Volkmer, Properties of 3D-printed fiber-reinforced Portland cement paste, Cem. and Concr. Composites, Volume 79, Pages 62–70, May 2017.

[14] S. Metsa-Kortelainen, T. Vehmas, J. Lagerbom, A. Kronlof, R. Mahlberg, H. Heinonen, Biomimetic building of 3D printed tailored structures, VTT Technical research Centre of Finland, Research Report VTT-R-00669-14 MIMECOMP commissioned by Tekes (public), March 2014.

[15] V.C. Li, On Engineered Cementitious Composites (ECC): A Review of the Material and Its Applications, J. of Adv. Concr. Technol., Vol. 1, No. 3, 215-230 November 2003.

[16] H. Kong, S.G. Bike, and V.C. Li, Constitutive rheological control to develop a self-consolidating engineered cementitious composite reinforced with hydrophilic poly(vinyl alcohol) fibers, Cem. and Concr. Composites, Volume 25, Issue 3, Pages 333–341, April 2003.

[17] Y.Y. Kim, H. Kong, and V.C. Li, Design of Engineered Cementitious Composite Suitable for Wet-Mixture Shotcreting, ACI Mater. J., V. 100, No. 6, pp. 511-518, Nov 2003.

[18] Q. Zhang and V.C. Li, Development of durable spray-applied fire-resistive Engineered Cementitious Composites (SFR-ECC), Cem. and Concr. Composites, 60, pp. 10-16, 2015.

[19] Z. Quanji, Thixotropic behavior of cement-based materials: effect of clay and cement types, Iowa State University, Graduate Theses and Dissertations, Paper 11724, 2010.

[20] Ö. Kirca, Temperature effect on calcium aluminate cement based composite binders, The Graduate School of Natural and Applied Sciences of Middle East Technical University, Doctoral Thesis, July 2006.

[21] G. Abbas, S. Irawan, K.R. Memon, S. Kumar and A.A.I. Elrayah, Hydroxyproylmethylcellulose as a primary viscosifying agent in cement slurry at high temperature, Int. J. of Automot. and Mech. Eng., Volume 8, pp. 1218-1225, July-December 2013.

[22] Th.M., Salem, Electrical conductivity and rheological properties of ordinary Portland cement–silica fume and calcium hydroxide–silica fume pastes, Cem. and Concr. Res. 32(9):1473-1481, September 2002.

[23] A.R. Hariharan, A.S. Santhi, and M. Ganesh, Study on Strength Development of High Strength Concrete Containing Fly ash and Silica fume, Int. J. of Eng. Sci. and Technol., Vol. 3 No. 4 Apr 2011.

[24] S. Kawashima, M. Chaouche, D.J. Corr, and S.P. Shah, Rate of thixotropic rebuilding of cement pastes modified with highly purified attapulgite clays, Cem. and Concr. Res., 53, 112-118, 2013.

[25] S. Kawashima, M. Chaouche, D.J. Corr, and S.P. Shah, Influence of purified attapulgite clays on the adhesive properties of cement pastes as measured by the tack test, Cem. and Concr. Composites, 48, 35-41, 2014.

[26] JSCE, "Recommendations for Design and Construction of High Performance Fiber Reinforced Cement Composites with Multiple Fine Cracks (HPFRCC)", Concrete Engineering Series 82, Japan Society of Civil Engineers, March 2008.

[27] R. Rael and V. San Fratello (of Rael San Fratello Architects), Developing Concrete Polymer Building Components for 3D Printing, Association for Computer Aided Design in Architecture (ACADIA) Conference 2011, University of Nebraska-Lincoln College of Architecture, March 10-12, 2011.

CHAPTER IV

Nacre-inspired composite design approaches for high energy dissipation in large-scale cementitious members and structures

4.1 INTRODUCTION

4.1.1 Bio-inspiration from Nacre

Nacre, the iridescent material seen on the interior of shells like that of the abalone is one of the seminal natural materials to motivate the biomimicry/bio-inspiration paradigm across science and engineering disciplines. Previous research has illuminated how nacre is able to exhibit an impressive combination of high compressive strength, high tensile strength, and high tensile ductility, despite being composed 95% of a relatively weak and brittle, chalk-like mineral called aragonite [1-9]. Nacre has been shown to require 1000-3000 times as much energy to cause failure than the bulk form of its principal component, aragonite [3,8]. Nacre is a shining example of nature's ability to leverage structure via shaping to turn a relatively limited palette of compositional building blocks (Oxygen, Hydrogen, Carbon, Nitrogen, Calcium, Magnesium etc.) into an immense and diverse ecosystem of materials, many of which outperform deliberately human-engineered materials in a variety of ways [7,10,11].

It has been seen that the structuring of nacre promotes specific deformation mechanisms that are responsible for the dramatic transformation of brittle aragonite into a material that exhibits tremendous toughness (the amount of energy required to cause the material to fail) [1,2,4-9]. There are four principle features of nacre's hierarchical structuring that have been observed and reported to be key in these deformation mechanisms. Nacre is composed of (1) distinct layers, with primary mineral layers composed of (2) discrete, tiled, hexagonal aragonite tablets, with boundaries off-set from those of the tablets in the layers above and below, each tablet having a

(3) markedly rough or wavy surface that nests into adjacent mineral layers, as well as (4) secondary, thin bio-polymeric layers between mineral tablets, which allow sliding of the tablets relative to each other, while also providing some physical resistance as sliding progresses [1]. This structure, a simplified illustration of which is pictured in Figure 4.1, has been called a "brick-and-mortar" arrangement previously. However, in literal brick and mortar structures, the mortar does not allow for the stretching or "give" within a given layer, nor the shear sliding between layers—both of which are key for the deformation mechanisms observed in nacre.

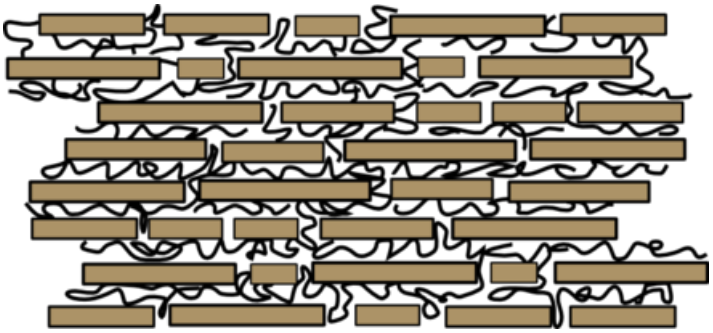

Figure 4.1: A schematic of the layered tablet, "brick and mortar" structure of nacre [image from Wikipedia Commons]

The deformation mechanisms seen in nacre allow a combination of tensile strength and ductility, macroscale tensile strain-hardening and shear-hardening behavior, and flaw and damage tolerance, each of which contribute to material toughness. The discrete tablets allow a "give" in the structure under tension and shear, which, as a result of local slip-hardening mechanisms, can be distributed throughout the material, instead of localizing at weak points and stress concentrations. These deformation mechanisms suppress brittle failure, increasing durability, and controlling damage such that it can later be repaired through natural processes, promoting resilience in the material.

Nacre's impressive mechanical performance has inspired a multitude of synthetic nacre materials [12-16]. However, these previous attempts at mimicry of nacre's structure have shared the same thin-sheet size scale and/or slow manufacturing/growth processes of natural nacre, making them irrelevant for large-scale structural applications. A major bottle neck in the development of synthetic, nacre-inspired materials is the time and cost-efficient arrangement of the multitude of tablet elements, which is particularly challenging for scalable manufacturing at large size scales.

4.1.2 Improved structural cementitious materials via inspiration from nacre

As addressed in Section 1.1 of this dissertation, traditional concrete is (1) the most used human engineering material in the world, serving as the ubiquitous basis of our built environment, and (2) has severe durability and resilience limitations due to weakness in tension, which makes a significant portion of concrete infrastructure, as currently constructed, unsustainable [17]. These facts together highlight the significance of improved cementitious materials.

Beyond durability under normal service conditions, concrete infrastructure also needs to withstand extreme loading events to ensure human safety in events like naturally occurring disasters, and even malicious attacks, of seemingly unlikely scale. Resiliency, defined as the ability to minimize the probability of failure, minimize the consequences of failure, and minimize the time between failure and a return to service, becomes increasingly important and challenging in these extreme cases.

To address the shortcomings in durability and resiliency of concrete, we look to nature, which seems to have already solved this problem. Can the composite design strategies observed in nacre to boost tensile strength and material toughness in an otherwise weak and brittle material be effective on a much larger scale, such as that which is applicable to civil infrastructure? This study aims to answer that question and explore ways this can be achieved.

As previously noted, nacre's impressive mechanical performance is due to its structuring and deformation mechanisms associated with that structuring. This improvement in performance has been determined to be derived from the aforementioned shaping paradigm of natural materials. A portion of this improvement is likely a product of size effects associated with the micron sized aragonite tablets (~8 μm in diameter, 0.5 μm thickness), as discussed by Rim et al. [15]. For realistic, widely applicable structural building materials, it is not feasible to exploit size effects due to processing constraints associated with the scale of the end-product. This research focuses, instead, on the contributions of shaping considerations, other than size effects, to the improvement of mechanical performance of nacre over that of bulk aragonite, and how those shaping strategies can be adapted for application in large-scale, structural building materials.

4.1.3 Large-scale nacre-inspired structure via SHCCs

Strain-hardening cementitious composites (SHCCs), also known as Engineered Cementitious Composites and "bendable concrete", are cement based materials suitable for large scale processing and application that exhibit a characteristic distributed microcracking pattern and tensile strain-hardening behavior when subjected to tensile loading above the elastic limit threshold. The micromechanics of SHCCs have been described previously in detail [18], and differ from those of other fiber reinforced concretes. In short, when the brittle cementitious matrix first fractures in tension, the dispersed fibers are able to bridge the crack, holding the crack to several tens of microns in width, while carrying the tensile load such that further opening of the microcrack (via fiber pullout) requires more energy than originating a microcrack elsewhere in the matrix. This cycle can be repeated many times, such that the composite is able to distribute deformation throughout and suppress brittle fracture failure.

The characteristic distributed microcracking tensile behavior of SHCCs provides a convenient route to produce an approximated analog of the natural nacre structure. When strained in tension, a plurality of microcracks open in the SHCC material at the weakest locations in the cementitious matrix, leaving between them stronger, discrete units, analogous to the tablets in nacre. Under unidirectional tension, the analog discrete units would be strips, rather than tablets, however, microcracks will occur in an orientation normal (perpendicular) to any tensile loading direction, so if tensile stress is applied in multiple directions, tablet-like architecture would theoretically be generated. Moreover, ECC produces a "give" at a certain threshold tensile stress, while also providing resistance to continuing tensile strain (as evidenced by the tensile strain-hardening behavior), just as in nacre.

When layers of ECC are stacked, an approximation of the nacre structure can be created. Microcracks opening in each of the ECC layers are probabilistically unlikely to line up, producing the off-set arrangement of stacked discrete units like that of nacre. In this way, crack propagation could be manipulated to require a higher amount of energy to cause failure.

Similar to nacre's ability to control damage to a degree that it can later be repaired via natural processes, ECC's microcracks are held to tight widths (tens of microns across) that allow cracks

to self-heal with exposure to water and air [20]. This previously documented behavior of ECCs can be leveraged in a nacre-inspired composite scheme to lend resilience.

Using ECCs to approximate the nacre structure in a form applicable to civil infrastructure is appealing because it provides an efficient solution to the principal challenge of producing synthetic nacre-inspired materials: the arrangement of the myriad discrete units.

While ECCs themselves are inherently a more durable, resilient alternative to typical, brittle concrete materials [18, 19, 21], this study seeks to determine if material design lessons learned from nacre can *further* improve the performance of ECCs, in addition to determining if these lessons are applicable and have utility on size scales relevant for civil infrastructure.

Preliminary testing [22] showed that nacre-inspired layering and waviness, applied to an ECC material, enhanced composite performance in flexure, boosting inelastic flexural toughness by as much as 140%. The work presented here investigates the performance of additional nacre-inspired design schemes in flexure, as well as in direct tension. The most promising design schemes are characterized in compression.

Rather than devise an optimized large-scale building material or product, this investigation aims to determine how nacre-inspired composite design features and approaches can affect the mechanical performance of structural cementitious materials on a size-scale much larger than that of natural nacre. Lessons learned from this study may be applied to develop cementitious composite materials and members for critical infrastructure components requiring extreme toughness, durability, and resiliency. Structural components designed for seismic, impact, and blast resistance/mitigation are prime candidates for such improvements in mechanical performance.

4.2 MATERIALS AND METHODS

4.2.1 Compositional Materials

A high strength ECC material, originally developed by Ranade et al. (2011), is used as the basis of all the nacre-inspired composite designs investigated herein [23, 24]. The composition of this material, referred to henceforth as HSHDC (high strength, high ductility concrete) is described in Table 4.1. The compositional ratios in Table 1 are reported as the percentage of the total cementitious material by weight (%CM), where the Type H cement and microsilica (also called silica fume) are considered cementitious material. A 2% volume fraction of ultra high molecular weight polyethylene (UHMW-PE) polymer fibers are included. Additional information about the ingredients of the HSHDC composition can be found in Appendix IV.1 and in Ranade et al. (2011) [24]. This composition and its mixing procedure is kept consistent throughout the study.

Table 4.1: The compositional ratio of the HSHDC material used as the primary component of each bio-inspired composite design investigated in this study. Composition is reported here as percentage of the total cementitious, except fiber content.

Ingredient	**%CM**
Class H Cement	72.00
Microsilica	28.00
Ground Silica	19.90
F-60 Sand	50.40
Water	*15.00
HRWRA	1.30
Coupling Agent	0.75
UHMW-PE Fiber	2.00% by vol.

**Plus water content of soaked fibers: 0.3-0.4 g water per gram of total fibers (dry weight)*

The mixing process of the HSHDC is highly compatible with typical concrete mixing equipment, however, the highly densified nature of the material requires a particular sequence of ingredient addition to ensure proper mixing and dispersion of fibers. The mixing procedure used for this study is described in Appendix IV.2.

This study does not investigate the HSHDC material per se; rather, it is the nacre-inspired structuring approaches that are investigated. The structuring approaches considered in this study are designed to be applicable with any strain-hardening cementitious composite that has been designed for casting. The HSDHC material is simply a model ECC/SHCC material that was selected for this study to explore if the hypothesized strength and toughness enhancing benefits of the nacre-inspired could potentially push ECC performance into a cementitious materials performance "whitespace" –a previously unachieved property profile.

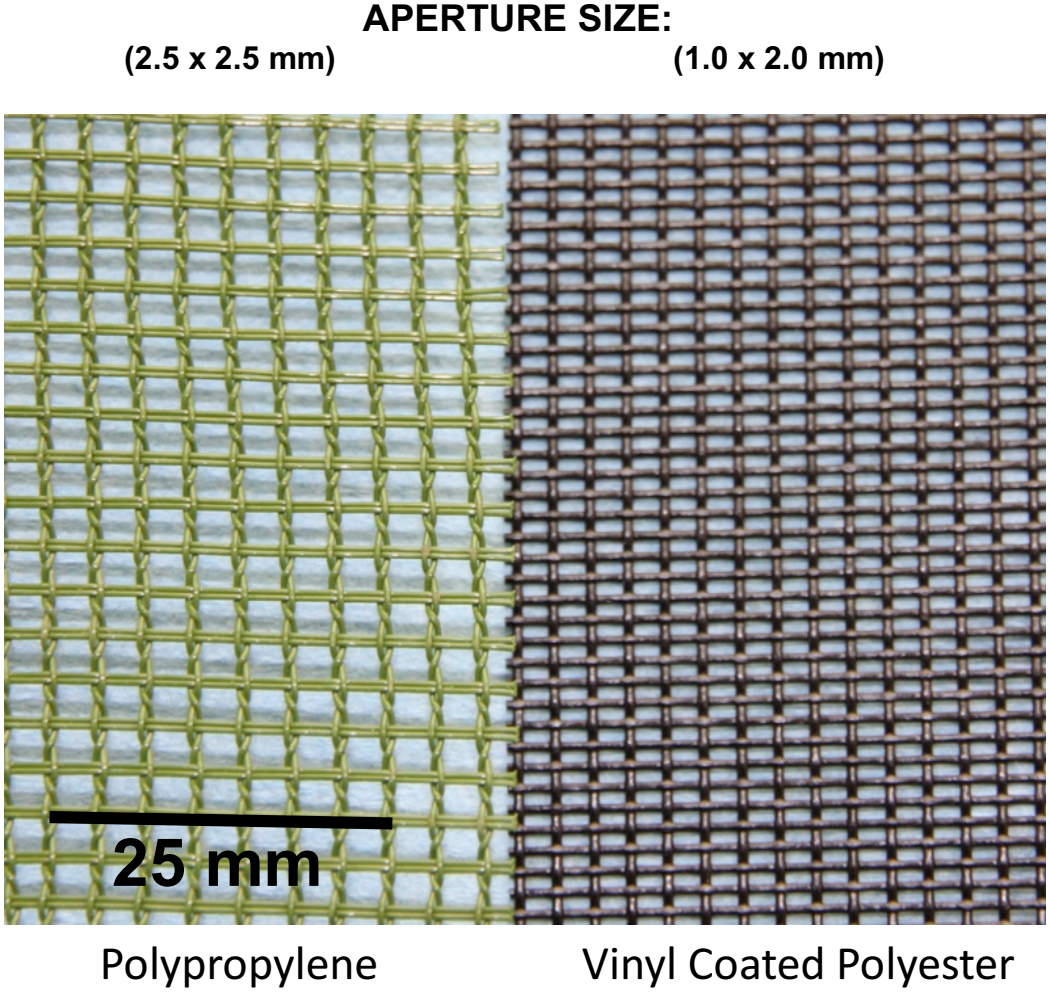

Figure 4.2: The appearance of the two polymer meshes used in this study are compared

Several of the nacre-inspired design schemes introduce additional materials into the composite. A commercially available, high strength polyurethane-based adhesive is used for one scheme,

and a variation of that scheme. Polymer mesh materials are used for several other schemes. One mesh is a commercially available, polypropylene geotextile mesh ("PP-Mesh") marketed for soil stability and soil separation in large-scale landscaping/construction applications. It is alkali resistant and rated for a 75 year service life, per a manufacturer-provided data sheet. Use of a vinyl-coated polyester mesh ("VCP mesh"), marketed as a tear-resistant window/door screen material, is also investigated. The appearance of these polymer meshes is described and compared in Fig. 4.2.

4.2.2 Mechanical testing methods

This study seeks to compare the performance of the structured composite design schemes to that of the monolithic HSHDC material to determine mechanical performance benefits produced by the nacre-inspired design schemes. Performance is compared in direct tension, beam bending (flexure), and compression. Specimens are tested between 14 and 19 days after casting, following an accelerated curing process (see Appendix IV.2).

Testing in direct tension is performed on a 110kip load capacity Instron instrument, using large-scale dogbone shaped specimens to accommodate the various nacre-inspired layering schemes described in Section 4.3. The size and shape of large dogbone shaped specimen is depicted in Figure 4.3. A pre-loading rate of 0.75 mm/min is used to allow the specimens to settle into the grip fixtures. When a pre-load of ~2 kips is achieved, the loading rate is increased to 1 mm/min and data collection is started.

Tensile stress is computed based on measurements of the gage section cross-section of each individual specimen. Tensile strength for each bio-inspired scheme is recorded as the average of the maximum stress carried by each specimen. Strain capacity is recorded as the tensile strain value at the maximum stress, based on change in gage section length as measured by LVDTs attached to each specimen.

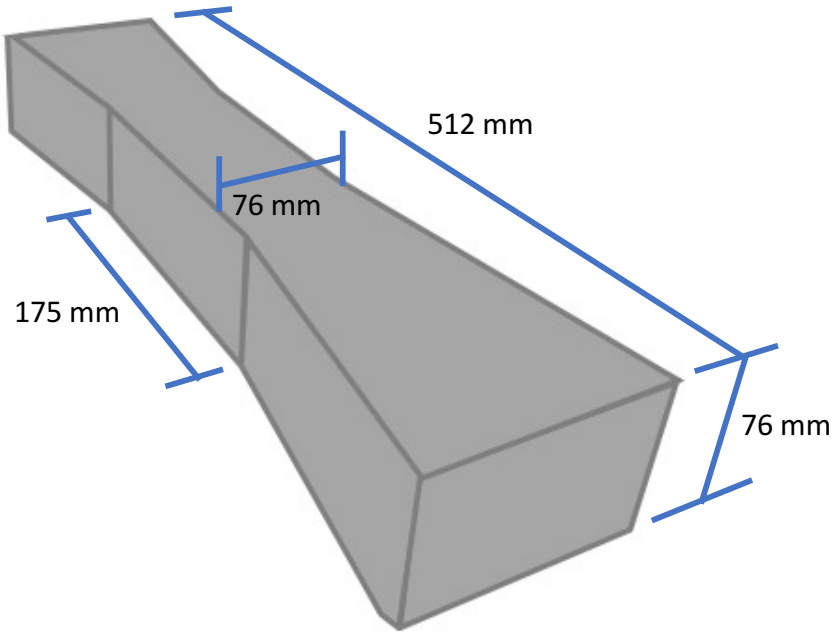

Figure 4.3: The large dogbone shaped specimens have a gage section cross-section approximately 76 x 76 mm, and gage length of ~ 175 mm

Four-point bend testing is performed using a 22 kip load capacity MTS universal testing machine. A support span of 10 inches is used with a loading span of 3.5 inches. Fixed displacement loading was applied while load and "average third point displacement" were recorded. Average third point displacement is a measurement of displacement at the top two loading support points, as measured by instrument stroke during testing. Beam specimens with approximate height of 75 mm and width of 68 mm are used. Because specimens are sectioned to size, and each have slightly different dimensions, every specimen is measured prior to testing and those measurements are used to calculate the flexural stress for each specimen individually. Flexural stress is calculated according to Equation 4.1, where F is force in Newtons, L is the support span (254 mm), b is the width of the specimen, and d is the height.

$$\text{Flexural Stress, } \sigma_f = (FL) / (bd^2) \qquad \text{(Eqn. 4.1)}$$

Modulus of rupture is calculated as the maximum flexural stress carried by a specimen. Inelastic flexural toughness is also calculated, providing a convenient metric to compare the toughness of the composites in flexure. The process of calculating inelastic flexural toughness is described in Soltan et al (2014) [22], and is a function of the elastic limit in flexure, the modulus of rupture,

and the deflection at which the stress carrying capacity of the beam has decayed to 90% of the modulus of rupture, after peak load has been reached.

Compression testing was performed with a Forney compression machine using cube-shaped specimens. A loading rate of ~50 psi/s was used, based on recommendations of the ASTM C109 International standard. Compressive strength is reported as the stress at the maximum load sustained by the composite.

4.3 APPROACHES TO PHYSICAL MODELING OF THE NACRE-INSPIRED STRUCTURE

Several design schemes are explored to incorporate nacre-inspired features associated with the key deformation mechanisms observed in nacre, on a scale and in a material applicable for full-scale construction and infrastructure.

All the design schemes reported here use the specific compositional version of ECC developed by Ranade et al. (2013) and described in Section 4.2.1, which has been previously reported to have high compressive strength, high tensile strength, and high strain capacity (i.e ductility)[23]. This high strength ECC, called HSHDC, forms what are hereafter referred to as “primary layers” within the various nacre-inspired design schemes.

The HSHDC material is not a direct analog to the aragonite material found in nacre. Aragonite is inherently brittle and weak in the bulk state. The HSHDC material is composed of a densified, high strength cementitious matrix, which could be thought of similarly to the high strength exhibited by the microscale aragonite tablets, but also includes 12.7 mm long, 38 micron diameter ultra-high molecular weight polyethylene fibers. These high tenacity polymer fibers do not have a direct analog in the nacre structure; however, they allow the segmentation of the HSHDC cementitious matrix material under tensile stress that approximates the tablet structure of nacre. As the cementitious matrix undergoes multiple cracking under tensile stress, the polymer fibers also provide a resistance to further deformation, similarly to the ligamental biopolymer connections between tablets within the same layer in natural nacre (Figure 4.4).

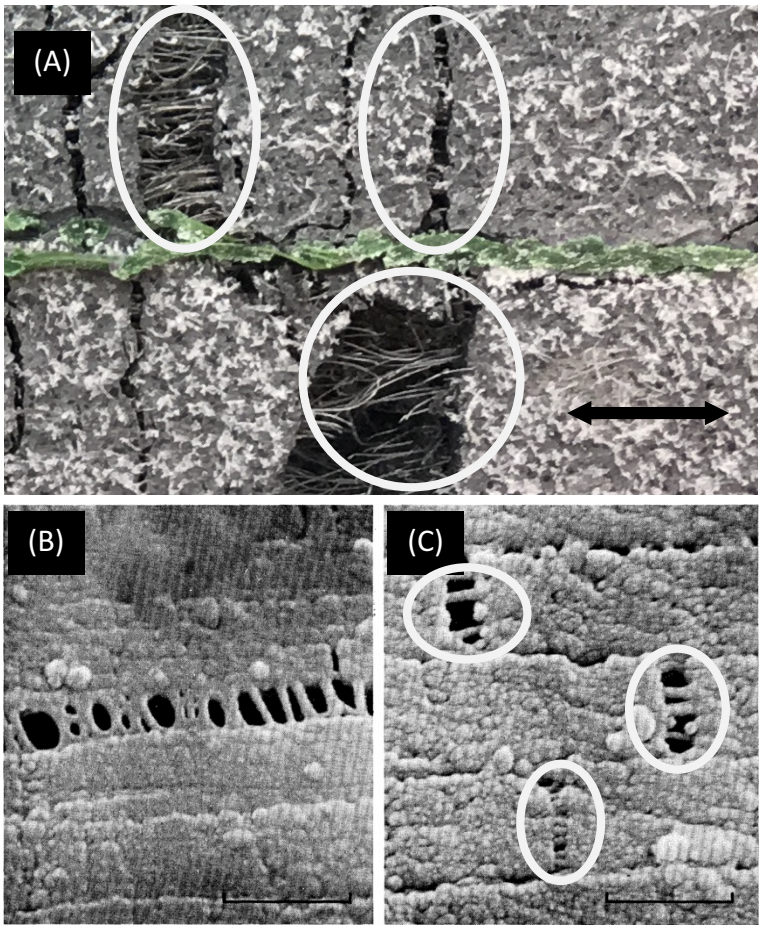

Figure 4.4: The crack-bridging fibers in HSHDC (circled in A) contribute to strain hardening behavior in the material, similarly to the biopolymer component between intralayer tablets (circled in (C)) in nacre. The biopolymer component between layers in nacre (B) inspires several other analog features in the structural composites investigated in this study. Scale bars: (A) = 8 mm, (B) and (C) = 0.60 microns [(B) and (C) adapted from A.P. Jackson et al., 1988 (Proc. R. Soc. Lond. B)]

These nacre-inspired composite designs, based on the ECC material system are not meant to be direct mimics of nacre's structure, but instead interpretative adaptations of the structure being realistically applicable to large scale construction applications. It is the generation of nacre-inspired deformation mechanisms, on a larger size scale, that is prioritized and targeted for investigation.

There are two main approaches to the physical adaptation of nacre's structure and deformation mechanisms to a large-scale structural material reported here. The first is stacking multiple layers

of precast ECC in various ways and manipulating the interface between the layers. The second approach is creating distinct layers within the cementitious composite via inlayed mesh materials. Each approach incorporates approximations of key features seen in nacre through different processing and compositional routes.

The physical model design approaches and processing steps explored have been deemed to be feasible within the realistic constraints of large scale construction. While these design schemes have been devised be realistic for actual large-scale application, the forms in which they are presented are meant to serve simply as simplified physical models of various nacre-inspired design strategies and have not been optimized. There remain several parameters for each design scheme that could be further tuned to manipulate mechanical performance, cost, and other application specificity.

Table 4.2: The nacre inspired composite design schemes and the control schemes are labeled and described

Summary of composite design schemes		
Type	**Label**	**Description**
Monolithic	Pour casting	Typical large application processing, material poured into mold
	Layered casting	Mold filled in step-wise fashion to promote preferential fiber alignment
Stacked	PU-bonded	Pre-cast HSHDC layers (3 and 4 layer versions) with PU adhesive at interfaces
	PU-bonded Prestrained	Same as above with HSHDC strained uniaxially prior to interfacial bonding
	Hybrid	Pre-cast layers alternated with freshly cast layers, no interfacial material
Mesh	PP-mesh	HSHDC alternated with PP-mesh layers (3 and 5 mesh layer versions)
	VCP-mesh	HSHDC alternated with VCP-mesh layers (3 and 5 mesh layer versions)
	PP-mesh WD40	HSHDC alternated with PP-mesh layers (3) coated in mold release (WD40)

These physical models are used to determine the potential mechanical utility of nacre-inspired design features in cementitious material systems on a size scale much larger than that of natural nacre. To determine these effects, the nacre-inspired schemes are compared to the monolithic version of the same ECC material that serves as the primary component of all the nacre-inspired design schemes. The composite design schemes investigated herein are summarized in Table 4.2.

4.3.1 Monolithic control schemes

Two version of the monolithic control series are tested. The first is monolithic specimens formed via freshly mixed HSHDC material being poured into molds, similarly to how the material would be processed and shaped for real, large-scale applications.

The second version of the monolithic HSHDC control uses a more refined casting process in which molds are filled in a step-wise manner, such that the discontinuous fibers within the HSHDC are allowed to preferentially align in the planar orientation normal to mold filling direction. This creates fiber alignment (in a planar orientation, rather than unidirectional), without the formation of discrete layers like those intentionally created in the nacre-inspired schemes. This control series can help isolate the effect of intentionally weak interfaces within the nacre-inspired schemes from that of simple 2D fiber alignment

4.3.2 Stacked layering design schemes

This group of design schemes uses precast HSHDC layers (primary layers) stacked in a variety of manners and with a variety of interfacial secondary layers between. The orientation of these layers in the large, dog-bone shaped tensile specimens is illustrated in Fig. 4.5 (a).

The adhesive interface scheme uses a commercially-available, high strength polyurethane adhesive as an analog to the biopolymer interfacial layers within nacre. The biopolymer in nacre is characterized as (1) having extremely high strength of adhesion to the mineral tablets, (2) allowing sliding of tablets relative to each other while, and (3) maintaining ligamental attachment to tablets during sliding, providing mechanical resistance to continued sliding. This particular polyurethane adhesive was chosen using these criteria. A transverse cross section of this scheme, hereafter referred to as the “PU-bonded scheme”, is seen in Figure 4.5 (b).

A styrenic block copolymer exhibiting ligamental attachment in shear and tensile loading arrangements was also explored during preliminary testing, but did not perform as well as the polyurethane adhesive due to lower strength of adhesion to the cementitious material and limited resistance to layer sliding.

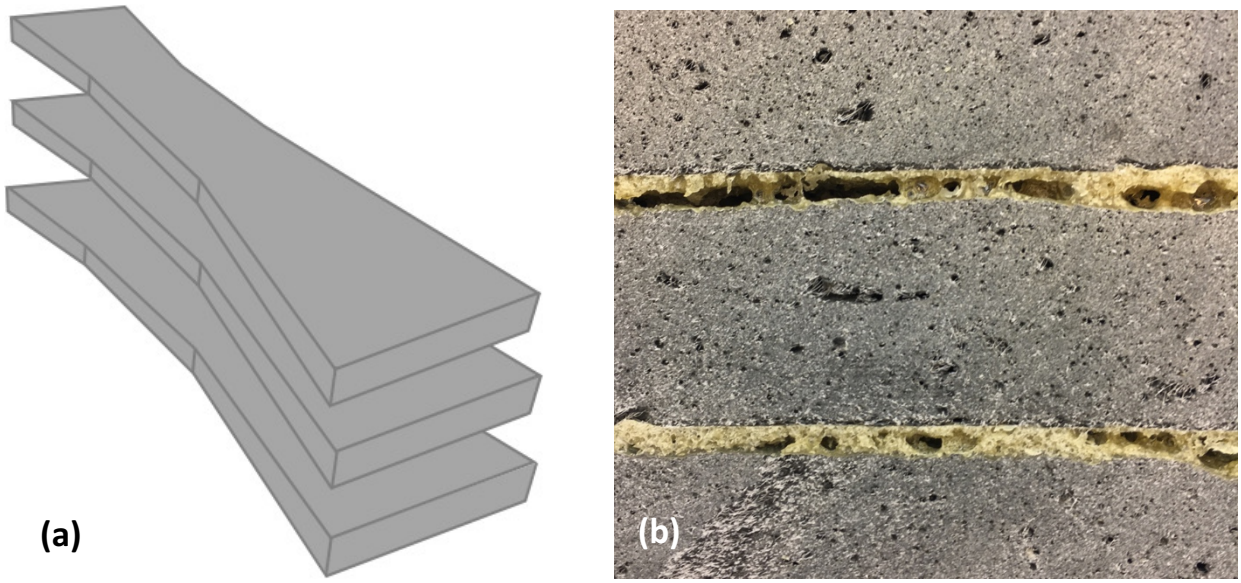

Figure 4.5: (a) An exploded view of the primary layer orientation used for the stacked layering schemes' ("PU-bonded" and "Hybrid") tensile specimens. In the PU-bonded scheme, as seen in transverse cross-section in (b), PU adhesive are applied at the interfaces between the primary layers, while additional layers of HSHDC material are cast between pre-cast layers in the Hybrid scheme.

Prestraining of the pre-cast layers, to generate discrete segments within the HSHDC material, prior to application of the PU adhesive is also investigated. This scheme, labeled as "Prestrained PU-bonded" is meant to more closely mirror the structure of nacre in that the segmented structure within each layer is present prior to the application of excessive loading. To produce these specimens, the primary layers, like those depicted in Figure 4.5(a), are individually subjected to uniaxial tension and bidirectional bending forces to generate well-distributed microcracking throughout. All cracks generated in the primary layers are oriented perpendicular to the eventual tensile loading direction in the large dogbone composite specimens. The degree of prestrain applied to each layer is kept below the average strain capacity of typical, high aspect

ratio (thin layer) HSHDC specimens (< 3%) After unloading, the layers are adhered together with the PU adhesive and a constant force is applied to promote the quality of bonding and mitigate the natural expansion of the PU bondlines, just as in the other PU-bonded schemes.

An additional stacking scheme, alternating precast layers with freshly cast layers with no additional interfacial component as described in Soltan et al. (2014) [22], was also investigated. In this scheme, referred to hereafter as the "Hybrid" scheme, the natural surface roughness on the precast layers contributes to an interfacial bond formed between the precast and cast-in-place layers, which is intentionally weak. With no fibers bridging across these interfaces within the composite, layers are allowed to deform independently under excessive loading after the initial bond is severed, hypothetically promoting crack arrest, energy dissipation, and compartmentalization of damage.

This Hybrid scheme was observed to have fewer internal voids at the interfaces than the PU-bonded stacked schemes. As seen in Figure 4.5(b), significant voids are present between stacked primary layers in the PU-bonding scheme due to non-flat surfaces of the pre-cast primary layers, as well as naturally occurring air entrapment in the foaming PU adhesive during curing.

The thickness of the primary layers in the stacked scheme specimens depends upon on the number of total cementitious layers in the scheme. The total thickness of the composite tensile specimens was kept at ~76mm regardless of scheme. The hybrid scheme includes four layers (two precast, two cast in place), and both 3 and 4 primary layer specimens were tested in tension for the PU bonded scheme.

4.3.3 Mesh layering design schemes

Polymer meshes were used as an alternate approach to create nacre-inspired structures and deformation mechanisms. In these schemes the secondary layers are polymer mesh materials, and they not only act as the interface between primary HSHDC layers, but they serve to distinguish and shape the primary layers during initial composite fabrication. During casting, mesh layers are alternated with cementitious material during mold filling to create a layered structure. Figure 4.6 illustrates the orientation of mesh layers (depicted in green) within the

dogbone shaped tensile specimens, aligning with the loading direction. The same orientation is used for the beam specimens, but in flexure, the loading direction is normal to the planar orientation of the mesh and HSHDC layers.

Two mesh materials are used in this investigation and the number of mesh layers is used as a variable. Regardless of number, the mesh secondary layers are spaced relatively evenly through the thickness of the composite, manipulating the thickness of the primary cementitious layers.

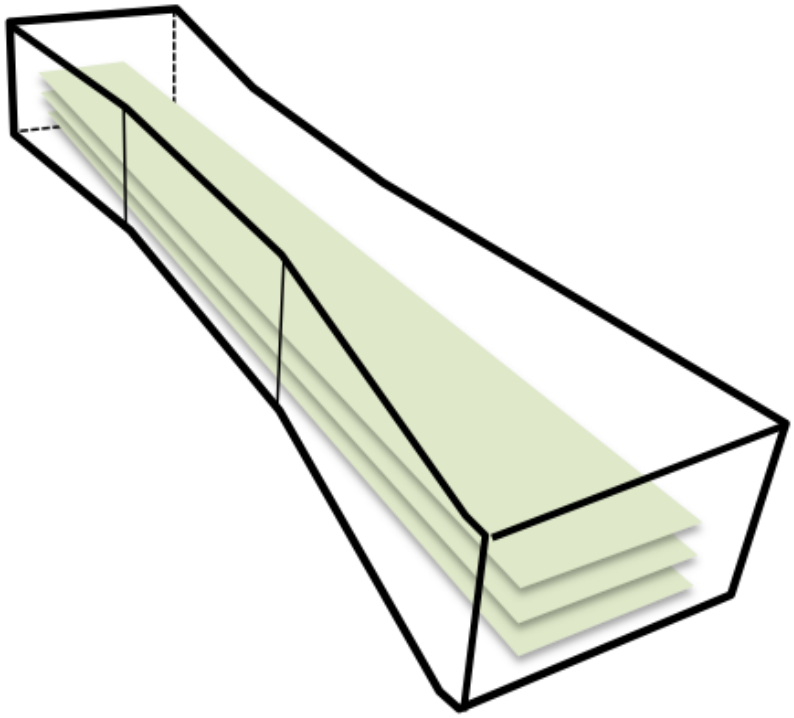

Figure 4.6: Illustration of the orientation of three mesh layers within tensile specimens tested in this study. The number of mesh layers, which also dictates the total number of layers, is used as a variable.

The alternating fiber-reinforced cementitious material and polymer meshes mimic nacre's structure in a number of ways. First, the meshes create distinct layers of cementitious material. The fibers within the cementitious material are generally confined to a single layer, creating intentionally weak interfaces between cementitious layers without fiber bridging, and strengthening each layer because of enhanced intra-layer fiber alignment. The meshes create pillars of cementitious material between cementitious layers (*through* the mesh apertures) due to the apertures in the mesh, creating a cohesive composite material and promoting initial elastic

stiffness in the composite. This “through-mesh” interlayer cementitious bonding is analogous to the mineral pillars observed in nacre that provide initial stiffness. Just as in nacre, these “pillars” are more susceptible to fracturing in shear and tension than the cementitious layers and are severed under extreme loading. After the pillars are severed under loading, the material remaining attached to each cementitious layer acts as a roughened surface (see Figure 4.7) to provide enhanced resistance to shearing/sliding between layers. Additionally, these mesh layers are cast into the composite so as to impart a wavy shape to the cementitious layers, while allowing contiguous layers to nest into each other (see Figure 4.8), just as in nacre. This waviness in nacre is thought to contribute to strain and shear-hardening behavior that enhances nacre’s toughness. By capturing the essence and hypothesized functionality of the interlayer mineral pillars, interfacial surface roughness, and wavy, nested shaping of the layers, all three of the mechanisms previously proposed to be responsible for nacre’s resistance to layer sliding are incorporated in the layered mesh approach [1,4,5,7,9,25,26,27].

Additional benefits of this mesh-based structuring approach were observed during mechanical testing and are discussed in Section 4.4.4.

Figure 4.7: Opposing faces exposed after layer debonding and sectioning of a VCP-mesh specimen. Interlayer mineral bridges are formed through the mesh apertures and subsequently severed during loading, leaving a marked surface roughness that may contribute a desired resistance to layer sliding. Interfaces in the PP-mesh scheme have a similar appearance, but with larger mesh apertures and thus larger interlayer mineral bridges.

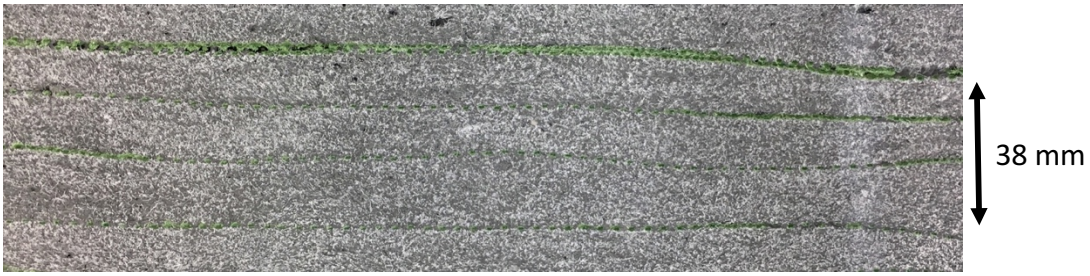

Figure 4.8: The waviness and nesting of HSHDC layers in the mesh layering schemes is illustrated. The waviness of the layers is inspired by a proposed mechanism in nacre that offers resistance to layer sliding, producing local shear-hardening and strain-hardening behavior, under excessive shear and tensile loads.

Previous research has shown advantages to using mesh reinforcement in concrete to enhance performance in flexure [28,29,30]. Peled and Bentur (2003) tested knitted and woven polymer fabrics within cementitious matrices and reported both improved and reduced performance in flexure, depending on the geometry of the fabric, in comparison to continuous fiber reinforcement [28]. Brückner et al. (2006) reported a strengthening effect in rectangular beams and T-shaped beams when multiple layers of woven glass fabrics were cast into the concrete [29]. Pakravan et al. (2011) saw enhanced ductility via displacement-hardening behavior (in flexure) when non-woven polypropylene fabric was added to a cementitious matrix, though the addition of many fabric layers caused a loss in flexural strength [30].

Effects of textile reinforcement or layering on cementitious composite performance in direct tension have not been as thoroughly reported, and are investigated in the present study. However, in the nacre-inspired schemes explored here, the primary aim of using the mesh materials is to create distinct layers and other nacre-inspired structural features within the composite, and any reinforcing effects are ancillary.

To determine the reinforcing contribution of the mesh to tensile and flexural performance, a scheme with purposefully weak interfaces is also tested. In this scheme, called “PP-mesh WD40”, mesh layers are coated in mold release (WD40) prior to being cast into the tensile and beam bending specimens. By discouraging bonding between the polymer mesh and the cementitious matrix, the contribution of the structuring allowed by the mesh, rather than the mesh as a reinforcement per se, can be shown more clearly. Similarly, the monolithic scheme

with aligned fibers is also meant to provide context to the performance of the layered mesh schemes regarding textile reinforcement contributions.

4.4 RESULTS AND DISCUSSION

Performance of the various schemes in tension, bending, and compression is presented and compared, followed by discussion of the effects of structuring features on deformation mechanisms, failure modes, and overall mechanical performance.

4.4.1 Performance in direct tension

The tensile strength and tensile strain capacities of each of the nacre-inspired composite design schemes are compared in Figure 4.9.

The relative parity amongst these tensile strength results indicate that composite tensile strength remains highly dependent on cementitious matrix strength and fiber bridging capacity, just as in unstructured (monolithic) ECC. The various nacre-inspired schemes do not appear to significantly alter ultimate strength at this size scale, with the exception of the prestrained PU-bonded scheme, which suffers reduced strength due to the damage accumulated in the HSHDC material during the prestraining process. Differences seen in tensile strength amongst the other schemes can be largely accounted for by natural matrix variation associated with processing. This would explain the curious tensile strength difference between the pour-casted and intentionally layered monolithic schemes, as well as the inconsistent differences between each of the 3 and 5-layer mesh schemes.

Tensile performance differences between the nacre-inspired schemes and the monolithic control case become clear when tensile strain capacity is compared. Nearly all nacre-inspired schemes showed significant improvement in tensile strain capacity over the pour-casted monolithic scheme. Improved strain capacity increases the amount of energy required to cause the material to fail, contributing to durability, but improvements in strain capacity that come at the expense of tensile strength or consistency in tensile performance would preclude use in some applications. Strength-governed design is more common than strain capacity-governed design in structural

applications. Therefore, it is important to evaluate tensile strength and tensile strain capacity in tandem, and also consider the consistency in performance.

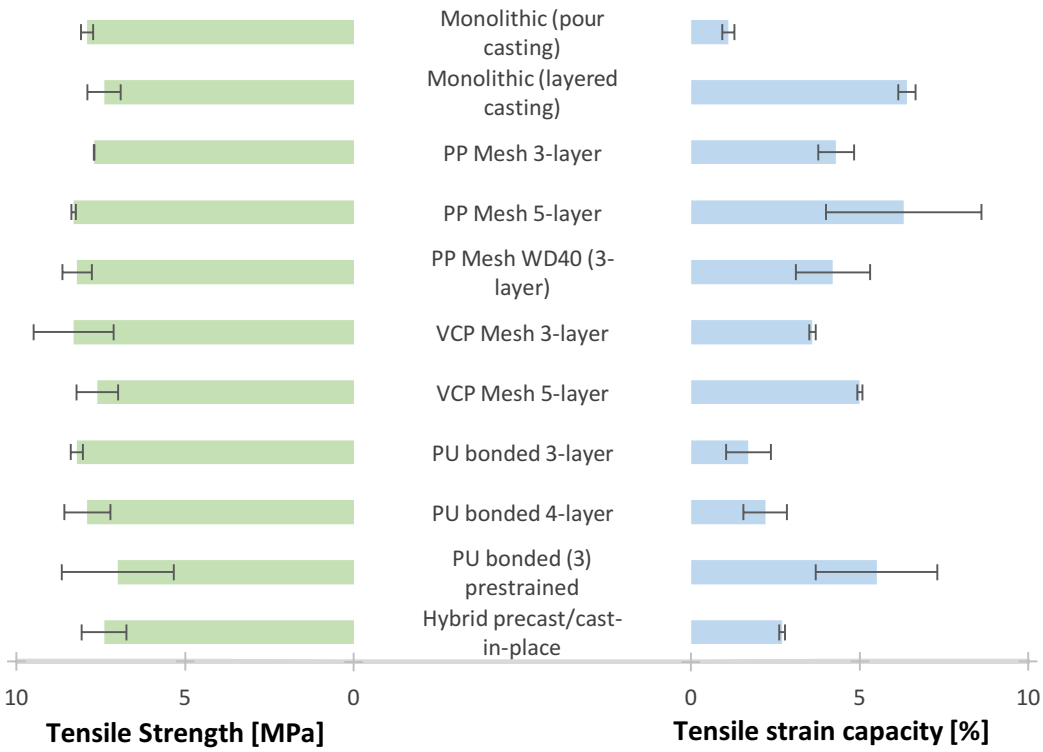

Figure 4.9: Tensile strength and tensile strain capacity of the nacre-inspired composite design schemes are compared

A general trend of improvement in strain capacity coming at the expense of tensile strength is observed (particularly apparent amongst the three PU-bonded schemes and two VCP mesh schemes). This trade-off between strength and strain capacity is common for SHCC materials, as discussed in Section 2.4.3, and can be attributed to the crack bridging capacity of fibers within the HSHDC material. At lower stresses, fibers can accommodate the stress associated with bridging a higher number of cracks, inflating strain capacity. When cracking in the cementitious matrix is suppressed until higher stresses, bridging capacity of the fibers is exhausted more quickly, resulting in fewer cracks and lower strain capacity.

The mesh layering schemes, in general exhibited a combination of significantly improved strain capacity, maintained tensile strength, and consistent performance that the PU-bonded schemes

could not match. The PP mesh schemes exhibited consistent tensile strength, while the VCP mesh schemes showed less consistent strength, but more consistent strain capacity.

The contribution of fiber alignment in all schemes is apparent from the significant improvement in tensile performance observed between the monolithic pour-casted and monolithic layered schemes. The monolithic layered scheme does not incorporate overtly distinct layers (and no evidence of layer debonding was observed), but does have a significantly higher degree of fiber alignment in the plane parallel to the tensile loading axis than the pour cast scheme. A similar degree of fiber alignment within HSHDC layers is generated from the mesh and stacked schemes and is certainly responsible for a portion of the improved strain capacity, if not a slight increase in strength due to enhanced strain-hardening.

An additional metric to compare in tension is the stress at which the elastic limit is reached, at which point inelastic deformation (generally microcracking) is initiated. The monolithic pour casted and layered casted schemes exhibited an average elastic limit at ~6 MPa and 4 MPa, respectively. The 3-layer PP-mesh schemes, both the regular version and the WD40 version, showed the highest elastic limit of the nacre-inspired schemes, at ~4.5 MPa, while the PU-bonded specimens showed reduced limit of ~3 MPa. The prestrained PU-bonded scheme showed the lowest elastic limit at ~2 MPa, precluding the scheme from structural applications.

The tensile performance of both the nacre-inspired schemes and monolithic schemes tested here can be compared to previous characterization done on the HSHDC material. Ranade et al. [23, 24] report an average tensile strength of 11.8 MPa and average tensile strain capacity of ~3.5% for HSHDC, however, this was using the Japanese Society of Civil Engineers (JSCE) recommended dogbone specimen. The geometry of the JSCE dogbone specimen promotes fiber alignment along the loading axis and minimizes the occurrence of natural casting flaws, inflating both strain capacity and ultimate tensile strength. The larger, square cross section of the large dogbone specimens used for tensile characterization here more accurately measures how cementitious material would perform in full-scale, structural applications using full-scale casting methods.

4.4.2 Performance in flexure

The advantages of the nacre-inspired structuring schemes are more apparent in flexure (Figure 4.10). All schemes tested, with the exception of the PU-bonded scheme, show at least a 30% increase in modulus of rupture over the pour-casted monolithic version. The PP-mesh schemes demonstrate the best performance in bending with an approximately 100% increase in modulus of rupture, in combination with a dramatic improvement (up to 6x) in inelastic flexural toughness, compared to the pour-casted monolithic case.

The improvement in flexure seen in the nacre-inspired schemes is not surprising when it is considered that natural nacre is specifically meant to lend flexural toughness to the shells in which it is found. The shells in which nacre is seen generally have an extremely hard outer mineral layer, while nacre coats the inside of the shell, primarily to protect against bending moments and through-cracking generated in the case of highly concentrated loads or impacts, as illustrated graphically in Fig. 4.11.

The nacre-inspired schemes tested here illustrate a range of performance profiles. The PP-mesh schemes demonstrate the combination of increases in both flexural strength and flexural toughness, while the PU-bonded scheme proves to be an option for prioritizing high energy absorption/dissipation over high strength. The relatively good performance of the layer casted monolithic scheme highlights a cost efficient route to improving SHCC performance and has implications for 3D printed SHCCs, which will have a naturally layered, but unified structure.

Previous characterization of the monolithic HSHDC material has measured a 30 MPa modulus of rupture, higher than that measured here and similar to what is measured here for the nacre-inspired design schemes [23]. Here we comparatively show a discernable improvement in modulus of rupture compared to two different monolithic HSHDC schemes, presumably due to the nacre-inspired structuring and mechanisms, as the HSHDC material used for every scheme is processed in a controlled, consistent manner. The discrepancy between the values of modulus of rupture of monolithic HSHDC reported here and reported previously is attributed to experimental and measurement sources of error. The discrepancy is not attributed to size effects due to the smaller beam cross section used in this study.

The hybrid pre-cast/cast-in-place scheme was previously tested in flexure, and showed improved inelastic flexural toughness compared to monolithic HSHDC [22]. However, in these previous tests, no significant improvements in modulus of rupture were observed in flexure for the hybrid scheme, unlike in the mesh schemes.

The weak interfaces in the PP-mesh WD40 (3-layer) scheme do not appear to negatively affect performance in flexure, indicating that the bond between the PP-mesh and the cementitious matrix is already inherently weak and does not play a significant role in composite performance.

The PP-mesh schemes outstrip the VCP schemes in flexure performance. This discrepancy is discussed in Section 4.4.4. With the cost of PP-mesh being relatively low compared to that of the VCP mesh, the PP-mesh schemes are the most promising of those tested in this study based on both tensile and flexural performance.

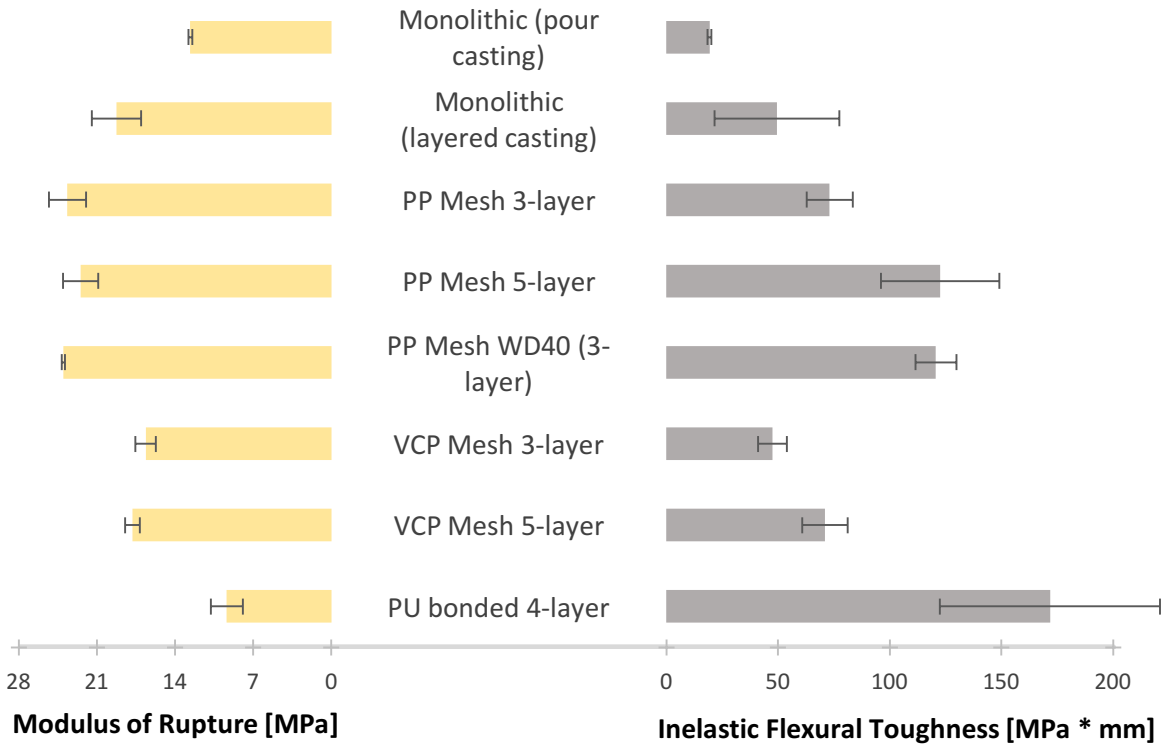

Figure 4.10: Modulus of rupture and inelastic flexural toughness are of various nacre-inspired composite design schemes are compared

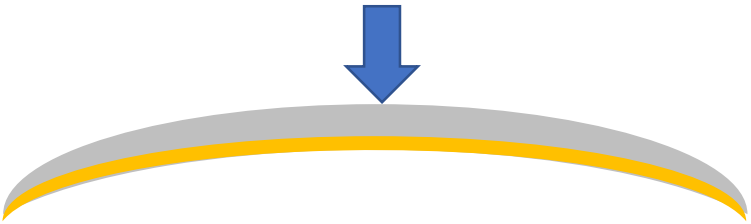

Figure 4.11: A schematic of a nacreous seashell and a typical loading condition from which natural nacre (represented in yellow) is designed to protect the animal living within. Nacre, present as a relatively thin layer on the interior of the shell, is designed to prevent through-cracking and provide material toughness when subjected to a bending moment such as that from a sharp object and/or concentrated impact to the outside of the shell.

Initial flexural stiffness (elastic) is also considered. The monolithic scheme exhibits the highest stiffness (24.4 MPa/mm), while the PU-bonded scheme (4 HSHDC layers) exhibits the lowest of the schemes tested in flexure (9.2 MPa/mm). Interestingly, the monolithic layered scheme exhibits a relatively intermediate average elastic stiffness of 16.3 MPa/mm. The PP-mesh WD40 scheme had the highest average initial elastic stiffness of the nacre-inspired schemes at 17.89 MPa/mm. Within each scheme, an increase in the number of total layers (primary + secondary) was generally correlated with a reduction in initial flexural stiffness.

4.4.3 Performance in compression

As the most promising nacre-inspired scheme in tension and flexure, the PP-mesh scheme is compared to monolithic HSHDC in compression. The PP-mesh composite scheme is tested in two orientations: with the mesh and HSHDC layers oriented normal to the loading axis and parallel to the loading axis. As seen in Figure 4.12, the PP-mesh scheme demonstrated consistently higher compressive strength, in both orientations, than the monolithic case.

The mesh component's contribution to improved performance in compression can probably be attributed to deformation mechanism manipulation. In tension the mesh layers may carry some tensile load, acting as "reinforcement", but in compression, the mesh would not be contributing to load carrying capacity. Instead, performance enhancement is likely a result of crack paths

within the HSHDC layers being altered by the mesh layers, dissipating energy and suppressing failure via layer debonding and crack bifurcation in both orientations.

This improvement in compressive performance is not necessarily expected as nacre has not been seen to exhibit higher compressive performance than bulk aragonite.

It should be noted that monolithic HSHDC has been previously reported to have an average compressive strength of ~160 MPa [23], similar to what is measured here for the PP-mesh scheme (normal orientation). Using the control series benchmark (monolithic series) from this study, however, it appears clear that the nacre-inspired schemes, designed to improve tensile and flexure performance, also offers a boost in compressive strength. Using specimens prepared as part of the same study provides a more direct method of comparison and eliminates other factors that may be the source of this quantitative discrepancy in performance.

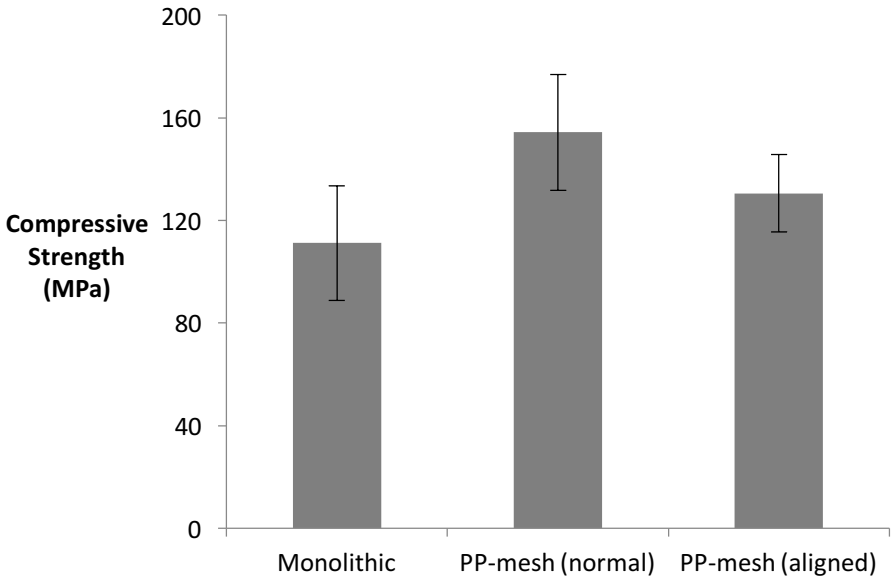

Figure 4.12: The performance in compression of the PP-mesh nacre-inspired scheme is compared with that of the monolithic HSHDC case at an age of 14 days

4.4.4 Effect of material structuring on deformation mechanisms, damage progression, and failure modes

Observation of cracking patterns and deformation progression suggests that nacre-inspired deformation mechanisms are being generated within the nacre-inspired composite schemes and may be associated with strain capacity and modulus of rupture improvements over the monolithic case.

Compartmentalization of Damage

One mechanism contributing to the nacre-inspired schemes' boost in tensile strain capacity, modulus of rupture, and inelastic flexural toughness appears to be the ability of the layered specimens to isolate an accumulation of damage within each primary layer, at least to a degree. The HSHDC material, upon which the various layering schemes are based, inherently suppresses failure by distributing damage throughout the material instead of allowing damage to localize at a single weak point. However, this material is only able distribute damage in one dimension (the length of the gage section of the tensile specimen or length of the span in flexure). The layered nacre-inspired hierarchical composites are able to distribute damage along the length of the gage/span section, but also between different primary layers, which, in some cases, are able to contain the damage without affecting other layers.

This compartmentalization of damage within layers is observed in every one of the nacre-inspired design schemes tested here, but through cracking behavior is not necessarily excluded. Compartmentalization is evident when cracks are arrested or caused to bifurcate at the mesh interlayer boundary. Based on the observed occurrence of crack arrest, it is an initial layer debonding at the secondary layer interface that promotes this compartmentalization. Several instances of layer debonding and crack arrest are seen in the longitudinal cross-sections of tensile specimens shown in Figure 4.13. In other instances, also seen in Fig. 4.13, cracks appear to be contained, not within one layer, but within two or three adjacent layers. This behavior is similar to process zones that appear in nacre under extreme loading, as seen in Wang et al., (2001) and Kakisawa and Sumitomo, (2012) [4,5]. The appearance of the longitudinal cross sections of the PP-mesh and VCP specimens in Fig. 4.13 can be compared to that of the monolithic specimen pictured in Fig. 4.14, which shows a much higher degree of through cracking.

In addition to the observed instances of crack arrest between primary layers, compartmentalization of damage within layers in the PP-mesh scheme is also indicated by the cracking observed parallel to the loading direction. In Figure 4.15, a progression of damage accumulation in a single specimen shows multiple longitudinal cracks developing parallel to the loading direction (up and down, as pictured). These cracks correspond to the locations of PP-mesh interlayers within the specimen and indicate that shear stress is occurring at the interlayer boundaries as damage accumulates in each layer at different rates.

In the PP-mesh scheme, fewer layers are employed than in nacre due to processing and cost constraints, but the principal is preserved: multiple layers allow damage to not only be distributed, but also compartmentalized, to a higher degree than a monolithic case, contributing to the improved macroscopic performance.

(a)

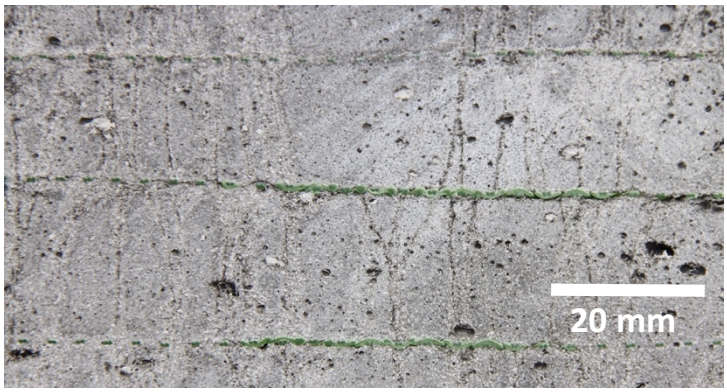

(b)

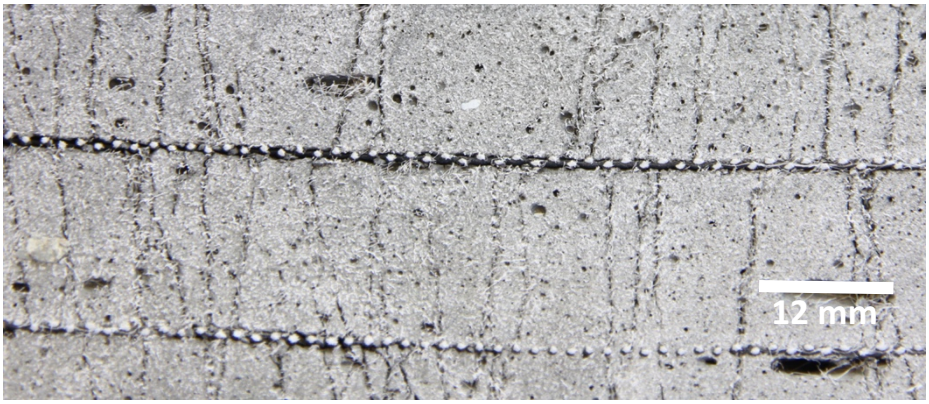

(c)

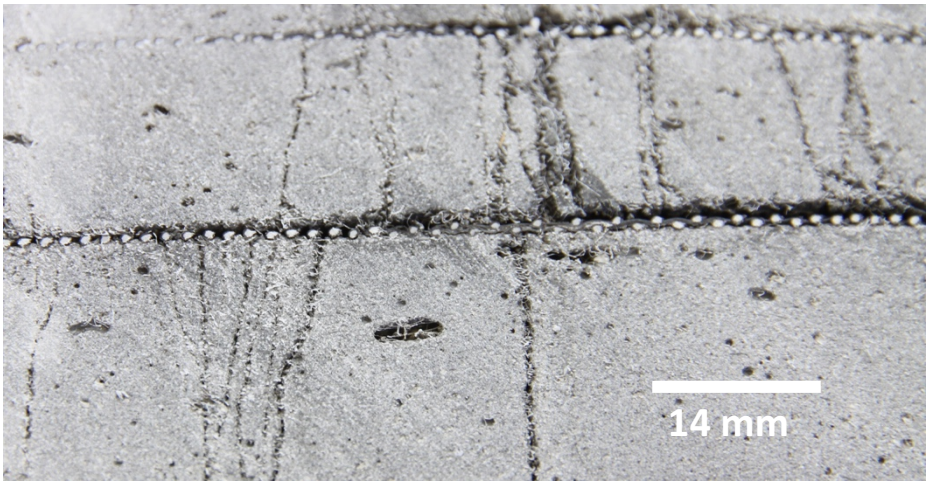

Figure 4.13: Longitudinal cross sections of the PP-mesh (a) and VCP-mesh (b and c) layering schemes tested in direct tension, showing the containment of damage (cracking) either within a layer or within several adjacent layers

Figure 4.14: A longitudinal cross section of a monolithic scheme tensile specimen showing a high degree of complete through-cracking.

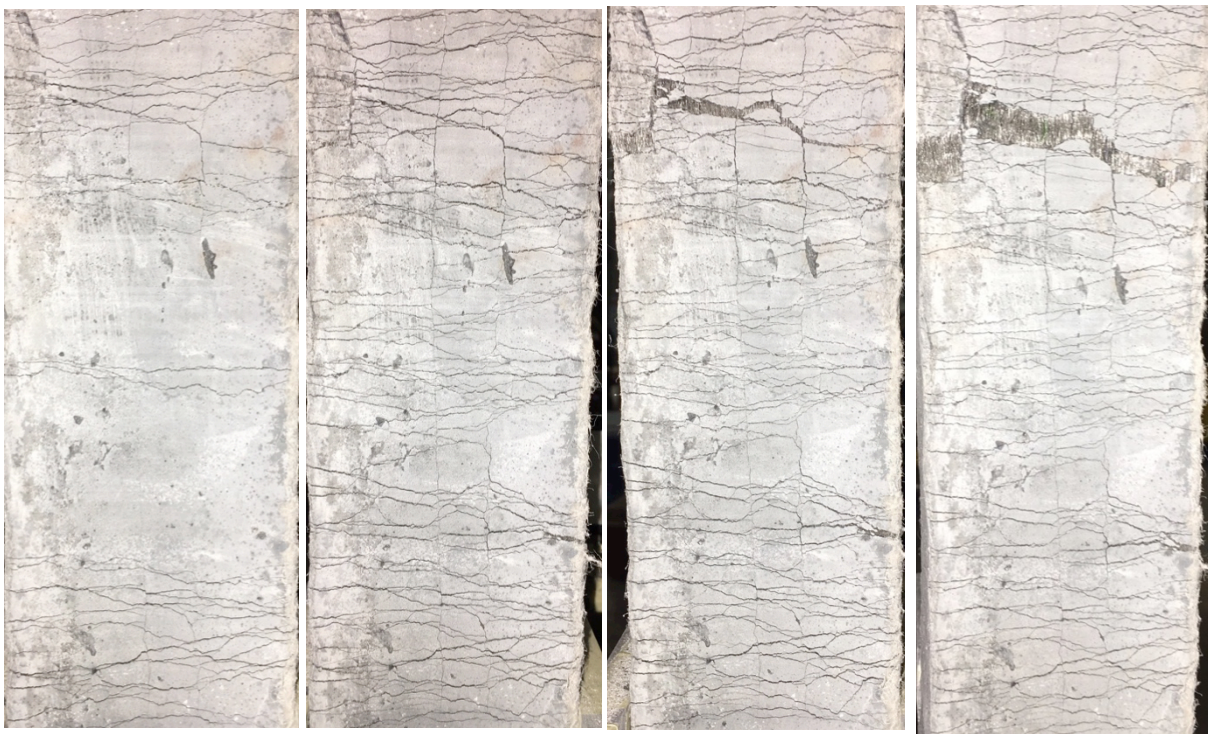

Figure 4.15: Progression of damage (from left to right) in a PP-mesh tensile specimen, showing the development of several longitudinal cracks, parallel to the loading direction (vertical), corresponding with locations of PP-mesh within the specimen. (Scale: the specimen pictured has a horizontal width of ~76 mm)

Layer sliding and resistance to sliding

The vertical cracks and large failure crack seen in the last image of the progression shown in Figure 4.15, show evidence of layer sliding, related to the accumulation of damage within each layer at different rates. The left most layer (as pictured in Fig. 4.15) has slid significantly relative to the adjacent layer near the location of failure. It is seen that the failure crack has a tortuous path, influenced by the layering scheme.

Layer sliding is part of a deformation mechanism in nacre that generates local slip-hardening, and macroscale damage distribution, strain-hardening, tensile ductility, and enhanced material toughness. The microcracks generated within each of the primary HSHDC layers are analogous to the “activation sites” produced in nacre when tablets slide relative to those adjacent. Each of these features, microcracking and tablet activation, provides a “give” within the material and are

spread throughout the material instead of localizing. To generate the necessary slip-hardening behavior, however, there must be some interlayer resistance to sliding, once it has been initiated.

Intralayer resistance is provided in part by the fibers bridging the microcracks within each layer, analogous to the organic bridging in nacre, described in Figure 4.4 (a) and (c). Of course, in nacre tablets are pre-defined via the growth process, and in the PP-mesh scheme, the discrete units are generated under loading via microcracks. However, the activation of these sites, resistance to continued sliding, and distribution of damage occur in similar ways in both nacre and the PP-mesh nacre-inspired scheme.

Additional interlayer resistance to sliding is also required to suppress intralayer failure as stress continues to build. In the mesh schemes, the layer waviness and surface roughness left by the severed mineral pillars was hypothesized to contribute to interlayer sliding resistance, but why do the PP-mesh schemes outperform the VCP-mesh schemes in flexure, where layer debonding and sliding occur more readily? The answer could be the small number of polymer fibers that pass through the PP-mesh and connect adjacent layers through the mineral pillars formed in the mesh apertures, as pictures in several PP-mesh specimens in Figure 4.16. These exposed fibers, indicating evidence of fiber pullout, are not seen in the VCP-mesh specimens, presumably because of the smaller aperture size.

The relative sparsity of these interlayer fibers compared to those available for intralayer crack bridging, as observed in the PP-mesh schemes, means that the interlayer bridging strength is relatively low, but the force required for pullout of these fibers still contributes resistance to layer sliding after the mineral pillars have been severed. These limited but consistently observed interlayer fibers serve a similar role to the interfacial biopolymer component in nacre, providing ligamental adhesion between layers and resistance to layer sliding.

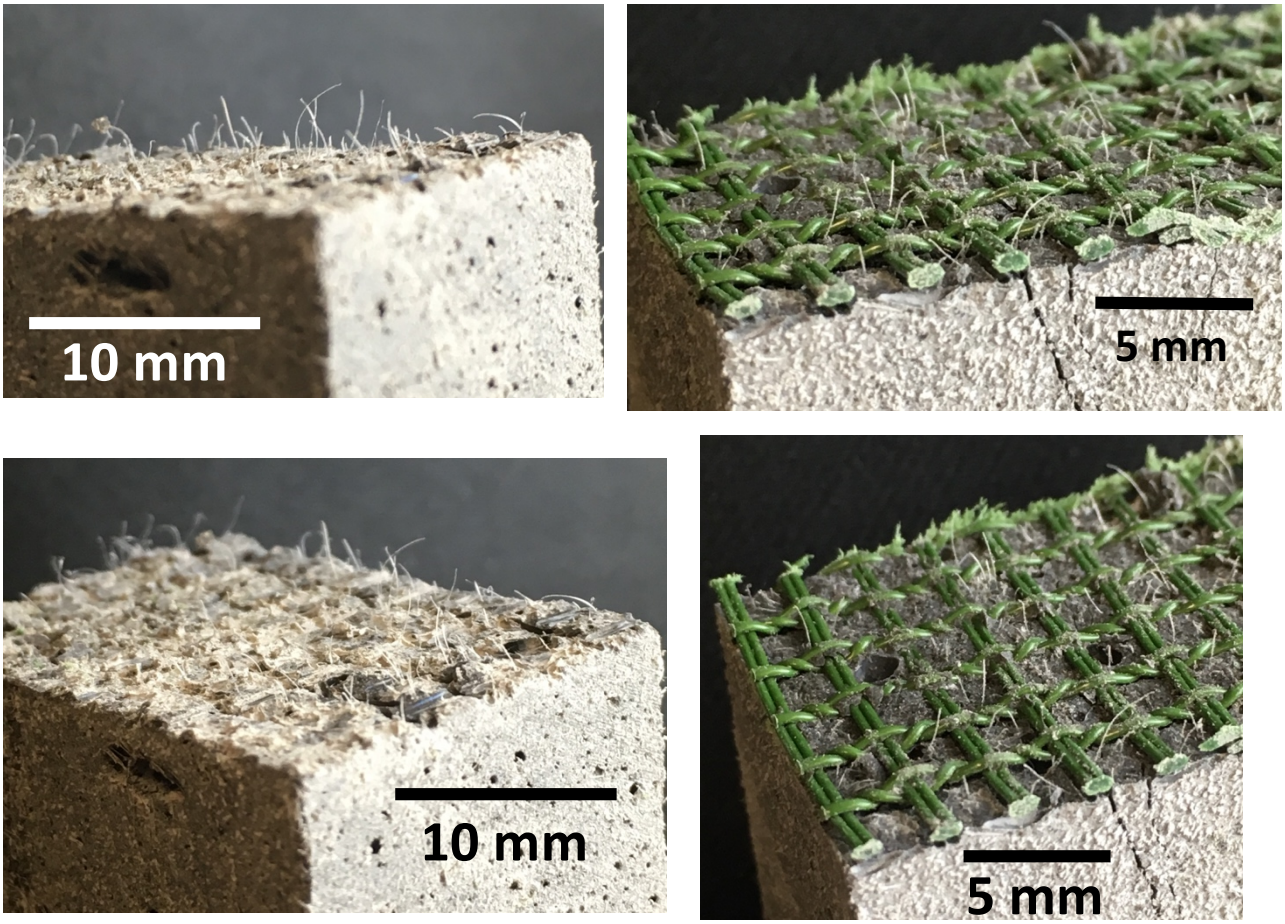

Figure 4.16: Interlayer fibers are observed in the PP-mesh schemes when layers debonded during testing are sectioned and the interfacial surfaces are exposed. Interlayer fibers were not observed in the VCP-mesh (Figure 4.7) scheme, nor in other nacre-inspired schemes.

The absence of interlayer fibers in the VCP specimens (Figure 4.7), due to the smaller mesh aperture size, may be the reason the PP-mesh scheme outperforms the VCP schemes in flexure. The sliding distances between layers are greater in flexure than in direct tension, meaning the effect of the resistance to layer sliding is more pronounced between schemes. Despite layer delamination (and associated crack arrest and bifurcation) being observed with more consistency in VCP-mesh schemes than in the PP-mesh schemes, flexural performance of the VCP-mesh schemes lagged behind that of the PP-mesh schemes. While simply generating layer delamination in the composite offers benefits over the monolithic case, the importance of generating subsequent resistance to layer sliding is highlighted. The superior performance of the

PP-mesh scheme suggests that the interlayer polymer fibers, playing the role of nacre's interfacial biopolymer, likely provide more effective sliding resistance than layer waviness and surface roughness in the large-scale, nacre-inspired composite schemes.

Layer sliding resistance is also observed in the PU-bonded schemes, as evidenced by elongated appearance of the adhesive remaining attached to either side of the HSHDC layer interface (Figure 4.17). Friction generated between the rough, adhesive covered surfaces remaining after the strength or strain limit of the adhesive has been reached, likely also contributes in flexure where sliding distances are larger. Significant layer sliding distances (up to 5mm) are observed in the PU-bonded bending specimens, which showed the largest deflections prior to failure, but inferior modulus of rupture to the monolithic case in flexure.

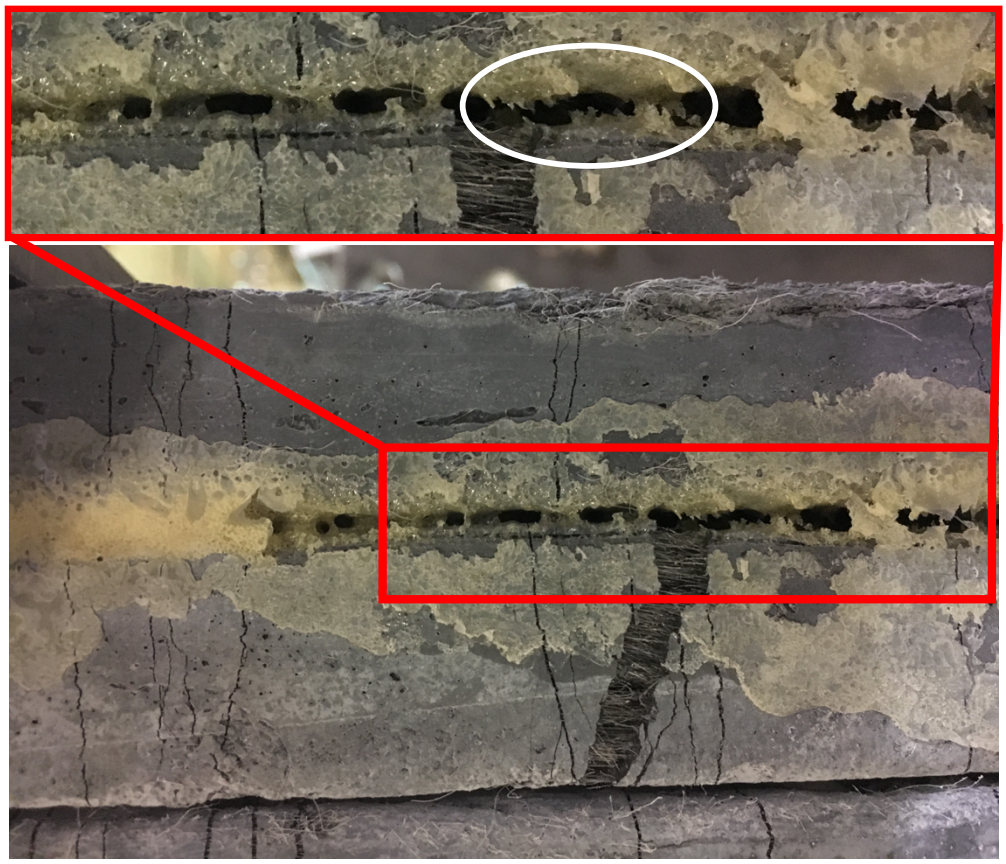

Figure 4.17: An example of the elongation of the remaining interfacial adhesive (circled), in an area of a prestrained PU-bonded tensile specimen where layer sliding has taken place, suggesting a degree of HSHDC layer sliding resistance provided by the adhesive. Similar observations were made in other locations in the prestrained PU-bonded specimens.

The sliding resistance provided by the PU adhesive, and the sequence of forces are applied to the adhesive, may explain the significantly higher strain capacity of the prestrained PU-bonded scheme in direct tension compared to the other PU-bonded schemes. In the normal PU-bonded schemes, the sudden appearance of cracks at the high stresses carried by the HSHDC matrix (and bridging fibers) cause a high rate of shear loading upon the adhesive material, perhaps debonding locally around cracks suddenly, without contributing to load carrying capacity. In the prestrained PU-bonded schemes, the profile of loading upon the adhesive material is different. Because the HSHDC layers are already cracked at intervals along the gage section, tensile strain initially occurs at lower stresses and at a much more gradual, controlled rate. This allows the adhesive material, as shear forces are applied to it, to share some of the load as HSHDC layers strain at slightly different rates. Cohesive debonding in the adhesive occurs only after it has substantially contributed to layer sliding resistance. Frictional resistance may even contribute after this limit has been reached. In this way, a larger strain can be reached prior to the exhaustion of the strength limit of the HSHDC, even though that strength limit may have been reduced due to the damage caused by prestraining.

While many of the schemes show layer sliding, and the requisite resistance to said sliding, comparing the overall mechanical performance of the various schemes, it is easy to pick the PP-mesh schemes as the most effective in applying nacre-inspired deformation mechanisms to enhance composite performance.

Progressive failure

All of the nacre-inspired schemes, in both tension and flexure, exhibit progressive failure: the sequential failure of single layers, while other layers preserve high stress carrying capacity, rather than total specimen failure. Even though through cracking is observed in many instances in the nacre-inspired schemes, “through failure” is prevented in every case.

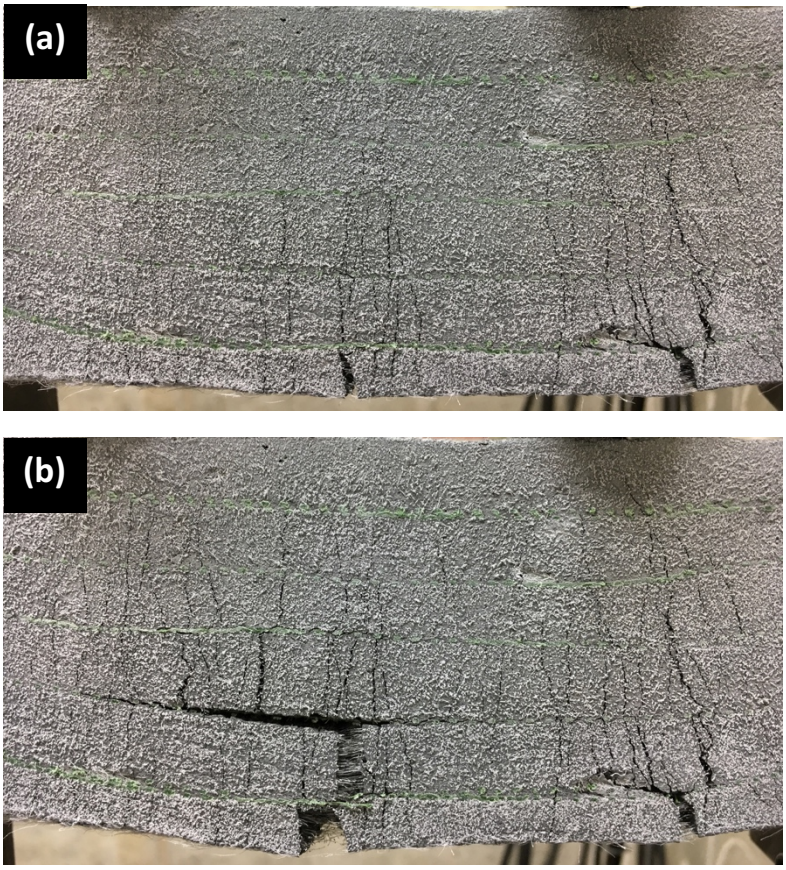

Figure 4.18: An example of the progressive failure behavior is seen in the PP-mesh scheme under flexure. In (a) the bottom layer has failed while the remaining five layers carry the flexural stress. In (b) the new "effective bottom layer" (second from bottom) has failed, while the remaining four retain load carrying capacity. The significant damage accumulated in the most tensile (bottom) layers is isolated from the upper layers, suppressing total failure of load carrying capacity.

Failure of any one of the layers, typically due to the exhaustion of crack bridging capacity of fibers across one of the cracks, often represents the end of composite scale strain-hardening simply because there is a reduced amount of material by which stress can be carried. However, the composite retains significant load carrying capacity as the significant damage accumulated by the failed layer has been compartmentalized and isolated from the other layers. An example of this behavior occurring in the PP-mesh bending specimens is illustrated in the sequence of images in Figure 4.18. Similar occurrences were seen in every nacre-inspired scheme. While other layers have also accumulated damage to accommodate the strain levels required to cause the first layer to complete the fiber pullout/rupture process, they have been shielded from whatever weakness caused the loss of load carrying capacity in the failed layer. In this way, the

composite can maintain a stress carrying capacity relatively close to its ultimate strength, even after significant damage has been accumulated and terminal stress decay has begun. This enhances composite toughness and provides a fail-safe mechanism. Such behavior is well suited to the critical applications in which a nacre-inspired cementitious building material could be justifiably deployed.

4.4.5 Continued Development

While advantages of using nacre-inspired features and deformation mechanisms have been shown, continued development needs to address durability of such composite schemes in a variety of environmental conditions and under cyclic loading conditions.

Additionally, alternate routes to producing nacre-inspired features and deformation mechanisms remain to be explored. The layered structure of nacre is a natural fit for fabrication processing via the large-scale 3D printing techniques currently being pioneered for automated, additive manufacturing of full-scale structures. Similarly, the benefits of layered strain-hardening cementitious composites reported here, and previously in Soltan et al. (2014), have advantageous implications for structural members 3D printed using strain-hardening cementitious composite material [22].

4.5 CONCLUSIONS

Approaches to adapting features and associated deformation mechanisms of nacre to a larger size scale and in materials applicable to civil infrastructure have been investigated. Various nacre-inspired hierarchical composite designs, based on strain-hardening cementitious composites, are evaluated in direct tension and flexure. The following conclusions can be drawn from this work:

The nacre-inspired composite design schemes tested herein, adapted to a much larger size scale than that of nacre, can provide strain-hardening cementitious composites comparatively enhanced modulus of rupture (stress carrying capacity) and significantly improved inelastic flexural toughness in flexure compared to the monolithic cases. While only one version of ECC was used for testing of the nacre-inspired schemes, it is expected that similar improvements

would be seen in other varieties of ECC when the most successful of these nacre-inspired schemes are applied. Absolute values of modulus of rupture, inelastic flexural toughness, and deflection, as well as percentage increase in these metrics compared to the monolithic case, will depend on the type of SHCC material used as the primary component.

In direct tension, significant benefits are seen for tensile strain capacity, but any improvements in tensile strength are small, and in several of the nacre-inspired composite schemes improvements in strain capacity come at the expense of tensile strength. Again, values of tensile strength, tensile modulus, and tensile strain capacity will depend on the type of SHCC to which these nacre-inspired design schemes are applied.

Both the "stacked layer" and "mesh layer" schemes show improvements in mechanical performance; however, the mesh schemes provide more consistent performance and property profiles better suited structural applications in which strength is prioritized over capacity for deformation prior to failure.

Of the schemes tested in this study, the mesh schemes incorporating polypropylene (PP) mesh, with aperture size of 6.25 mm^2, provide the best overall mechanical property benefits and outperforming other mesh schemes with smaller aperture sizes. While all the mesh schemes incorporated distinct layers, interlayer mineral pillars, interfacial surface roughness (after pillar fracture), and nested waviness (all features inspired by nacre's structure), the interlayer fibers allowed by the larger mesh apertures in the PP mesh appeared to provide the most effective resistance to layer sliding, resulting in the best performance in flexure, where layer sliding is most pronounced. The interlayer fibers, in the PP-mesh schemes behave as an analog to the interfacial biopolymer in natural nacre, providing ligamental adhesion between layers and allowing controlled sliding (shear) between primary layers.

In addition to enhanced tensile strain capacity, tensile strength, modulus of rupture, and inelastic flexural toughness, the PP-mesh scheme also exhibited enhanced compressive strength compared to the monolithic form of its primary material, HSHDC. This enhanced compressive performance of the hierarchical composite over the primary component is not observed in natural nacre.

Layer debonding is observed in all the nacre-inspired schemes tested in this study and contributes to compartmentalization of damage. Layer debonding, itself an energy dissipation mode, gives rise to crack arrest and crack bifurcation, which also contribute to fracture suppression.

Progressive failure, in which total composite failure is suppressed by virtue of intralayer compartmentalization of damage, provides a failsafe feature to all nacre-inspired design schemes presented here. This feature is particularly applicable to the critical use cases—such as seismic, impact, and blast resistance—in which enhanced strength, strain capacity, and toughness of cementitious materials already offer a value proposition.

Overall, the bio-inspiration from nacre, as adapted and evaluated here, does not provide the dramatic, holistic increase in mechanical properties observed in nacre compared to bulk aragonite. Conspicuously absent in these results is a notable improvement in tensile strength provided by the hierarchical structuring. The effects of the nacre-inspired structuring at this large, civil infrastructure relevant size scale are more subtle, though discernable mechanical advantages are seen, particularly in tensile strain capacity, modulus of rupture, and inelastic flexural toughness. These improved mechanical performance metrics are not as important for the design of civil infrastructure as strength, however, they can provide valuable performance enhancement in critical applications in which extreme, service disrupting loading is probable and high energy dissipation and failure mitigation are required.

References
(Chapter IV)

[1] Barthelat, F. H. Tang, P.D. Zavattieri, C.-M. Li and H.D. Espinosa, "On The Mechanics Of Mother-Of-Pearl: A Key Feature In The Material Hierarchical Structure," J. Mech. Phys. Solids. 55 (2), 306-337, 2007.

[2] Barthelat, F., J. Rim, and H.D. Espinosa, "A Review on the Structure and Mechanical Properties of Mollusk Shells - Perspectives on Synthetic Biomimetic Materials," Appl. Scanning Probe Methods XIII. B. Bhushan and H. Fuchs Eds. Springer, 1059-1100, 2009

[3] Davidson, M.S. "Towards an Understanding of the Role of Aragonite in the Mechanical Properties of Nacre." PhD diss., Harvey Mudd College, 2009.

[4] Kakisawa, H. and T. Sumitomo, "The Toughening Mechanism Of Nacre And Structural Materials Inspired By Nacre" Sci. Technol. Adv. Mater. 12 (6) 064710, 2011.

[5] Wang, R.Z., Z. Suo, A.G. Evans, N. Yao, I.A. Aksay, "Deformation Mechanisms in Nacre," J. Mater. Res, 16 (9), 2488-2493, 2001.

[6] Barthelat, F. and H.D. Espinosa, "An Experimental Investigation of Deformation and Fracture of Nacre-Mother of Pearl," Exp. Mech. 47 (3), 311-324, 2007.

[7] Meyers, M., P. Chen, A. Lin, and Y. Seki, "Biological Materials: Structure and Mechanical Properties." Prog. Mater. Sci. 53 (1), 1-206, 2008.

[8] Jackson, A.P., J.F. Vincent, and R.M. Turner, The mechanical design of nacre, Proc R Soc London B, 234, pp. 415-440, 1988.

[9] Evans, A., Z. Suo, R.Z. Wang, I.A. Aksay, M.Y. He, J.W. Hutchinson,"Model For the robust mechanical behavior of nacre" J. Mater. Res., 16(9), 2001.

[10] Wegst, U.G. K., H. Bai, E. Saiz, A.P. Tomsia, and R.O. Ritchie, Bioinspired structural materials, Nat. Mater., 14, 23–36, 2015.

[11] Barthelat, F., Biomimetics for next generation materials, Phil. Trans. R. Soc. A, 365, 2907–2919, 2007.

[12] Podsiadlo, P., S. Paternel, J.M. Rouillard, Z. Zhang, J. Lee, J.W. Lee, E. Gulari, and N.A. Kotov, "Layer-by-Layer Assembly of Nacre-like Nanostructured Composites with Antimicrobial Properties," Langmuir, 21, 11915-11921, 2005.

[13] Hunger, P.M., A.E. Donius, U.G.K. Wegst, "Platelets Self-Assemble into Porous Nacre during Freeze Casting," J. Mech. Behav. of Biomed. Mater., 2012.

[14] Finnemore, A., P. Cunha, T. Shean, S. Vignolini, S. Guldin, M. Oyen, and U. Steiner, "Biomimetic Layer-by-Layer Assembly of Artificial Nacre," Nat. Commun., DOI: 10.1038/ncomms1970, 2012.

[15] Rim, J.E., P.D. Zavattieri, A. Juster, H.D. Espinosa, "Dimensional Analysis And Parametric Studies For Designing Artificial Nacre", J. of the Mech. Behav. of Biomed Mater., 4(2), pp. 190-211, 2011.

[16] Espinosa, H., A. Juster, F. Latourte, D. Gregoire, O. Loh, P. Zavattieri, "Tablet-Level Origin of Toughening in Abalone Shells and Translation to Synthetic Composite Materials", Nat. Commun., 2, 173, 2011.

[17] American Society of Civil Engineers. 2017 Report Card for America's Infrastructure, http://www.infrastructurereportcard.org/, July 31, 2017.

[18] V.C. Li, On Engineered Cementitious Composites (ECC): A Review of the Material and Its Applications, J. of Adv. Concr. Technol., Vol. 1, No. 3, 215-230, November 2003.

[19] Chandler, R.F. “Life-Cycle Cost Model for Evaluating the Sustainability of Bridge Decks: A Comparison of Conventional Concrete Joints and Engineered Cementitious Composite Link Slabs.” A report of the Center of Sustainable Systems, University of Michigan, 2004.

[20] Li, V.C., and E. Herbert, “Robust Self-Healing Concrete for Sustainable Infrastructure,” J. Adv. Concr. Technol., 10:207-218, 2012.

[21] Şahmarana, M. and V.C. Li, Durability of mechanically loaded engineered cementitious composites under highly alkaline environments, Cem. and Concr. Compos., Volume 30, Issue 2, pp. 72-8, February 2008.

[22] Soltan, D.G.; Ranade, R.; Li, V.C.; "A Bio-inspired Cementitious Composite for High Energy Absorption in Infrastructural Applications", Proc. of the 13th Int. Symp. Multiscale, Multifunctional and Funct. Graded Mater., Blucher Material Science Proceedings, v.1, n.1, p. 1-4. São Paulo: Blucher, 2014.

[23] Ranade, R. , V.C. Li, M.D. Stults, W.F. Heard, and T.S. Rushing, Composite Properties of High-Strength, High-Ductility Concrete, ACI Mater. J., Vol. 110, Issue 4, pp. 413-422, 2013.

[24] Ranade, R., M.D. Stults, V.C. Li, T.S. Rushing, J. Roth, and W.F. Heard, Development of a high strength high ductility concrete, Proc. 2nd Int. RILEM conf. strain hardening cementitious composites, Rio De Janiero, Brazil, 12-14 Dec. 2011.

[25] Barthelat, F., C.M. Li, C. Comi, & H. Espinosa, Mechanical properties of nacre constituents and their impact on mechanical performance. J.Mater. Res., 21(8), 1977-1986, 2006.

[26] Song, F., A.K. Soh, and Y.L. Bai, Structural and mechanical properties of the organic matrix layers of nacre, Biomater. Vol. 24, Iss. 20, Pages 3623-3631, September 2003.

[27] K.S. Katti, D.R. Katti, S. M. Pradhan, A. P. Bhosle, Platelet interlocks are the key to toughness and strength in nacre, J. Mater. Res. 20 (5) 1097-1100, 2005.

[28] Peled, A. and A. Bentur, Fabric structure and its reinforcing efficiency in textile reinforced cement composites, Comp.: Part A 34, pp. 107–118, 2003.

[29] Brückner, A., Ortlepp, R. & Curbach, M., Textile reinforced concrete for strengthening in bending and shear, Mater. Struct. 39: 741, 2006.

[30] Pakravan, H., M. Jamshidi, M. Latifi, and M. Neshastehriz, Application of polypropylene nonwoven fabrics for cement composites reinforcement, Asian J. Civ. Eng. (Building and Housing), Vol. 12, No. 5, pp 551-562, 2011.

Chapter V

CLOSING

5.1 CONCLUDING REMARKS

5.1.1 Research Overview

This research has covered three materials design and development projects related to novel routes to material greening, processing methods, or bio-inspired hierarchical structuring of Engineered Cementitious Composites. Each project has resulted in novel varieties of functional ECCs and effective design strategies to guide additional or continued material development.

A variety of ECC using only natural, renewable plant fibers as fiber reinforcement to generate robust tensile strain-hardening behavior in a cementitious material has been developed. Compositional and processing strategies to overcome the challenges of using short, natural plant fibers within brittle cementitious matrices have been investigated and reported. Thermal characterization, lightweightedness, and limited strength of these curauá-reinforced ECCs point to specific construction applications.

A version of ECC compatible in principle with building-scale 3D printing processes has also been designed and developed. A general approach to promote printability in cementitious composites, leveraging thixotropy, was presented, and compositional ingredients and processing parameters were investigated for their effect on fresh state rheological behaviors related to printability. These parametric studies were performed and reported to guide both proof-of-concept material development, and continued printable cementitious composite development. Mechanical properties, both inherent and as a result of the material structuring resulting from printing processes, of the proof-of-concept “printable” ECC materials were characterized, and strain-hardening and distributed microcracking behavior was confirmed.

Bioinspired hierarchical composite design schemes, as inspired by nacre, were also designed and evaluated for mechanical enhancement of SHCC material. The effect of nacre-inspired structuring, enabled by the characteristic tensile behavior of ECCs, was seen to provide mechanical performance advantages on a size scale and in materials relevant for full-scale construction, though these advantages were primarily in flexure and tensile strain capacity, rather than tensile strength. Energy dissipation deformation mechanisms were observed that could offer utility in critical applications designed for extreme loading, or to improve the mechanical property profile of SHCCs limited by compositional, processing, or cost factors.

5.1.2 Research Impacts and Implications

Each of the three varieties of ECC designed and developed through this research offer feasible application and value propositions for real-world use cases. The design strategies investigated and reported can also be used for continued development of these and other cementitious composites. The projects are unified by their role in making the durability and resilience benefits of ECC accessible to new infrastructure applications and improving the benefits ECC can offer in others.

Thermal characterization, lightweightedness, and limited strength of the curauá-reinforced ECCs points to façade and building cladding applications in construction. These natural plant fiber reinforced composites offer a more eco-friendly alternative to traditional, synthetic polymer-reinforced ECCs in these applications. Depending on the market economics, Curauá-ECCs could also offer cost-saving, particularly for construction in the regions these fibers are cultivated, where the difference in fiber cost would be most significant. The demonstration of curauá in versatile construction materials like ECC can also serve to boost the curauá fiber market in these regions as the fiber is more widely recognized for utility in engineering applications.

Observation of the failure surfaces of the most robustly strain-hardening curauá-reinforced ECCs reported here indicate a fiber pullout failure mode, suggesting that further strength improvement can be made via enhancement of the fiber-matrix bonding. An improvement in composite strength can expand the range of appropriate applications.

The development of ECC materials compatible with building-scale 3d printing processes represents several significant outcomes. First, it positions ECC materials to be used in a method of construction that is currently receiving significant attention from the construction industry and the public alike, and is likely to be prominent method of construction in the future. Secondly, the advantages that ECC materials can provide to the building-scale 3D printing industry could potentially redefine the whole process. The robust tensile performance and "self-reinforced" nature of ECCs eliminates or reduces the need for ancillary reinforcement currently used in such processes, expands the design freedoms that the 3DP process offers to the construction industry, and can improve the durability and resilience of large-scale printed members and structures. The design and approach to printability of these printable ECC materials is meant to be widely applicable to the various hardware solutions that have already been developed for building-scale printing. The printable ECC materials produced and tested in this work represent a proof-of-concept that can be tailored to individual processing systems and/or applications. This work, in addition to previous ECC material design work, can inform the future development of a range of printable ECC materials with varying cost and performance.

The nacre-inspired hierarchical composite design project introduced several approaches to enhance the mechanical performance of SHCC materials, and for the first time explored nacre-inspired design for civil engineering applications. While the effect of such nacre-inspired structuring and deformation mechanisms was not seen to be as significant as at the size scale of natural nacre, mechanical performance benefits, particularly in flexure, were observed. Several of these hierarchical composite design schemes demonstrated energy dissipation deformation mechanisms that may be exploited in critical infrastructure applications to mitigate consequences of extreme loading more effectively than monolithic SHCCs. These nacre-inspired design schemes could also be employed to improve the mechanical property profiles of SHCCs otherwise limited by compositional, processing, or cost factors.

The conclusions and outcomes of these three projects also relate to one another. The limited strength, tensile strain capacity of the curauá-ECC may be improved by applying nacre-inspired hierarchical design schemes. Rather than using a synthetic polymer mesh material, natural plant

fiber meshes could be employed with similar benefits. The layered structure proven by the nacre-inspired composite design project to offer mechanical benefits to SHCC materials is encouraging for the use of ECC in 3DP processes, which produce a naturally layered structure. Conversely, 3DP is a natural fit as a processing route to produce alternate nacre-inspired hierarchical SHCC materials because of its ability to efficiently produce layers and complex geometries. The ability of the 3DP process to efficiently produce unique geometries and features can also be employed to produce appealing façade and building cladding members. The design strategies to produce printable ECC could be applied to curauá-ECC, and thus custom-designed, eco-friendly 3D printed curauá-ECC façade panels, produced with minimal material waste, can be imagined.

These exercises in relating the results and products of the three design projects reported herein underscore the highly applied, tangible nature, and broad impacts of the outcomes of this research. Each project was guided by a focus on feasible application, and the materials design and development for novel greening, processing, and bio-inspired structuring of Engineered Cementitious Composites represents innovation and improvement in a variety of cementitious infrastructure segments, contributing to improved sustainability of our built environment.

5.1.3 Directions for related future research

The materials design and development research reported here is meant to contribute to continued and future work on cementitious composites and their applications. The results of this research point to several specific directions for related future research.

Failure analysis of the most robustly strain-hardening curauá-ECCs indicates the potential for the tensile strain capacity and ultimate strength to be improved via matrix-fiber bond enhancement. Curing the composites in a carbon-rich environment is proposed to improve this interfacial bond. While carbonation is used as an accelerated degradation/aging process to study the durability of cementitious material, applied in the curing phase, it may serve to strengthen the interfacial transition zone, eliminating porosity and improving fiber-matrix bonding. Research investigating the effects on chemical reaction and resulting microstructural features of this process are recommended, including determination of appropriate process parameters to optimize SHCC performance.

Additional fiber treatments to improve fiber-matrix binding and/or fiber strength should also be pursued to improve composite performance and durability in a range of aggressive environments.

Related to the 3D printable ECC materials, interlayer bonding remains a weak point of the proof-of-concept materials produced, as well as of 3D printed members/structures in general. Strategies to improve interlayer bonding, through composition or process modification, should be studied and developed. The efficacy of the thixotropy enabled minimal workability loss approach to printability still remains to be confirmed with real, building-scale 3DP hardware systems. While these printable ECC materials have been designed to be universally compatible in principle with the various approaches to hardware design for building-scale 3D printing, minor system-specific material parameter requirements and adjustments are expected and need to be empirically calibrated. Additional considerations for full-scale printing also need to be studied, including appropriate hardening rate and time for large-scale prints in which the deposition of adjacent layers is separated by significant time intervals. Manipulation of strength and cost of the material (through composition adjustment), while maintaining the characteristics that make the material both printable and strain-hardening, will also requires additional testing. Finally, for successful commercialization, specific use cases, within the building-scale 3D printing industry, in which the "self-reinforced" printable ECC material offers significant value proposition over alternative/existing materials/methods need to be identified and targeted for early product development and adoption.

Related to the nacre-inspired hierarchical composite design project, the various deign schemes tested and reported here are meant to be models of the various approaches to adapting nacre-inspired features and deformation mechanisms to the larger scale. It has been shown that nacre-inspired structuring and deformation mechanism can offer mechanical benefits on a much larger scale than natural nacre, the most effective route to adapting these nacre-inspired concepts to infrastructure remains as an open question. The research reported here in this topic is by no means an exhaustive exploration, and only represents the initial steps toward a fully realized nacre-inspired infrastructure product. A significant amount of parameter optimization remains to be studied as it related to material choice (of the mesh and interfacial adhesive materials, for example) and layer/feature size ratios. Additionally, evaluation of these design scheme

approaches under blast, impact, and seismic loading is recommended to inform continued composite development.

In general, the durability of each of these novel varieties of ECCs in a range of aggressive environments needs to be studied such that weaknesses to environmental conditions can be addressed. Of particular concern is the longevity and property stability of the curauá fiber and the adhesive material used in one of the nacre-inspired design schemes. Also, while self-healing behavior has been observed previously in ECC materials, self-healing behavior and conditions required for effective healing need to be confirmed for each of these novel varieties, and associated implications for future application-specific design should be considered.

APPENDICES

Appendix II.1

Cultivation, Harvest, and Processing of Curauá Plants and Fibers

The first harvest of curauá takes place one year after planting. The number of harvested leaves normally ranges from 7 to 20 units per plant or more depending on the availability of mature leaves (average length of 1.5 m). One leaf weighs around 100 g and yields from 7 to 10% of dry fiber. Cordeiro et al. (2010) reported an annual yield varying from 496 to 1389 kg/ha from the first to the third year after planting in the monoculture field with spacing 0.8 x 0.5 m between the plants [28]. The interval between the collections varies from 3 to 4 months during a period of 5 or 6 years, corresponding to the plant life cycle, but that can be exceeded depending on the production system and cultivation care. In the range of three years the plant provides twelve collections, the last three being the most abundant ones as they represent the harvest from the mother-plant and also from the daughter-plants left aside. The so-called daughter-plants are sprouts that grow from the older plants and that are left together in order to increase productivity. The plant allows great flexibility in the collection intervals as the leaves stay mature without degradation for an extended period of time [28]. Curauá, therefore, has the potential to be a robustly renewable resource for engineering applications.

The extraction process of the fibers involves several steps. The harvest is done manually by pulling the leaves from the plant. The curauá fiber is extracted from the leaves immediately, in the cultivation fields, using an “EMBRAPA”-type decorticator with two blades. Decortication is the separation of mucilage, serum, and fibers. The mucilage can be used for animal feed, organic

fertilizer and pharmaceutical product. Serum produced by decortication and subsequent washing processes is also used as animal nutrition and as liquid fertilizer in curauá plantations [12].

After decortication, the fibers are washed in two tanks (containing only water) and air-dried for two or three days. Drying and protection from rain is important to prevent the undesired presence of fungi and subsequent decay. The total removal of mucilage through friction of the fibers (by beating process), allows for greater smoothness to the fiber surface. According to the Pematec company, there are currently no existing alternative methods (as of 2015) that achieve the efficiency of the procedure described above.

Appendix II.2

Additional Compositional Information about Ingredients

Class F Fly Ash Chemical Composition
(from Headwaters Resources, Monroe, Michigan Plant)

Silicon Dioxide (SiO2) 39.77%
Aluminum Oxide (Al2O3) 20.00%
Iron Oxide (Fe2O3) 9.74%
Sum (SiO2+Al2O3+Fe2O3) 69.51%
Sulfur Trioxide (SO3) 1.95%
Calcium Oxide (CaO) 18.88%
Magnesium Oxide (MgO) 3.67 %
Sodium Oxide (Na2O) 1.23 %
Potassium Oxide (K2O) 1.20 %
Sodium Oxide Equivalent (Na2O+0.658K2O) 2.02 %
Moisture 0.18%
Loss on Ignition 0.86%
Available Alkalies, as Na2Oe 1.14%

Elkem Microsilica (Silica Fume) Grade 955 (undensified) Chemical Composition
(from Elkem product data sheet)

SiO_2 95.5% (min)
C_{free}** 1.0% (max)
Fe_2O_3 0.3% (max)
Al_2O_3 1.0% (max)
CaO 0.4% (max)
MgO 0.5% (max)
K_2O 1.0% (max)
Na_2O 0.4% (max)
H_2O* 1.0% (max)

*when packed
**C in SiC not counted

Additional Compositional Ingredients

W.R. Grace ADVA 190 is a polycarboxylate superplasticizer used as a high range water reducing admixture

The US Silica brand Sil-Co-Sil 75 product is a ground silica (crystalline quartz)

The Type I Portland cement used in this study was sourced from Lafarge

Appendix III.1
Materials

Presented here is additional information regarding the materials used in the cementitious composites reported in this 3D printable SHCC study. The information presented in this appendix was provided by the materials' respective manufacturers/suppliers.

Lafarge Type I Portland Cement

Table AIII.1: Compositional characterization of Lafarge Type I Portland Cement, Alpena, MI plant

Compositional Component	**Content (%)**
SiO_2	19.6
Al_2O_3	4.6
Fe_2O_3	3.0
CaO	63.5
MgO	2.6
SO_3	2.6
Loss on ignition	2.6
Insoluble residue	0.32
Free lime	1.4
CO_2	1.7
Limestone	4.3
$CaCO_3$ in limestone	87.0

Class F fly ash chemical composition

Table AIII.2: Class F fly ash chemical composition as provided by Headwaters Resources, Monroe, Michigan Plant

Compositional Component	Content (%)
Silicon Dioxide (SiO_2)	39.77
Aluminum Oxide (Al_2O_3)	20.00
Iron Oxide (Fe_2O_3)	9.74
Sum (SiO_2+Al_2O_3+Fe_2O_3)	69.51
Sulfur Trioxide (SO_3)	1.95
Calcium Oxide (CaO)	18.88
Magnesium Oxide (MgO)	3.67
Sodium Oxide (Na_2O)	1.23
Potassium Oxide (K_2O)	1.20
Sodium Oxide Equivalent (Na_2O+0.658K_2O)	2.02
Moisture	0.18
Loss on Ignition	0.86
Available Alkalis, as Na_2Oe	1.14

Elkem Microsilica (Silica Fume) Grade 955 (undensified)

Table AIII.3: Chemical composition of Elkem Microsilica (Silica Fume) Grade 955 (undensified)

Compositional Component	Content (%)
SiO_2	95.5 (min)
C_{free}**	1.0 (max)
Fe_2O_3	0.3 (max)
Al_2O_3	1.0 (max)
CaO	0.4 (max)
MgO	0.5 (max)
K_2O	1.0 (max)
Na_2O	0.4 (max)
H_2O*	1.0 (max)

*when packed

**C in SiC not counted

Additional compositional information:

The high range water reducing admixture used is W.R. Grace ADVA 190, a polycarboxylate superplasticizer

The ground silica used is US Silica brand Sil-Co-Sil 75 (crystalline quartz)

The silica sand used is US Silica brand F-75 silica sand

The attapulgite nanoclay used is an Active Minerals International product called Actigel208, which is a highly purified hydrous magnesium aluminum-silicate (Attapulgite) made from a patented process that creates pure, uniformly sized, rod – shaped mineral particles.

The polymer fibers used are poly vinyl alcohol (PVA), with diameter of 40 microns and length of 12mm.

Appendix IV.1
HSHDC Compositional Information

Presented here is additional information regarding the materials used in the cementitious composites reported in this study. Quantitative information presented in this appendix was provided by the materials' respective manufacturers/suppliers. Additional discussion of this composition can be found in Ranade et al. (2011) [24].

Microsilica: Elkem 955 undensified Microsilica (silica fume)
Table A.1: Chemical composition of Elkem Microsilica (Silica Fume) Grade 955 (undensified)

Compositional Component	Content (%)
SiO_2	95.5 (min)
C_{free}**	1.0 (max)
Fe_2O_3	0.3 (max)
Al_2O_3	1.0 (max)
CaO	0.4 (max)
MgO	0.5 (max)
K_2O	1.0 (max)
Na_2O	0.4 (max)
H_2O*	1.0 (max)

*when packed

**C in SiC not counted

Class H cement: The primary cementitious component used is Lafarge Class H oil well cement.

HRWRA: The high range water reducing admixture used is W.R. Grace ADVA 190, a polycarboxylate superplasticizer

Ground Silica: US Silica brand Sil-Co-Sil 75 (crystalline quartz)

F-60 silica sand: US Silica brand F-60 silica sand

UHMW-PE Fiber: The ultra high molecular weight polyethylene fibers used is Honeywell brand Spectra 900 (675 denier), cut to 0.5" (12.7 mm) by Minifibers, Inc. (Johnson City, TN). The fibers have a diameter of 38 microns, a niminal strength of 3000 MPa, modulus of 100 GPa, and specific density of 0.97.

Appendix IV.2

HSHDC Mixing and Accelerated Curing Procedure

A 12 gallon Hobart planetary style mixer is used. Dry ingredients (excluding fibers) are first mixed for at least 5 minutes, then approximately one third of this dry mix is removed from the mixer to be added in later in small amounts at regular time intervals to aid proper hydration and mixing. The entire water content is added at time, t=0. The HRWRA content is added immediately after the addition of water at approximately t=30 seconds. Over the next several minutes the mix turns from a damp powder to liquefied paste. At this point the remainder of the dry mix is reintegrated in several steps. The mix is allowed to return to a paste-like state prior to the addition of more of the dry mix. Prior to fiber addition, half of the fiber content (by weight) is first soaked in water for several minutes. The water (as much as possible) is then wrung out of this portion of fibers via manual squeezing. The fibers are reweighed to determine the additional water content being added to the mix. The additional water carried by the soaked portion of the fibers when added to the mix is approximately 0.38-0.45 g water for 1.0 g of total fibers (dry weight). Once all the dry ingredients have been thoroughly mixed into the paste, fibers are added in small handfuls, with clumps of the soaked fibers picked apart by hand prior to being added. The vinyl-silane coupling agent is added immediately fiber addition is completed. Mixing is continued for 2-3 minutes after the addition of the coupling agent. Casting is then performed immediately.

Demolding is performed 24-48 hours after casting (depending on size of specimen). Specimens are then placed in a room temperature water bath for seven days for continued hydration. Specimens are then placed in an elevated temperature (80C) water bath for four additional days, after which they are removed from the water bath and dried at elevated temperature (70-80C) for at least 24 hours. Specimens are allowed to return to room temperature prior to testing. In schemes where polymer adhesive is applied following this curing process, the adhesive is allowed to cure for an additional 4-5 days.